OPTIMIZING REGISTRATION OF COMPLEX VASCULAR GEOMETRIES

by

MIE KUNIO

B.Eng. in Applied Physics and Physico-Informatics, Keio University, 2010
M.Sc.Eng. in Fundamental Science and Technology, Keio University, 2012

Submitted to the Harvard-MIT Division of Health Sciences and Technology
in Partial Fulfillment of the Requirements for the Degree of

Doctor of Philosophy

in the subject of

Medical Engineering and Medical Physics

at the

MASSACHUSETTS INSTITUTE OF TECHNOLOGY

June 2016

Signature of Author ..... Signature redacted .....
Harvard-MIT Division of Health Sciences and Technology
May 16, 2016

Certified by ..... Signature redacted .....
Elazer R. Edelman, M.D., Ph.D.
Thomas D. and Virginia W. Cabot Professor of Health Sciences and Technology
Thesis Supervisor

Accepted by ..... Signature redacted .....
Emery N. Brown, M.D., Ph.D.
Director, Harvard-MIT Division of Health Sciences and Technology
Professor of Computational Neuroscience and Health Sciences and Technology

Optimizing Registration of Complex Vascular Geometries

by

Mie Kunio

Submitted to the Harvard-MIT Division of Health Sciences and Technology
in Partial Fulfillment of the Requirements
for the Degree of Doctor of Philosophy in Medical Engineering and Medical Physics

ABSTRACT

Advances in imaging, such as coronary angiography, intravascular ultrasound, and optical coherence tomography, can improve procedural success and outcomes for endovascular catheter intervention, such as stent implantation. Yet, these imaging modalities are not universally embraced; and thus, optimization of stent implantation and management of the adverse outcomes remain challenging. This is partially because full adoption of complex imaging awaits methods to reconstruct precise 3D structure of lumen and implanted stent, and to track vascular responses to stent implantation over time in 3D.

This thesis creates new methods for reconstruction and registration in 3D by melding disparate imaging modalities, coronary angiography and optical coherence tomography (OCT), that provide different 2D-plane information (longitudinal and cross-sectional) using widely-varied experimental models (static phantom models, preclinical swine model with controlled scenarios of stent implantation in coronary arteries, and clinical unbiased model of stent implantation). A 3D vessel centerline from coronary angiography serves as a fusion path for OCT to reconstruct 3D structures and as a registration path for the reconstructed 3D structures across time.

The developed vessel centerline reconstruction method overcame current spatial and temporal alignment challenges, and demonstrated high reproducibility across imaging angles and throughout the cardiac cycle. Structural reconstruction by angiography-OCT fusion was established and improved to account for the cardiac motion, reducing error in estimation of the stent length from 5.5% ± 4.5% with standard fusion to 2.4% ± 2.0%. Time-point registration was accomplished by detecting landmarks that are least affected by the vascular responses - its error, i.e., stent-strut shift from post-implantation to follow-up, was 1.6 mm ± 0.5 mm (9.2% ± 3.0% of the stent length). These methods were validated in a clinical setting and the errors of all methods were within those in the preclinical setting, suggesting potential for clinical applicability.

Thesis Supervisor: Elazer R. Edelman, M.D., Ph.D.

Title: Thomas D. and Virginia W. Cabot Professor of Health Sciences and Technology

ACKNOWLEDGEMENT

First, I would like to thank Prof. Elazer Edelman for his continuous support and guidance throughout my entire PhD life. I met him a year before I entered this PhD program – if I did not have a chance to meet him at that time, I would never know this program and I just lost my opportunity to come here. After entering this program, he welcomed me warmly and always gave me the best and most reliable advice on my research and course work. He also provides me a lot of advice on my professional and personal life. I cannot imagine my PhD life without his guidance. Thank you very much.

Second, I am deeply thankful to Prof. Guillermo Tearney. He has served not only as my thesis committee chair, but also as my thesis technical advisor and my mentor for my future career. Whenever I had problems in my research, he always showed me the best solution that I've never imagined. He sometimes challenged me, which helps lead my research in a better direction and grow myself. I really appreciate his support.

Third, I am grateful for the support from Dr. Peter Stone. He always reminded me (and all other committee members) how important and valuable my PhD work was every committee meeting, which saved me many times when I felt lost in my research. He also always gave me a warm and nice note after every meeting. Thank you very much for your kind support.

I would also like to thank Prof. Mehmet Toner, Prof. John Gabrieli, and Prof. Thomas Heldt, who were my qualifying exam committee members. If they had not challenged me at my qualifying exam, my thesis would not be precious in the medical/clinical aspect. Thank you very much for helping me shapes my PhD thesis to be valuable in both engineering and medicine.

I thank my Brazilian collaborators, Dr. Pedro Lemos, Dr. Augusto Celso de Araujo Lopes Jr., and Dr. Micheli Galon, who kindly share the clinical data. My thesis work cannot be completed without the access to this dataset. Thank you very much.

I appreciate the help from my academic advisor, Prof. Richard Cohen. We had a meeting at

the beginning of every semesters and he always made sure that I was on the track. He also encouraged me whenever I felt overwhelmed. Thank you very much for your continuous support.

I'd like to thank Dr. Caroline O'Brien. She always helped me whenever I had technical problems in my research even after she left the lab.

My life at the lab was always supported by my lab mates, especially Kim LePage, Demet Guntas, Dr. Pedro Melgar Lesmes, Dr. Sara Strecker, Dr. Lyndon Charles, Dr. Christina Arnold, Dr. Farhad Rikhtegar Nezami, Dr. Kay Everett, and Or Gadish – they are very intelligent, kind, and supportive. They always cheered me up whenever I was overwhelmed and/or I felt I could not move forward. Thank you very much for their mentorship and friendship.

My life at HST cannot be talked without my classmates, Lina Colucci, Britni Crocker, Cheryl Cui, Anik Debnath, Atray Dixit, Or Gadish, Jaeseung Hahn, Isha Jain, Katerina Mantzavinou, Changwook Min, Rida Mourtada, Bryan Ranger, Adhvait Shah, Jeff Stout, my HST friends, especially Katelyn Burkhart and Jingzhi An, and academic office stuffs, Dr. Julie Greenberg, Laurie Ward, Traci Anderson, and Joe Stein. They always supported and understood me although we have completely different cultural backgrounds. They are my wonderful English teachers as well – I learned a lot about English and many different cultures from them.

My life at MIT is always surrounded by my friends, especially Yiou He, Lixin Sun, Sasha Miao, Hsin-Jung Yang, members of Coffee Hour Committee. The time that I spent with them is always fun, relaxing, and makes me forget about my research. We talked a lot - sometimes about the lab lives, sometimes about our personal lives. I also have wonderful Japanese friends. We shared many common experiences that we had to go through as an international student – it is always nice to talk about it in my native language. We have many traditional celebration events together, in which I always feel I am at home. Thank you very much for all the friendship.

I'd like to thank my best friend, Mahoko Taniguchi. Although our majors are completely different, we have many similarities in the way that we tackle challenges. We have been able to develop ourselves by motivating each other - she is a person who encourages and supports me

anytime I need. Thank you very much for your kind support and our friendship.

I cannot imagine myself being in the US without having my American parents, Roger and Pascaline Tran. Throughout my PhD life, they always teach me how American culture is different from Japanese culture and how I should behave in a different culture. They have treated me as their actual daughter and encourage me whenever I feel I need to give up this PhD program. They also support me to find my future career path – they understand me very well and try hard to find the best way that I should go. Thank you very much for your warm support and wonderful advice on my professional and personal life.

I would like to thank Kyle Paczkowski. He went through the last period of my PhD that I was very stressful. He accepted me anytime, no matter how good or bad condition I was in at that time. He always supported me and encouraged me – he gave me strength to complete this PhD. Thank you very much.

My grandfather, Yoshizo Kaneko, led me to be a biomedical engineer. He believed the power of education, especially for women, and kept telling me to educate myself as same as men will do, although it is less acceptable in Japanese culture. Unfortunately, he died 13 years ago, but his death meant a lot to me. I decided to study biomedical engineer and to develop medical devices that will help my loved ones be happy until the last moment. Thank you for giving me an idea to highly educate myself and to live a life that I can help others.

Finally, I would like to give my best and deepest appreciation to my parents, Takemitsu and Misuzu Kunio. They have been my role models in entire my life. They encouraged me to apply to this PhD program and gave me confidence to study abroad. Whenever I lost my confidence, I was overwhelmed, and I felt that I could not move forward, they always supported me and gave me advice and solutions how to go through. They visited me many times, although it costed a lot to them, to support me in person. I don't think I can finish my PhD without their continuous support, help and advice. Thank you very much.

TABLE OF CONTENTS

LIST OF FIGURES

CHAPTER 1: INTRODUCTION

CHAPTER 2: DEVELOPMENT OF VESSEL CENTERLINE RECONSTRUCTION IN STATIC PHANTOM MODELS

CHAPTER 3: VALIDATION OF VESSEL CENTERLINE RECONSTRUCTION & DEVELOPMENT OF STRUCTURAL RECONSTRUCTION AND TIME-POINT REGISTRATION IN A PRECLINICAL SETTING

CHAPTER 4: VALIDATION OF STRUCTURAL RECONSTRUCTION AND TIME-POINT REGISTRATION IN A CLINICAL SETTING

CHAPTER 5: CONCLUSIONS

APPENDIX: PRECLINICAL STENT-CELL LEVEL ANALYSIS

LIST OF TABLES

CHAPTER 1: INTRODUCTION

CHAPTER 2: DEVELOPMENT OF VESSEL CENTERLINE RECONSTRUCTION IN STATIC PHANTOM MODELS

CHAPTER 3: VALIDATION OF VESSEL CENTERLINE RECONSTRUCTION & DEVELOPMENT OF STRUCTURAL RECONSTRUCTION AND TIME-POINT REGISTRATION IN A PRECLINICAL SETTING

CHAPTER 4: VALIDATION OF STRUCTURAL RECONSTRUCTION AND TIME-POINT REGISTRATION IN A CLINICAL SETTING

CHAPTER 5: CONCLUSIONS

CHAPTER 1: INTRODUCTION

1.1 Thesis Overview

Coronary artery disease is a major cause of death worldwide, and its prevalence is expected to increase [1-4]. Innovations in imaging, i.e., more precise angiography and intravascular imaging, have revolutionized our ability to diagnose coronary artery disease [5-8] and have dramatically improved the procedural success of catheter-based intervention, including stent implantation, which is a widely-used treatment for atherosclerotic coronary artery disease [5, 9-12]. However, stent implantation may fail due to adverse outcomes, such as stent thrombosis (1.2% after BMS, 0-2.7% with annual increase rate of 0.6% after DES [14-17]) and in-stent restenosis (20-25% after BMS, 8.6% after DES [21]). Therefore, the current challenges in stent implantation are how to predict outcomes, how to prevent stent failure, and how to treat adverse vascular responses to stent implantation. Studies have attempted to reveal the mechanism of these variable vascular responses by correlating lesion locations, plaque components in lesions, and changes in blood flow patterns due to stent implantation using high-resolution intravascular images and computer simulations [22-26]. However, these studies are limited to 2D. Structures of a lumen and a stent cannot be reconstructed in 3D from the 2D intravascular images that are taken perpendicular to the imaging catheter because the location of the catheter in 3D space is unknown [5]. Neither can the vascular morphological changes can be tracked over time in 3D since the imaging catheter cannot be placed at the exact same position at follow-ups. To compare the images from different time-points in 2D, we use landmarks which are visible at all time-points, but this comparison is limited by the number of available landmarks and prevents the usage of the entire imaging dataset [23].

It is here that this thesis contributes by integrating vascular biology, fluid dynamics, and imaging technology. The underlying hypothesis of this thesis is that new methods to reconstruct

the 3D structures of lumens and stents accurately and to register the 3D structures of the same vessel across different time-points can be developed by melding different imaging modalities, i.e., coronary angiography and intravascular imaging modality. 3D reconstruction will advance the understanding of the interaction between plaque components in the lesion and the hemodynamic influence on the vascular wall in 3D. Time-point registration will provide the novel knowledge about the time course of vascular responses in 3D. Specifically, this thesis will concentrate on the vessel centerline technique – extracting the vessel centerline from two planar coronary angiographic images and transforming the 2D centerline information of each image into one 3D space [28]. The 3D vessel centerline can provide both the 3D location of the imaging catheter for 3D reconstruction and 3D landmarks for comparison of images taken at different time-points. Although this technique has been used previously [29, 30], the state-of-the-art methods have been validated for images acquired under conditions that are difficult for physicians to satisfy in the clinical situations. Therefore, to improve the technique and make it clinically applicable and to enable the accurate reconstruction of 3D structures of lumens and stents and the registration of them across time, this thesis is proposed with three specific aims:

Specific Aim 1: Develop a vessel centerline reconstruction method in static phantom models

Specific Aim 2: Validate a vessel centerline reconstruction method and
Develop a structural reconstruction method and a time-point registration method in a preclinical setting

Specific Aim 3: Validate the structural reconstruction and the time-point registration methods in a clinical setting

This multi-scale and multi-dimensional project combines the rigor of precise imaging and fluid dynamics, the power of both bench-top and animal studies with controllable parameters, and clinical patient data with uncontrollable parameters. The tools developed through this project enable making use of all the available imaging data including unbiased and clinically diverse

patient data. The accumulated data can serve as a data bank, which will help physicians assess the risk of stent failure, optimize the procedure and prescribe patient-specific medication. Moreover, the 3D reconstruction method will enable physicians to diagnose the lesion more accurately. By using the data bank, they can predict the vascular responses to stent implantation before the procedure, which guides the interventional procedures to achieve better outcomes. Therefore, the completion of this thesis will enable the improvement of catheter intervention, especially stent implantation.

1.2 Cardiovascular Diseases and Coronary Artery Diseases

1.2.1 Mortality and Morbidity

Cardiovascular disease is the main cause of mortality and morbidity worldwide and is responsible for 17 million deaths (a third of all deaths) annually [2]. In the US alone, 83 million people suffer from cardiovascular disease [1, 31], and 3 million people are newly diagnosed per year [2]. By 2030, almost 25 million people worldwide will die of cardiovascular disease [3]. Cardiovascular diseases can be categorized into variable disorders of heart and vasculatures, such as coronary artery disease, cerebrovascular disease, and peripheral arterial disease [3]. Within these categories, coronary artery disease (CAD) itself remains to be the primary cause of mortality and morbidity all over the world [3]. It is responsible more than half of all cardiovascular diseases in the population younger than 75 years old and accounts for approximately 40% of all cardiovascular deaths (approximately 3.8 million men and 3.4 million women) every year [3, 4, 32, 33]. According to the Global Burden of Disease study, the death from CAD is expected to increase and to reach 11.1 million in 2020 [32, 33]. In addition, CAD is predicted to be the leading cause of death for the next 20 years [33, 34]. In the US, CAD causes about 1 of every 6 deaths [1], which is half of the deaths from cardiovascular diseases. The American Heart Association estimates that approximately 785,000 Americans will have a new coronary attack and that

approximately 470,000 will have a recurrent attack, with an additional 195,000 silent first myocardial infarction occurrence every year [1].

The economic impact of cardiovascular disease, especially CAD, is straining medical insurance coverage and global economies [1, 4, 32, 33, 35]. In the US alone, the total direct cost, i.e., the medical cost, of cardiovascular disease is expected to increase 200% within 20 years (272.5 billion dollars in 2010 to 818.1 billion dollars in 2030), and the total indirect cost due to lost productivity is expected to increase 61% within 20 years (171.5 billion dollars in 2010 to 275.8 billion dollars in 2030) [35]. Therefore, developing new treatments that are inexpensive and effective based on understanding the mechanisms of CAD is crucial not only for decreasing mortality and morbidity, but also for lowering health care costs.

1.2.2 Treatment Methods

The major cause of CAD is atherosclerosis [36]. Atherosclerosis is a chronic inflammatory condition which occludes arterial lumens, limiting tissue perfusion and inducing ischemia in the myocardium [18, 36-38]. This ischemia frequently causes symptoms of chest pain, known as angina, and causes sudden cardiac death in the worst-case scenario. To prevent the negative outcome and to improve quality of life by reducing the rate of angina attacks and/or symptoms, pharmaceutical treatment and/or revascularization, i.e., restoration of arterial lumen diameter and blood flow, by a surgical means or through minimally-invasive interventions are performed [33, 36, 39].

1.2.2.1 Pharmaceutical Treatment

Pharmaceutical treatment is used for two purposes: to prevent acute cardiac events and to prevent ischemic events [18, 33].

If atherosclerotic plaque is ruptured and/or if a coronary artery is injured for any reasons, platelets will be aggregated and a thrombus will be formed in the coronary artery, both of which

are key elements in pathophysiology of acute myocardial infarction and unstable angina. Antithrombotic therapy can prevent further occlusion of coronary arteries that is caused by platelet aggregation and thrombus formation and can facilitate dissolution of the thrombus. This type of therapy includes antiplatelet medications, such as aspirin, clopidogrel, prasugrel, and glycoprotein IIb/IIIa receptor antagonists, and anticoagulant medication, such as unfractionated heparin and low molecular weight heparins.

Pharmaceutical treatment can be the first line of defense to prevent angina attacks for the patients with chronic ischemic heart disease. The purpose of this treatment is to decrease the cardiac workload, i.e., decrease the oxygen demand in the myocardium, and to increase myocardial perfusion; and thus, to balance the demand and supply of oxygen to the myocardium. Three classes of medications are commonly used: organic nitrates, β-adrenergic blockers, and calcium channel blockers. Angiotensin-converting enzyme (ACE) inhibitors, a well-known medication for heart failure treatment, may also prevent further angina attacks by reducing the cardiac workload.

1.2.2.2 Coronary Artery Bypass Surgery

Before the invention of catheter intervention, coronary artery bypass surgery (CABG) was the alternative to pharmaceutical treatment and only revascularization choice for the patients with ischemic heart disease due to CAD. This procedure bypasses the occluded region of coronary artery by grafts [18]. There are two types of surgical grafts: native vein, typically a section of the saphenous vein, and arterial grafts, most commonly an internal mammary artery (Figure 1-1). The native vein graft connects between the base of the aorta and the downstream of the stenotic region in the coronary segment. The arterial graft can directly connect to the distal of the stenotic coronary artery site. Since it is more resistant to atherosclerosis, an arterial graft is often used to perfuse the more critical sites, such as the left anterior descending artery.

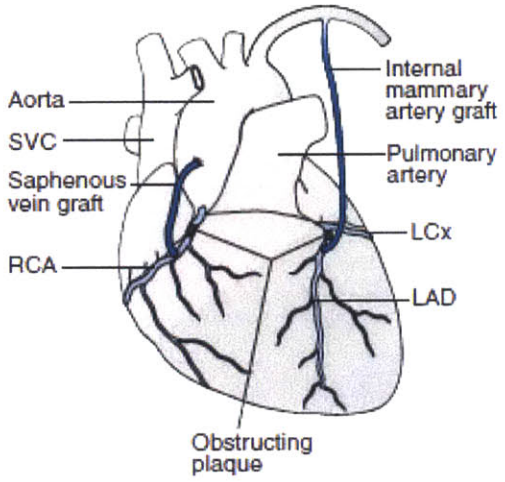

Figure 1-1 Coronary artery bypass surgery [18]

Two types of bypass surgeries are shown in this figure. (1) One end of the saphenous vein graft is connected to the proximal aorta and the other end is to the distal of the stenotic region in right coronary artery. (2) The internal mammary artery graft from the left subclavian artery is bypassed to the left anterior descending artery at the distal of the stenotic area.

1.2.2.3 Catheter Intervention

Balloon angioplasty was the first and is the simplest interventional therapeutic method for revascularization [36, 40]. A balloon-tipped catheter is inserted into a narrowed artery and inflated to dilate the artery. After inflation, the catheter is deflated and removed from the dilated artery (Figure 1-2). This procedure was invented by Dotter et al. in 1964 [41] and was first performed in human coronary arteries by Gruentzig in 1977 [42]. To obtain sufficient dilation against the elasticity of the vessel wall, plastic deformation with high balloon pressure is required; and thus, the intima and the media are stretched and the atherosclerotic lesion is sometimes fractured. These phenomena induce renarrowing of the artery, i.e., restenosis, (35-40%) on both acute and chronic phases due to (i) elastic recoil of the arterial wall immediately after balloon deflation and (ii) excessive proliferation over time of smooth muscle cells during healing [21, 36, 43, 44]. To decrease restenosis and to maintain revascularization over extended periods of time, adjuvant methods, such as stent implantation, were developed.

Stents are expandable metal mesh tubes that are implanted into the atherosclerotic lesions to maintain long-term arterial dilation. They are used more than 90% of the time with balloon angioplasty [2, 15, 45, 46], and more than 2 million people are treated annually worldwide. In the

US alone, approximately 600,000 patients undergo stent implantation every year [1, 47-49]. Two kinds of stents are commonly used: Bare Metal Stent (BMS) and Drug Eluting Stent (DES). DESs are coated with anti-proliferative drugs that are released over time [2, 15, 45, 46]. The usage of these stents has reduced restenosis, the main adverse outcome of balloon angioplasty. However, it has introduced new adverse events, such as stent thrombosis (1.2% after BMS, 0-2.7% with annual increase rate of 0.6% after DES [14-17]) and in-stent restenosis (20-25% after BMS, 8.6% after DES [21]) (Figure 1-3). Although relatively uncommon, these events are often fatal. For example, 50-70% of stent thrombosis cases lead to non-fatal myocardial infarction and 20-40% lead to death [50, 51]. If patients have in-stent restenosis, they may need to undergo repetitive catheter intervention or CABG based on the severity of coronary artery renarrowing.

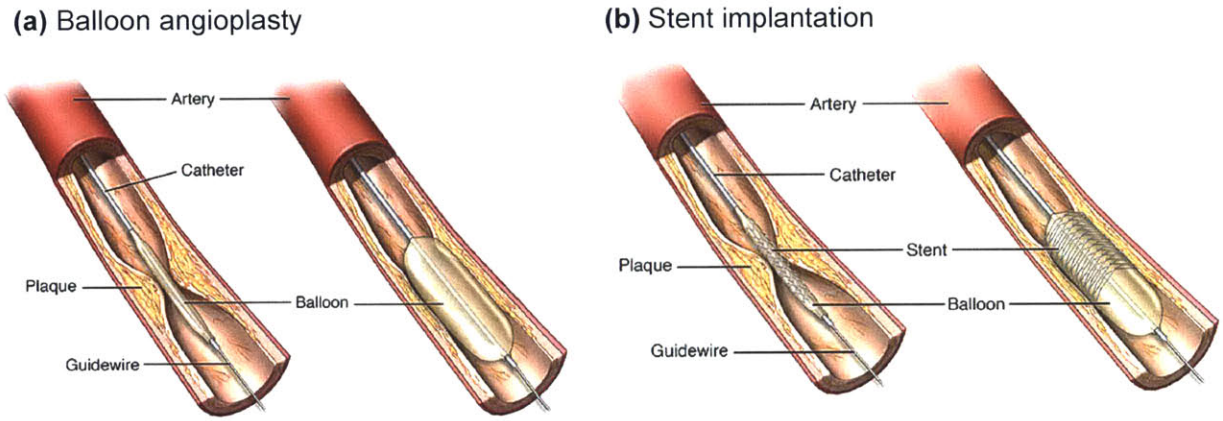

Figure 1-2 Catheter intervention: (a) Balloon angioplasty and (b) stent implantation [13]

An uninflated balloon catheter is inserted into the narrowed artery. Then, the balloon is dilated for about 30-60 s. Finally, the balloon is deflated and removed. If the stent is implanted, the stent is delivered to the region with the balloon catheter, dilated as the

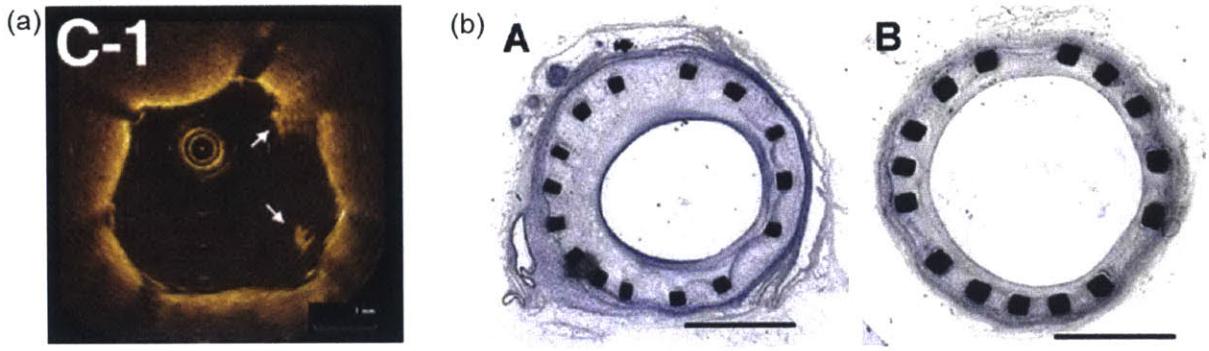

Figure 1-3 Adverse outcomes of stent implantation: (a) Stent thrombosis [20] **and (b) in-stent restenosis** [27]

(a) Intracoronary thrombi were identified as intra-luminal mass (arrows) by optical coherence tomography (OCT). **(b)** Neointima was formed inside the stent area, as shown in both histology images. Scale bar represents 1 mm.

Although there are some conditions that CABG is recommended rather than catheter intervention [52], the number of patients who will undergo catheter intervention, especially stent implantation, is expected to increase, while the number of CABG cases is expected to decrease [53].

1.2.3 Imaging Modalities for Catheter Intervention

The innovative imaging techniques have improved catheter-based coronary interventions dramatically. These imaging modalities help physicians to localize and diagnose the lesion more rapidly and precisely, to evaluate the procedural success quickly after the intervention, and to assess the chronic outcomes of the intervention [5, 54]. These imaging modalities can be categorized into two groups based on the imaging plane of coronary arteries: longitudinal plane and cross-sectional plane. Coronary angiography and computed tomography angiography provide longitudinal silhouettes of coronary artery lumens, while intravascular imaging modalities provide information on the cross-sectional plane of coronary artery structures (Figure 1-4).

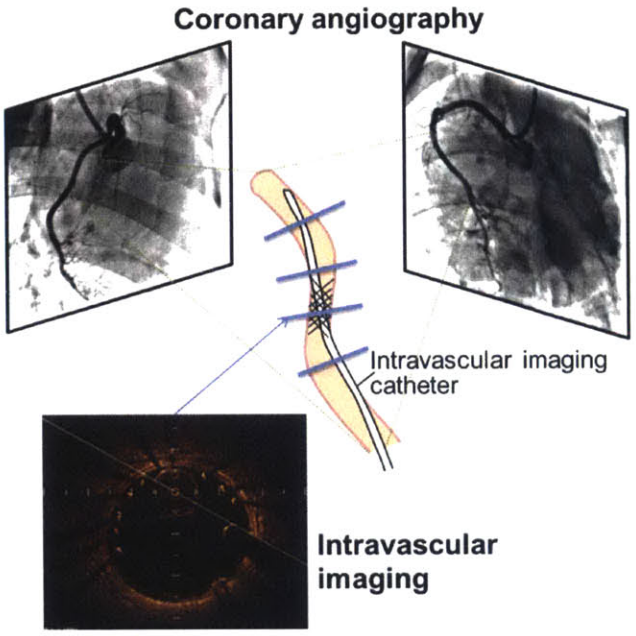

Figure 1-4 Imaging modalities for catheter intervention

Coronary angiography and computed tomography angiography show longitudinal silhouettes of coronary artery lumen. Intravascular imaging, such as intravascular ultrasound and optical coherence tomography, provides cross-sectional images of coronary arteries.

1.2.3.1 Coronary Angiography

The rapid evolution of catheter intervention requires a standardized method to diagnose CAD severity and to evaluate the procedural success after the intervention [18, 54]. Coronary angiography is the gold standard for pre-interventional CAD evaluation and post-interventional therapeutic effect evaluation [8, 54].

Coronary angiography shows two-dimensional projections of the lumens of arteries. A radio-opaque contrast dye is injected into the vasculature from the femoral artery with an access through the inguinal region, and X-ray is radiated through the body to the intensifier, which is located at the opposite site from the X-ray source. A C-arm fluoroscopic angiography system is usually used for obtaining angiographic images. This C-arm machine allows physicians to change angles of X-ray radiation and/or the location of the table where a patient is placed to obtain better views during the procedures. Before the catheter intervention, several projections are obtained from different positions and quantitative coronary angiography (QCA) analysis is performed to evaluate the severity of CAD, i.e., the lesion length and the percentage of arterial

occlusion, based on the size of a guiding catheter. Then, the sizes of a balloon catheter and a stent are determined and catheter intervention proceeds. After the procedure, several more projections are obtained to confirm successful revascularization. Angiography can also be used for follow-up checking to detect the renarrowing of the artery due to in-stent restenosis or stent thrombosis. Although coronary angiography is a routine imaging modality and QCA provides acceptable evaluation of lesion dimension before intervention for basic clinical decision-making, multiple studies have shown the significant inter- and intra-observer variability [54-57]. In addition, only the arterial lumen can be seen in coronary angiography, which is most affected by thrombus. Both of these facts result in either overestimation or underestimation of CAD severity and lead to create geographic mismatch between the lesion and the stented region [54-57]. The incidence rate of geographic mismatch is reported as 47.6% and is considered to increase the risk of re-intervention by 2.3-fold and the risk of non-fatal myocardial infarction by 3-fold [55].

1.2.3.2 Computed Tomography Angiography

Computed tomography can provide a long series of images in the axial direction (proximal to distal direction) in a non-invasive manner [5, 18]. An X-ray tube rotates around the body and the generated thin X-ray beams irradiate the body. Electronic detectors capture the non-absorbed X-ray beams and an image is reconstructed from the different projections. Since distinct tissues have different absorption rates of X-ray beams, organs and/or tissue types can be distinguished in computed tomography images. Computed tomography angiography emphasizes coronary arteries through the injection of radio-opaque contrast dye in the similar manner as that of coronary angiography [5, 18]. Computed tomography angiography is superior to coronary angiography because the effect of cardiac movement can be avoided in computed tomography angiography with the dedicated software [5]. It is also better than coronary angiography since it is a relatively inexpensive and significantly less invasive technique compared to coronary angiography. However, it cannot be used in the interventional suites and its sensitivity to detect

coronary artery is not as good as that of coronary angiography. Neither can it evaluate adequately the renarrowing of an artery after stent implantation because it is confounded by metal in stents. Moreover, this technique results in significant radiation exposure [18]. Therefore, computed tomography angiography is mainly used for assessing patients with symptoms that suggest CAD and for following the progression of known CAD, while coronary angiography is used to guide intervention and to follow up after the procedure.

1.2.3.3 Intravascular Imaging Modalities

To improve lesion diagnosis and to understand the mechanism of vascular responses to catheter intervention, the detailed information of coronary artery wall is critical. Thus, intravascular imaging modalities have been developed as both coronary angiography and computed tomography angiography can only provide information of coronary artery lumens.

There are two types of intravascular imaging modalities: intravascular ultrasound (IVUS), which uses ultrasound as its light source, and optical coherence tomography (OCT), which uses near-infrared light (Table 1-1). Both intravascular imaging modalities show cross-sectional planes of the coronary artery that are taken perpendicular to an intraluminal imaging catheter inserted from the inguinal region. IVUS can detect the lumen border, vessel wall morphology, and volumes and components of coronary atherosclerotic plaques precisely in 2D space because of its high penetration depth (about 10 mm) [10, 58, 59]. OCT also allows defining the structures inside the vessel wall, although it does not penetrate through all plaques. Because of its higher in-plane resolution (12-15 μm), OCT is preferable to IVUS to evaluate the endovascular structures, i.e., both lumen border and stent-struts [22, 60-64]. In addition, the image of approximately 50-mm long coronary artery can be obtained in few seconds with OCT, while it takes 30-60 s with IVUS due to the difference in pullback speed. Unlike IVUS, OCT requires radio-opaque contrast dye flushing to clear blood from the field of view.

Catheter intervention guided by intravascular imaging modalities has been proposed to

reduce the adverse outcomes of stent implantation. Since both OCT and IVUS are very effective for determining the longitudinal extent of the lesion, the likelihood of geographic mismatch ban be decreased. Also, since these modalities can detect intra-luminal information, especially stent location relative to lumen surface, acute stent malapposition can be prevented. IVUS-guided catheter intervention demonstrated 40% decrease in the risk of stent thrombosis, 32% decrease in the risk of non-fatal myocardial infarction, and 33% decrease in the risk of cardiac death [65].

Table 1-1 Comparison of IVUS and OCT [19]

+: OK; ++: Good; +++: Excellent

	IVUS	OCT
Light source	Ultrasound	Near-infrared light
Frame rate [fps]	30	100
Pullback speed [mm/s]	0.5-1.0	20
In-plane resolution [μm]	150	12-15
Tissue penetration [mm]	10	1.0-2.0
Need for contrast or Dextran	No	Yes
Detection of lipid	+/++	+++
Detection of fibrous cap	+	+++
Detection of thrombus	+	++
Detection of calcium	+++	++
Dissection	++	+++
Malapposition	++	+++
Stent-strut surface coverage	+	+++

1.2.4 Underlying Mechanisms of Vascular Responses to Catheter Intervention

Although several imaging modalities can be used to guide catheter intervention, a non-negligible rate of adverse outcomes has occurred after the intervention. To prevent these adverse events, optimization of catheter interventional procedures and the understanding of underlying mechanisms of these vascular responses to stent implantation are critical. Many studies have attempted to correlate adverse events, i.e., stent thrombosis and in-stent restenosis, with lesion locations, plaque components in lesions, and hemodynamic effects that are

determined by geometrical interaction between lesions and stent-struts. Since the stent-strut itself can be an obstacle and create turbulent blood flow or blood stagnation, the mis-sizing and the mis-positioning of stents may exacerbate the response to flow [9, 14, 15, 21, 22, 24, 25, 36, 40, 66-80]. Thicker BMS stent-struts tend to disturb blood flow more and to induce more thrombosis than thinner stent-struts [26] (Figure 1-5). Malapposition of stents to the arterial walls or overlapped usage of stents induces the deposition of blood, leading to the formation of thrombus [26] (Figure 1-5). Acute stent malapposition, i.e., incomplete stent apposition at post-implantation, was observed in 62% of lesions when DES was used [71], increasing the risk of stent thrombosis by 22.5-fold, the risk of non-fatal myocardial infarction by 7.1-fold, and the risk of cardiac death by 2.7-fold [67]. For DES, flow will further augment these adverse responses by causing local variability in drug deposition [81-85]. Blood flow disruption due to stent placement causes variation in wall shear stress along the stented arteries [86, 87] (Figure 1-6). Lower wall shear stress environments have been known to facilitate proliferation of smooth muscle cells. Greater neointima response has been observed in these environments after stent implantation [38, 80, 86, 87].

So far, only 2D or idealized 3D computational models and bench-top models have been used to evaluate these relationships. To understand the underlying mechanisms of vascular responses precisely, physiologically correct lesion anatomy, real-world blood flow alternations due to stent implantation and arterial drug deposition need to be exactly correlated in 3D space with the actual vascular responses *in vivo*. To achieve this improved understanding of the interation between devices and vascular pathophysiology, research needs to be conducted to define the *in vivo* endovascular environment precisely and to register the information accurately over time.

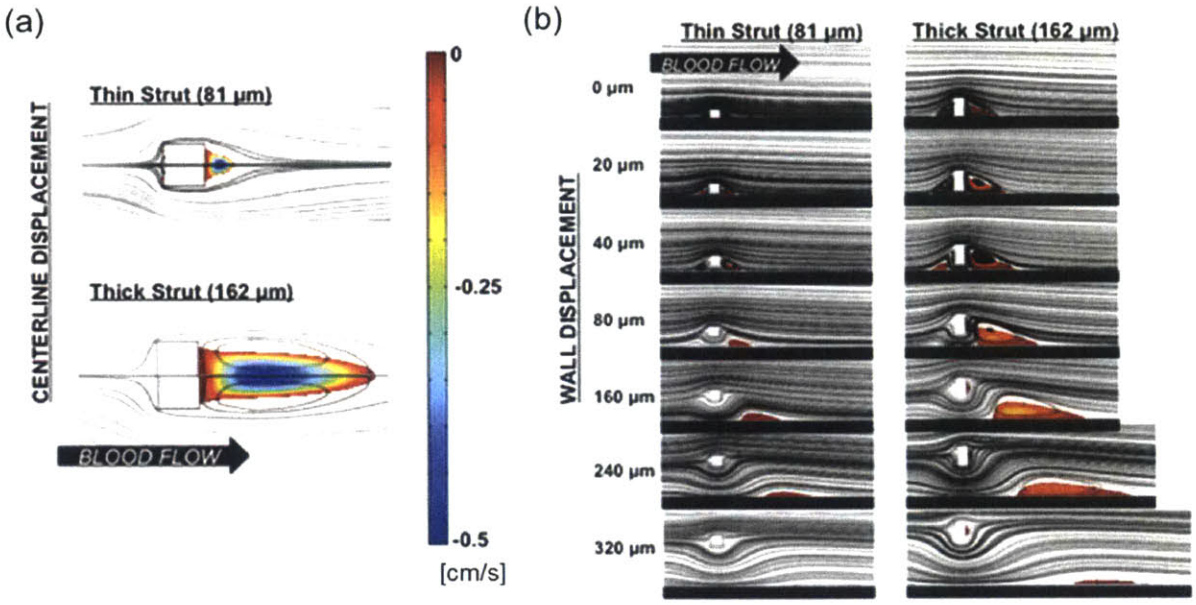

Figure 1-5 Relationship between blood flow pattern and stent-strut location [26]
(a) Thicker stent-struts create greater disturbance of blood flow, which may result in more thrombus formation. (b) Stent malapposition induces the deposition of blood, leading to stent thrombosis.

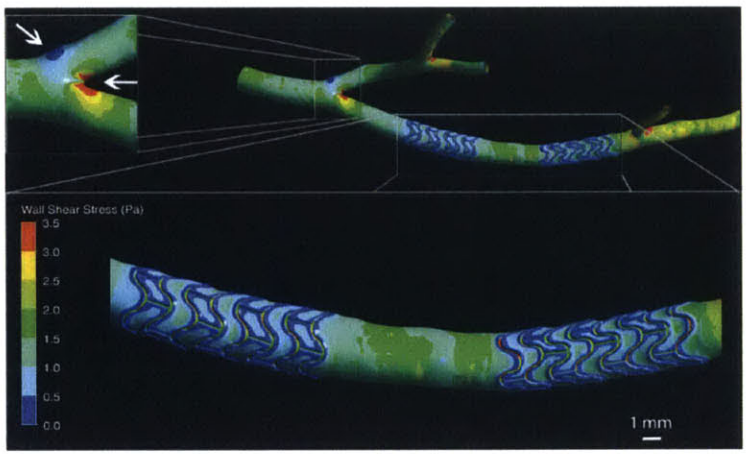

Figure 1-6 Wall shear stress distribution in a porcine left coronary artery with two stents [87]
Within the region where the stent was implanted, wall shear stress is distributed from 0 Pa to 3.5 Pa. The low wall shear stress is observed around stent-struts.

1.3 Reconstruction of Physiologically Realistic Endovascular Environment and Its Long-term Study

1.3.1 Reconstruction of 3D Geometries of Lumen and Stent

The geometries of the lumen and stent in 3D space are typically reconstructed by transforming 2D images into 3D. Computed tomography angiography was first used to reconstruct the 3D structure of coronary arteries [88, 89]. Since these images are acquired in the axial direction, the coronary artery structure can be easily reconstructed by segmenting each image and interpolating between images in the axial direction. However, since this method cannot detect stent-struts due to its limited in-plane resolution (0.5 mm) [88], the stent structure cannot be assessed. Micro-computed tomography, whose in-plane resolution is about 25 μm [90], can be used to detect stent-struts; yet, this imaging modality cannot be used *in vivo* in large animals or humans [91-93].

The structure of coronary arteries can also be reconstructed in 3D space from a pair of coronary angiographic images [94-96]. However, stent-struts cannot be detected in angiographic images because these images show only the silhouette of coronary arteries that are highlighted by radio-opaque contrast dye [97]. Therefore, another imaging modality, i.e., intravascular imaging modalities, that provides intra-luminal information is necessary for reconstructing a stent structure. Since images by IVUS or OCT are acquired perpendicular to the imaging catheter, knowledge of the catheter path in 3D space is required to reconstruct the 3D geometries of the lumen and the stent. Here is where coronary angiography is a very useful imaging modality, and the technique of fusing IVUS or OCT with angiography has been investigated [29, 30, 97-108]. All of these fusion techniques use coronary angiography to reconstruct a 3D fusion path, on which IVUS or OCT images are placed perpendicularly. There are two potential paths for fusion: the imaging catheter path or the vessel centerline (Figure 1-7). The comparison of these two potential fusion paths is summarized in Table 1-2.

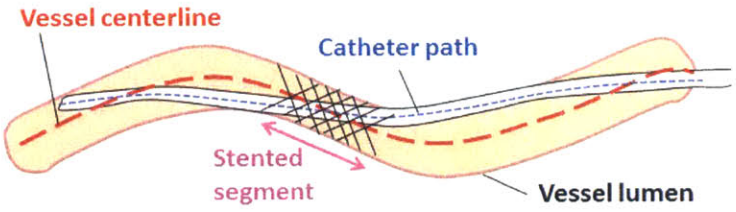

Figure 1-7 Two potential paths for fusion of coronary angiography and IVUS/OCT: Imaging catheter path and vessel centerline

Table 1-2 Comparison of catheter path and vessel centerline as a fusion path

	Catheter path	Vessel centerline
Advantage	• Not affected by cardiac motion • Reconstruct more accurately if ECG-gated IVUS images are used	• Easy angiographic images requirements to satisfy
Disadvantage	• Can move during the procedure • Difficult angiographic images requirements to satisfy	• Affected by cardiac motion
Suitability	Angiography-IVUS fusion	Angiography-IVUS/OCT fusion

For fusion of IVUS and angiography, the end-diastolic IVUS images are placed on the end-diastolic catheter path that is reconstructed from paired coronary angiographic images with partial contrast dye injection [97, 98, 104-108]. While IVUS is more often used for fusion, angiography-OCT fusion may enable more accurate reconstruction of both lumen and stent because of the higher in-plane resolution of OCT [101, 109]. Since OCT images are acquired over 1-2 cardiac cycle(s) due to the fast pullback speed of OCT [19, 98], coregistration in a cardiac cycle between angiography and OCT is impossible, although it is possible for angiography-IVUS fusion. As cardiac motion can generate lateral and longitudinal movements of the OCT imaging catheter relative to the artery, the vessel centerline is used in lieu of the catheter path for angiography-OCT fusion. Papafaklis et al. recently demonstrated with the images from four patients that the usage of the vessel centerline as a fusion path could directly overcome the lateral movement problem and that longitudinal movement of the catheter would

introduce a small error in angiography-OCT fusion [110]. Cardiac motion also induces movement of the coronary arteries themselves, which directly affects the morphology of the vessel centerline. Therefore, this effect needs to be compensated for accurate angiography-OCT fusion. The reproducibility of the vessel centerline reconstruction between different cardiac cycles also needs to be evaluated as angiographic images and IVUS or OCT images are not taken simultaneously.

The methods to reconstruct the vessel centerline also have limitations. These state-of-the-art methods [98, 100, 101, 103, 111, 112] have been validated with the isocentric (i.e., no machine-origin isocenter offset and no movements of object center) and/or orthogonal pair of coronary angiographic images only, both of which conditions are difficult to satisfy in real-world settings. In clinical situations, to obtain a better view, the angiographic images are taken from variable angles and/or by moving the table. Moreover, the patient may move during procedures [30, 113, 114]. Thus, a new vessel centerline reconstruction method, which can handle non-isocentric and non-orthogonal angiographic images, has high reproducibility, and considers the effect of cardiac motion, is needed for accurate 3D reconstruction of lumen and stent structures by angiography-OCT fusion.

1.3.2 Registration of Different Time-point Dataset

Although precise 3D geometries are created at every time-point, i.e., pre- and post-intervention and follow-ups, and an accurate blood flow pattern is computed from the geometry at post-intervention, registration of different time-point datasets is necessary to understand the influence of blood flow patterns on vascular responses to catheter intervention. Currently, time-point registration for long-term studies is conducted in 2D space with OCT images using side branches as landmarks [23]. However, this method is limited by the number of the available side branches, which is usually 2-3 in a 50-mm long coronary artery. More

importantly, the imaging catheter cannot be placed at the exact same position over time (Figure 1-8); and thus, the different time-point images that contain the same side branches may represent a different 2D cross-sectional plane. In PREDICTION study, 3D artery comparison between different time-points was performed by dividing the reconstructed 3D structure in consecutive 3-mm segments [38]. However, this method prevents the understanding of the vascular responses on the stent-strut level (approximately 100 μm level). Therefore, a new time-point registration method in 3D with high accuracy and fine spatial resolution is required to correlate lesion anatomy and blood flow patterns with vascular responses after interventions, so as to understand the underlying mechanisms.

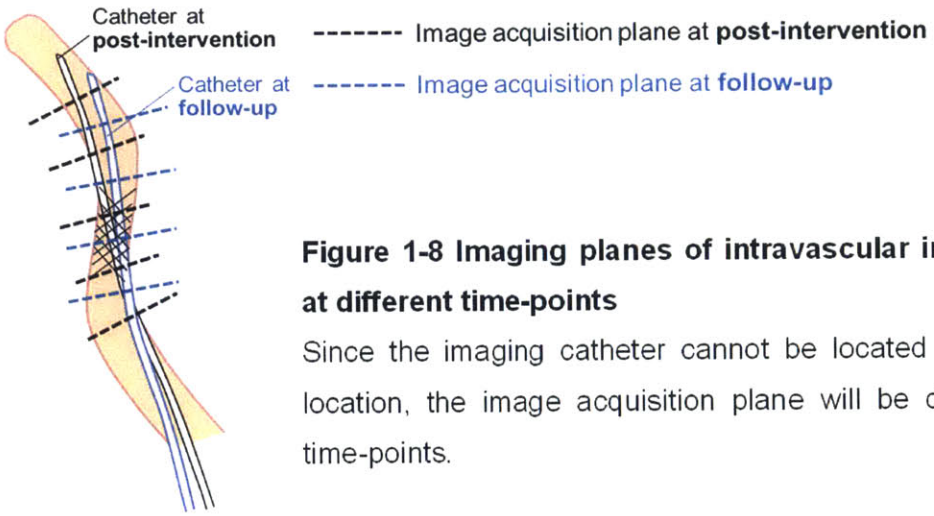

Figure 1-8 Imaging planes of intravascular imaging modalities at different time-points

Since the imaging catheter cannot be located at the exact same location, the image acquisition plane will be different at different time-points.

1.4 Research Goals and Specific Aims

Although innovation in imaging modalities has dramatically improved catheter intervention, especially stent implantation, two limitations prevent the optimization of catheter intervention and the improvement of the treatments for CAD based on the mechanistic understanding of vascular responses to intervention: (i) lack of a method to accurately reconstruct lumen and stent structures in 3D space, and (ii) lack of a method to accurately register these structures over time

in 3D space. The hypothesis governing this thesis is that new methods to reconstruct 3D structures accurately and to register the structures across time can be created by melding different imaging modalities, i.e., coronary angiography and intravascular imaging modalities. Since intravascular images provide us precise information of lumen surface and stent-struts location in 2D space, knowledge of a 3D path is necessary for 3D reconstruction to transform the information at each time-point and for 3D registration across time to transform the information at the different time-points. This thesis focuses on the vessel centerline that is accurately reconstructed from paired coronary angiographic images as a path to reconstruct the structure by fusing with intravascular images, especially OCT images, and to register the reconstructed structures over time. Many methods to reconstruct a vessel centerline have been proposed [98, 100, 101, 103, 111, 112]; however, none of them have been clinically applicable due to their requirements in coronary angiographic images. Therefore, this thesis is proposed with three specific aims to improve the vessel centerline technique and to enable us to reconstruct 3D structures of lumens and stents accurately and register them across time precisely.

Specific Aim 1: Develop a vessel centerline reconstruction method in static phantom models (Chapter 2)

State-of-the-art methods for vessel centerline reconstruction are not applicable to the actual clinical situations. A method will be developed that can reconstruct a vessel centerline from a non-orthogonal and non-isocentric pair of angiographic images. The development in static phantom models allows the evaluation and the understanding of the limitation and precision of this method including determining the reproducibility of the vessel centerline reconstruction.

Specific Aim 2: Validate a vessel centerline reconstruction method and
Develop a structural reconstruction method and a time-point registration method in a preclinical setting (Chapter 3)

First, the vessel centerline reconstruction method will be validated in a preclinical setting

where the influence of cardiac motion is to be considered. Then, I will develop a new structural reconstruction method by fusing coronary angiography and OCT. As OCT images for the stented segment are obtained over a cardiac cycle, this newly developed method will be improved to be made robust to the effect of cardiac motion. Finally, a time-point registration method will be developed using a vessel centerline as a path for registration across time.

Specific Aim 3: Validate the structural reconstruction and the time-point registration methods in a clinical setting (Chapter 4)

The applicability, i.e., the utilization and performance, of the structural reconstruction method and the time-point registration methods will be evaluated using the datasets that are acquired from living patients.

References

1. Roger, V.L., et al., *Heart disease and stroke statistics--2012 update: a report from the American Heart Association.* Circulation, 2012. **125**(1524-4539 (Electronic)): p. e2-e220.
2. World Health Organization Global Health Observatory, *Noncommunicable Diseases (NCD) Mortality and Morbidity.* [cited April 20, 2014]; Available from: http://www.who.int/gho/ncd/mortality_morbidity/en/.
3. World Health Organization, *Cardiovascular Diseases (CVDs) Fact sheet N°317.* 2013 March 2013; Available from: http://www.who.int/mediacentre/factsheets/fs317/en/index.html.
4. World Health Origanization, *Burden: mortality, morbidity and risk factors.* Global Status Report on Noncommunicable Diseases 2010. 2011.
5. Dowe, D.A., M. Fioranelli, and P. Pavone, *Imaging Crororary Arteries.* 2nd ed. 2013: Springer.
6. Dvir, D., et al., *Three-dimensional coronary reconstruction from routine single-plane coronary angiograms: in vivo quantitative validation.* Int J Cardiovasc Intervent, 2005. **7**(1462-8848 (Print)): p. 141-145.
7. Saito, T., et al., *Three-dimensional quantitative coronary angiography.* Biomedical Engineering, IEEE Transactions on, 1990. **37**(8): p. 768-777.
8. Brown, B.G., et al., *Quantitative coronary arteriography: estimation of dimensions, hemodynamic resistance, and atheroma mass of coronary artery lesions using the arteriogram and digital computation.* Circulation, 1977. **55**(2): p. 329-37.
9. Shah, V.M., et al., *Background incidence of late malapposition after bare-metal stent implantation.* Circulation, 2002. **106**(14): p. 1753-5.
10. Yock, P.G., et al., *Intravascular ultrasound guidance for catheter-based coronary interventions.* Journal of the American College of Cardiology, 1991. **17**(6s2): p. 39-45.
11. Kubo, T., et al., *Application of Optical Coherence Tomography in Percutaneous Coronary Intervention.* Circulation Journal, 2012. **76**(9): p. 2076-2083.
12. Adriaenssens, T., et al., *Optical coherence tomography (OCT) in PCI for in-stent restenosis (ISR): rationale and design of the SEDUCE (Safety and Efficacy of a Drug elUting balloon in Coronary artery rEstenosis) study.* Eurointervention, 2011. **7**: p. K100-K105.
13. Johns Hopkins Medicine Health Library, *Angioplasty and Stent Placement for the Heart.* Available from: http://www.hopkinsmedicine.org/healthlibrary/test_procedures/cardiovascular/percutaneous_transluminal_coronary_angioplasty_ptca_and_stent_placement_92,p07981/.
14. Nakazawa, G., *Stent thrombosis of drug eluting stent: Pathological perspective.* Journal of Cardiology, 2011. **58**(2): p. 84-91.

15. Sudhir, K., et al., *Risk factors for coronary drug-eluting stent thrombosis: influence of procedural, patient, lesion, and stent related factors and dual antiplatelet therapy.* ISRN cardiology, 2013. **2013**: p. 748736.
16. Iakovou, I., et al., *Incidence, predictors, and outcome of thrombosis after successful implantation of drug-eluting stents.* JAMA, 2005. **293**(17): p. 2126-2130.
17. Saeed, M.H., Ahmed, I. Nouman, A., *Frequency of stent thrombosis following percutaneous coronary intervention with bare metal versus drug eluting stents.* Pakistan Journal of Cardiology, 2012. **23**: p. 9-17.
18. Lilly, L.S. and Harvard Medical School., *Pathophysiology of heart disease : a collaborative project of medical students and faculty*. 5th ed. 2011, Baltimore, MD: Wolters Kluwer/Lippincott Williams & Wilkins. xiv, 461 p.
19. Jang, I.-K., *Optical Coherence Tomography or Intravascular Ultrasound?* JACC: Cardiovascular Interventions, 2011. **4**(5): p. 492-494.
20. Kubo, T., et al., *Comparison of Vascular Response After Sirolimus-Eluting Stent Implantation Between Patients With Unstable and Stable Angina PectorisA Serial Optical Coherence Tomography Study.* JACC: Cardiovascular Imaging, 2008. **1**(4): p. 475-484.
21. Nair, R.N., *Coronary Stent Fracture: A Review of the Literature.* Cardiac Cath Lab Director, 2011. **1**(1): p. 32-38.
22. Guagliumi, G., et al., *Serial Assessment of Coronary Artery Response to Paclitaxel-Eluting Stents Using Optical Coherence Tomography.* Circulation-Cardiovascular Interventions, 2012. **5**(1): p. 30-38.
23. Gutierrez-Chico, J.L., et al., *Vascular tissue reaction to acute malapposition in human coronary arteries: sequential assessment with optical coherence tomography.* Circ Cardiovasc Interv, 2012. **5**(1): p. 20-9, S1-8.
24. Inoue, T., et al., *Optical coherence evaluation of everolimus-eluting stents 8 months after implantation.* Heart, 2011. **97**(17): p. 1379-1384.
25. Papayannis, A.C., et al., *Optical coherence tomography evaluation of drug-eluting stents: A Systematic Review.* Catheterization and Cardiovascular Interventions, 2013. **81**(3): p. 481-487.
26. Kolandaivelu, K., et al., *Stent thrombogenicity early in high-risk interventional settings is driven by stent design and deployment and protected by polymer-drug coatings.* Circulation, 2011. **123**(13): p. 1400-9.
27. Tanous, D., et al., *Probucol inhibits in-stent thrombosis and neointimal hyperplasia by promoting re-endothelialization.* Atherosclerosis, 2006. **189**(2): p. 342-349.
28. Faugeras, O., Q.-T. Luong, and T.o. Papadopoulo, *The geometry of multiple images : the laws that govern the formation of multiple images of a scene and some of their applications*. 2001,

Cambridge, Mass.: MIT Press. xxiv, 644 p.

29. Bourantas, C.V., et al., *A new methodology for accurate 3-dimensional coronary artery reconstruction using routine intravascular ultrasound and angiographic data: implications for widespread assessment of endothelial shear stress in humans.* EuroIntervention, 2013. **9**(5): p. 582-593.
30. Yang, J., et al., *Novel approach for 3-d reconstruction of coronary arteries from two uncalibrated angiographic images.* IEEE Trans Image Process, 2009. **18**(7): p. 1563-72.
31. National Institutes of Health, National Heart, Lung, and Blood Institute, *Morbidity & Mortality: 2012 Chart Book on Cardiovascular, Lung, and Blood Diseases*. 2012.
32. World Health Organization, *The global burden of disease: 2004 update*. 2008.
33. Tardif, J.-C., *Coronary artery disease in 2010.* European Heart Journal Supplements, 2010. **12**(suppl C): p. C2-C10.
34. Loncar, C.D.M.D., *Projections of Global Mortality and Burden of Disease from 2002 to 2030.* PLoS Medicine, 2006. **3**(11).
35. Heidenreich, P.A., et al., *Forecasting the Future of Cardiovascular Disease in the United States: A Policy Statement From the American Heart Association.* Circulation, 2011. **123**(8): p. 933-944.
36. Kumar, V., et al., *Robbins & Cotran Pathologic Basis of Disease*. 8th ed. 2010, Philadelphia, PA: Saunders/Elsevier. xiv, 1450 p.
37. Takumi, T., et al., *Coronary endothelial dysfunction is associated with a reduction in coronary artery compliance and an increase in wall shear stress.* Heart, 2010. **96**(10): p. 773-778.
38. Stone, P.H., et al., *Prediction of progression of coronary artery disease and clinical outcomes using vascular profiling of endothelial shear stress and arterial plaque characteristics: the PREDICTION Study.* Circulation, 2012. **126**(2): p. 172-81.
39. Lilly, L.S. and Harvard Medical School., *Pathophysiology of heart disease : a collaborative project of medical students and faculty*. 3rd ed. 2003, Philadelphia: Lippincott Williams & Wilkins. xiii, 445 p.
40. Dotter, C.T. and M.P. Judkins, *Transluminal Treatment of Arteriosclerotic Obstruction. Description of a New Technic and a Preliminary Report of Its Application.* Circulation, 1964. **30**: p. 654-70.
41. Dotter, C.T. and M.P. Judkins, *Transluminal Treatment of Arteriosclerotic Obstruction. Description of a New Technic and a Preliminary Report of Its Application.* Circulation, 1964. **30**: p. 654-670.
42. Gruentzig, A.R., A. Senning, and W.E. Siegenthalea, *Nonoperative dilation of coronary-artery stenosis: percutaneous transluminal coronary angioplasty.* New England Journal of Medicine, 1979. **30**: p. 61-68.

43. Liu, M.W., G.S. Roubin, and S.B. King, 3rd, *Restenosis after coronary angioplasty. Potential biologic determinants and role of intimal hyperplasia.* Circulation, 1989. **79**(6): p. 1374-87.
44. Rivard, A. and V. Andres, *Vascular smooth muscle cell proliferation in the pathogenesis of atherosclerotic cardiovascular diseases.* Histol Histopathol, 2000. **15**(2): p. 557-71.
45. Serruys, P.W., M.J. Kutryk, and A.T. Ong, *Coronary-artery stents.* N Engl J Med, 2006. **354**(5): p. 483-95.
46. Lanzer, P., et al., *The need for stent-lesion matching to optimize outcomes of intracoronary stent implantation.* Journal of Biomedical Materials Research Part B-Applied Biomaterials, 2013. **101**(8): p. 1560-1570.
47. Brilakis, E.S., V.G. Patel, and S. Banerjee, *Medical management after coronary stent implantation: A review.* JAMA, 2013. **310**(2): p. 189-198.
48. Eisenberg, M.J., *Drug-Eluting Stents: The Price Is Not Right.* Circulation, 2006. **114**(16): p. 1745-1754.
49. Hirshfeld, J.W. and R.L. Wilensky, *Drug-eluting stents are here--now what? Implications for clinical practice and health care costs.* Cleveland Clinic Journal of Medicine, 2004. **71**(10): p. 825-828.
50. Head, S.J., A.J. Bogers, and A.P. Kappetein, *Drug-eluting stent implantation for coronary artery disease: current stents and a comparison with bypass surgery.* Curr Opin Pharmacol, 2012. **12**(2): p. 147-54.
51. Luescher, T.F., et al., *Drug-eluting stent and coronary thrombosis - Biological mechanisms and clinical implications.* Circulation, 2007. **115**(8): p. 1051-1058.
52. Hillis, L.D., et al., *2011 ACCF/AHA Guideline for Coronary Artery Bypass Graft SurgeryA Report of the American College of Cardiology Foundation/American Heart Association Task Force on Practice Guidelines Developed in Collaboration With the American Association for Thoracic Surgery, Society of Cardiovascular Anesthesiologists, and Society of Thoracic Surgeons.* Journal of the American College of Cardiology, 2011. **58**(24): p. e123-e210.
53. Epstein, A.J., et al., *Coronary Revascularization Trends in the United States: 2001–2008.* JAMA : the journal of the American Medical Association, 2011. **305**(17): p. 1769-1776.
54. Thompson, C.A., *Textbook of Cardiovascular Intervention.* 1 ed. 2014: Springer. XVI, 545.
55. Costa, M.A., et al., *Impact of Stent Deployment Procedural Factors on Long-Term Effectiveness and Safety of Sirolimus-Eluting Stents (Final Results of the Multicenter Prospective STLLR Trial).* Am J Cardiol, 2008. **101**(12): p. 1704-1711.
56. Reiber, J.H.C., et al., *QCA, IVUS and OCT in interventional cardiology in 2011.* Cardiovascular Diagnosis and Therapy, 2011. **1**(1): p. 57-70.
57. Serruys, P.W., D.P. Foley, and P.J.d. Feyter, *Quantitative Coronary Angiography in Clinical Practice.* Developments in Cardiovascular Medicine. 1994: Springer. XXII, 722.

58. Nissen, S.E., et al., *Intravascular ultrasound assessment of lumen size and wall morphology in normal subjects and patients with coronary artery disease.* Circulation, 1991. **84**(3): p. 1087-99.
59. Nair, A., et al., *Coronary plaque classification with intravascular ultrasound radiofrequency data analysis.* Circulation, 2002. **106**(17): p. 2200-6.
60. Bezerra, H.G., et al., *Intracoronary optical coherence tomography: a comprehensive review clinical and research applications.* JACC Cardiovasc Interv, 2009. **2**(11): p. 1035-46.
61. Gonzalo, N., et al., *Reproducibility of quantitative optical coherence tomography for stent analysis.* Eurointervention, 2009. **5**(2): p. 224-32.
62. Murata, A., et al., *Accuracy of optical coherence tomography in the evaluation of neointimal coverage after stent implantation.* JACC Cardiovasc Imaging, 2010. **3**(1): p. 76-84.
63. Suzuki, Y., et al., *In vivo comparison between optical coherence tomography and intravascular ultrasound for detecting small degrees of in-stent neointima after stent implantation.* JACC Cardiovasc Interv, 2008. **1**(2): p. 168-73.
64. Templin, C., et al., *Coronary optical frequency domain imaging (OFDI) for in vivo evaluation of stent healing: comparison with light and electron microscopy.* Eur Heart J, 2010. **31**(14): p. 1792-801.
65. Witzenbichler, B., et al., *Relationship Between Intravascular Ultrasound Guidance and Clinical Outcomes After Drug-Eluting Stents: The Assessment of Dual Antiplatelet Therapy With Drug-Eluting Stents (ADAPT-DES) Study.* Circulation, 2014. **129**(4): p. 463-470.
66. Alfonso, F., et al., *Combined use of optical coherence tomography and intravascular ultrasound imaging in patients undergoing coronary interventions for stent thrombosis.* Heart, 2012. **98**(16): p. 1213-1220.
67. Cook, S., et al., *Impact of incomplete stent apposition on long-term clinical outcome after drug-eluting stent implantation.* European Heart Journal, 2012. **33**(11): p. 1334-1343.
68. Foin, N., et al., *Incomplete stent apposition causes high shear flow disturbances and delay in neointimal coverage as a function of strut to wall detachment distance: implications for the management of incomplete stent apposition.* Circulation. Cardiovascular interventions, 2014. **7**(2): p. 180-9.
69. Gutierrez-Chico, J.L., et al., *Vascular Tissue Reaction to Acute Malapposition in Human Coronary Arteries Sequential Assessment With Optical Coherence Tomography.* Circulation-Cardiovascular Interventions, 2012. **5**(1): p. 20-U81.
70. Hong, M.K., et al., *Late stent malapposition after drug-eluting stent implantation: an intravascular ultrasound analysis with long-term follow-up.* Circulation, 2006. **113**(3): p. 414-9.
71. Im, E., et al., *Incidences, predictors, and clinical outcomes of acute and late stent malapposition detected by optical coherence tomography after drug-eluting stent implantation.*

Circulation. Cardiovascular interventions, 2014. **7**(1): p. 88-96.

72. Kim, B.K., et al., *Relationship between Stent Malapposition and Incomplete Neointimal Coverage after Drug-Eluting Stent Implantation.* Journal of Interventional Cardiology, 2012. **25**(3): p. 270-277.
73. Kim, B.K., et al., *Optical coherence tomography-based evaluation of malapposed strut coverage after drug-eluting stent implantation.* International Journal of Cardiovascular Imaging, 2012. **28**(8): p. 1887-1894.
74. Nakamura, M., et al., *Late incomplete stent apposition and focal vessel expansion after bare metal stenting.* Am J Cardiol, 2003. **92**(10): p. 1217-9.
75. Parodi, G., et al., *Stent-related defects in patients presenting with stent thrombosis: differences at optical coherence tomography between subacute and late/very late thrombosis in the Mechanism Of Stent Thrombosis (MOST) study.* Eurointervention, 2013. **9**(8): p. 936-944.
76. Ragkousis, G.E., N. Curzen, and N.W. Bressloff, *Simulation of longitudinal stent deformation in a patient-specific coronary artery.* Medical engineering & physics, 2014. **36**(4): p. 467-76.
77. Santos, M.C., T. Lin, and P. Barlis, *In-stent restenosis associated with stent malapposition: Seven year optical coherence tomography findings.* Int J Cardiol, 2011. **147**(1): p. 149-151.
78. Shimamura, K., et al., *Serial Changes of Everolimus-eluting Stent Malapposition: An Optical Coherence Tomography Subanalysis from the RESET Trial.* American Journal of Cardiology, 2013. **111**(7): p. 38B-39B.
79. Hong, M.K., et al., *Incidence, mechanism, predictors, and long-term prognosis of late stent malapposition after bare-metal stent implantation.* Circulation, 2004. **109**(7): p. 881-886.
80. Chen, H.Y., et al., *Impact of stent mis-sizing and mis-positioning on coronary fluid wall shear and intramural stress.* Journal of Applied Physiology, 2013. **115**(2): p. 285-292.
81. Balakrishnan, B., et al., *Thrombus causes fluctuations in arterial drug delivery from intravascular stents.* J Control Release, 2008. **131**(3): p. 173-80.
82. Balakrishnan, B., et al., *Intravascular drug release kinetics dictate arterial drug deposition, retention, and distribution.* J Control Release, 2007. **123**(2): p. 100-8.
83. Balakrishnan, B., et al., *Strut position, blood flow, and drug deposition: implications for single and overlapping drug-eluting stents.* Circulation, 2005. **111**(22): p. 2958-65.
84. O'Brien, C.C., et al., *Impact of flow pulsatility on arterial drug distribution in stent-based therapy.* Journal of Controlled Release, 2013. **168**(2): p. 115-124.
85. Tzafriri, A.R., et al., *Lesion complexity determines arterial drug distribution after local drug delivery.* J Control Release, 2010. **142**(3): p. 332-8.
86. Stone, P.H., et al., *Effect of endothelial shear stress on the progression of coronary artery disease, vascular remodeling, and in-stent restenosis in humans: in vivo 6-month follow-up*

study. Circulation, 2003. **108**(4): p. 438-44.

87. Rikhtegar, F., et al., *Compound Ex Vivo and In Silico Method for Hemodynamic Analysis of Stented Arteries.* Plos One, 2013. **8**(3).
88. Schoepf, U.J., et al., *CT of coronary artery disease.* Radiology, 2004. **232**(1): p. 18-37.
89. Achenbach, S., et al., *Noninvasive coronary angiography by retrospectively ECG-gated multislice spiral CT.* Circulation, 2000. **102**(23): p. 2823-2828.
90. Stephenson, R.S., et al., *Contrast Enhanced Micro-Computed Tomography Resolves the 3-Dimensional Morphology of the Cardiac Conduction System in Mammalian Hearts.* Plos One, 2012. **7**(4): p. e35299.
91. Detombe, S.A., et al., *Longitudinal Follow-up of Cardiac Structure and Functional Changes in an Infarct Mouse Model Using Retrospectively Gated Micro-Computed Tomography.* Investigative Radiology, 2008. **43**(7).
92. Song, J., et al., *Sparseness prior based iterative image reconstruction for retrospectively gated cardiac micro-CT.* Medical Physics, 2007. **34**(11): p. 4476-4483.
93. Butcher, J.T., et al., *Quantitative volumetric analysis of cardiac morphogenesis assessed through micro-computed tomography.* Developmental Dynamics, 2007. **236**(3): p. 802-809.
94. Andriotis, A., et al., *A new method of three-dimensional coronary artery reconstruction from X-ray angiography: Validation against a virtual phantom and multislice computed tomography.* Catheterization and Cardiovascular Interventions, 2008. **71**(1): p. 28-43.
95. Chen, S.Y., J.C. Carroll Jd Fau - Messenger, and J.C. Messenger, *Quantitative analysis of reconstructed 3-D coronary arterial tree and intracoronary devices.* IEEE Transactions on Medical Imaging, 2002. **21**(7): p. 724-749.
96. Sprague, K., et al., *Coronary x-ray angiographic reconstruction and image orientation.* Medical Physics, 2006. **33**(3): p. 707-718.
97. Bourantas, C.V., et al., *A method for 3D reconstruction of coronary arteries using biplane angiography and intravascular ultrasound images.* Computerized Medical Imaging and Graphics, 2005. **29**(8): p. 597-606.
98. Athanasiou, L.S., et al. *3D Reconstruction of Coronary Arteries using Frequency Domain Optical Coherence Tomography Images and Biplane Angiography.* in *34th Annual International Conference of the IEEE Engineering-in-Medicine-and-Biology-Society (EMBS).* 2012. San Diego, CA.
99. Khaleel, H.H., et al., *A Review paper of 3D Surface Reconstruction of Coronary Arteries From Cardiovascular Angiography.* 2012 International Conference on Advanced Computer Science Applications and Technologies (Acsat), 2012: p. 419-435.
100. Sarwal, A. and A.P. Dhawan, *Three dimensional reconstruction of coronary arteries from two views.* Computer Methods and Programs in Biomedicine, 2001. **65**(1): p. 25-43.

101. Tu, S., et al., *Fusion of 3D QCA and IVUS/OCT.* Int J Cardiovasc Imaging, 2011. **27**(2): p. 197-207.

102. Tu, S.X., et al., *In vivo comparison of arterial lumen dimensions assessed by co-registered three-dimensional (3D) quantitative coronary angiography, intravascular ultrasound and optical coherence tomography.* International Journal of Cardiovascular Imaging, 2012. **28**(6): p. 1315-1327.

103. van der Giessen, A.G., et al., *3D fusion of intravascular ultrasound and coronary computed tomography for in-vivo wall shear stress analysis: a feasibility study.* International Journal of Cardiovascular Imaging, 2010. **26**(7): p. 781-796.

104. Bourantas, C.V., et al., *ANGIOCARE: An automated system for fast three-dimensional coronary reconstruction by integrating angiographic and intracoronary ultrasound data.* Catheterization and Cardiovascular Interventions, 2008. **72**(2): p. 166-175.

105. Ellwein, L.M., et al., *Optical Coherence Tomography for Patient-specific 3D Artery Reconstruction and Evaluation of Wall Shear Stress in a Left Circumflex Coronary Artery.* Cardiovascular Engineering and Technology, 2011. **2**(3): p. 212-227.

106. Subramanian, K.R., et al., *Accurate 3D reconstruction of complex blood vessel geometries from intravascular ultrasound images: in vitro study.* Journal of Medical Engineering & Technology, 2000. **24**(4): p. 131-140.

107. Zhang, W., Z. Chen, and X. Zhang, *3D Vessel Tree Reconstruction from Rotational C-arm Projections by Multi-view Stereo Reconstruction*, in *Apcmbe 2008: 7th Asian-Pacific Conference on Medical and Biological Engineering*, Y. Peng and X. Weng, Editors. 2008. p. 434-441.

108. Hoffmann, K.R., et al., *Biplane X-ray angiograms, intravascular ultrasound, and 3D visualization of coronary vessels.* Int J Card Imaging, 1999. **15**(6): p. 495-512.

109. Bourantas, C.V., et al., *Bioresorbable vascular scaffold treatment induces the formation of neointimal cap that seals the underlying plaque without compromising the luminal dimensions: a concept based on serial optical coherence tomography data.* EuroIntervention, 2014.

110. Papafaklis, M.I., et al., *Anatomically correct three-dimensional coronary artery reconstruction using frequency domain optical coherence tomographic and angiographic data: head-to-head comparison with intravascular ultrasound for endothelial shear stress assessment in humans.* . EuroIntervention, 2014(1969-6213 (Electronic)).

111. Tu, S.X., et al., *Assessment of obstruction length and optimal viewing angle from biplane X-ray angiograms.* International Journal of Cardiovascular Imaging, 2010. **26**(1): p. 5-17.

112. Slager, C.J., et al., *True 3-Dimensional Reconstruction of Coronary Arteries in Patients by Fusion of Angiography and IVUS (ANGUS) and Its Quantitative Validation.* Circulation, 2000.

102(5): p. 511-516.

113. Dumay, A.C.M., J. Reiber, and J.J. Gerbrands, *Determination of optimal angiographic viewing angles: basic principles and evaluation study.* Medical Imaging, IEEE Transactions on, 1994. **13**(1): p. 13-24.

114. Wunderlich, W., et al., *Analytic isocenter calibration. A new approach for accurate x-ray gantries.* Angiology, 1995. **46**(7): p. 577-82.

CHAPTER 2:

DEVELOPMENT OF VESSEL CENTERLINE RECONSTRUCTION IN STATIC PHANTOM MODELS

2.1 Abstract

A physiologically realistic endovascular environment can be reconstructed by transforming, from 2D to 3D, precise information of lumen surface and stent-struts locations obtained from 2D intravascular images. Since the intravascular images are acquired perpendicularly to the imaging catheter, the knowledge of a 3D path where the 2D information is placed is required for this transformation. This knowledge needs to be obtained from another imaging modality that can provide longitudinal information of a coronary artery and/or the imaging catheter. Coronary angiography can be used as the secondary imaging modality, and many methods to reconstruct a fusion path from paired angiographic images have been proposed [1-13]. The vessel centerline is often used as a fusion path especially for the fusion of angiography with optical coherence tomography images; however, the state-of-the-art vessel centerline reconstruction methods have limitations in spatial and temporal alignments. Many of these methods have been validated for isocentric and orthogonal paired angiographic images; and yet, most of the images are acquired from non-isocentric and non-orthogonal views in a clinical setting. In addition, no methods have considered the effect of cardiac motion, which can influence vessel centerline reconstruction. To reconstruct more physiologically realistic structures of lumen and stent by fusing coronary angiography and optical coherence tomography, a new method that can reconstruct the vessel centerline more accurately by overcoming these spatial and temporal alignment challenges is required. In this chapter, a new vessel centerline reconstruction method that can solve the spatial alignment problems is developed and validated using static phantom models.

2.2 Background

Intravascular images, such as those obtained from intravascular ultrasound (IVUS) and optical coherence tomography (OCT), provide information of the lumen surface, the plaque components, and the locations of stent-struts in 2D cross-sectional planes [14-22]. To reconstruct anatomically correct structures of the lumen and the stent, this information needs to be transformed from 2D to 3D. Since all IVUS and OCT images are acquired along a plane that is perpendicular to their imaging catheter, this transformation requires the knowledge of the 3D location of the imaging catheter. To obtain this knowledge, another imaging modality that can provide the correct 3D representation of the coronary artery and/or the 3D location of the imaging catheter within the artery is necessary. Coronary angiography is the most practical option for this secondary imaging modality, and many studies have attempted to develop a technique that fuses coronary angiography and intravascular imaging modalities to reconstruct the 3D structures of lumen and stent [1-6, 8, 9, 23-28]. This thesis focuses on angiography-OCT fusion as a means for 3D reconstruction of lumen and stent structures since OCT has higher in-plane resolution (12-15 μm) than IVUS (150 μm) [14], enabling more precise detection of stent-struts in 2D [4, 29]. Due to the fast pullback speed of OCT [3, 14], the images of an entire stented segment with OCT are acquired over approximately a single cardiac cycle without ECG-gating, while they are acquired at a certain cardiac phase with IVUS. In addition, the imaging catheter can move laterally and longitudinally with the cardiac motion during a single cardiac cycle, preventing fusing the OCT images onto the imaging catheter path that is reconstructed from a certain cardiac phase, unlike angiography-IVUS fusion. Therefore, a usage of a vessel centerline as a fusion path is more appropriate than that of an imaging catheter path for angiography-OCT fusion [30]; and thus, this thesis specifically focuses on the vessel centerline.

The accuracy of 3D structural reconstruction from angiography-OCT fusion relies on the accuracy of the vessel centerline reconstruction because the information of lumen surface and

stent-strut locations in 2D is quite accurate thanks to the high in-plane resolution of OCT. Therefore, the reconstruction of the vessel centerline from paired planar angiographic images is important, and many vessel centerline reconstruction methods have been proposed [1, 6, 8, 31]. For example, Yang et al. [6] used the projection matrix, which describes the relationship between 3D geometries and projected 2D geometries. Bourantas et al. [8] found the intersection points of two 2D vessel centerlines by sweeping the projection plane along a direction perpendicular to the image. However, these state-of-the-art methods have limitations. First, all of these methods have been validated for the isocentric (no machine-origin isocenter offset or no movements of object center) and orthogonal pair of angiographic images. Although some of these methods have already been used in the clinical protocols, the two angiographic images are often non-isocentric and non-orthogonal in clinical practice because (i) the C-arm fluoroscopic angiography system itself has an isocenter offset, (ii) physicians may take images from various positions and may move the table during the procedure to obtain better views, and (iii) patients themselves may move during the procedure. Second, no methods have considered the effect of the cardiac motion. Since cardiac motion itself can induce a morphological change of the coronary arteries, the reconstruction of the vessel centerline could be influenced by it. This influence can be avoided if angiographic images are obtained at the same cardiac phases using an ECG-gating function; however, most of them are acquired without ECG-gating for practical reasons, although the coronary angiography system does have such a function (Figure 2-1, Table 2-1). Therefore, a new vessel centerline reconstruction method that can overcome these limitations is necessary to enable reconstructing more accurate and physiologically realistic 3D structures of the lumen and the stent by angiography-OCT fusion.

In this chapter, a vessel centerline reconstruction method that can handle a non-isocentric and non-orthogonal pair of angiographic images is developed based on stereoscopic theory [32] using static phantom models. The static error, i.e., precision and limitation, of this method is evaluated.

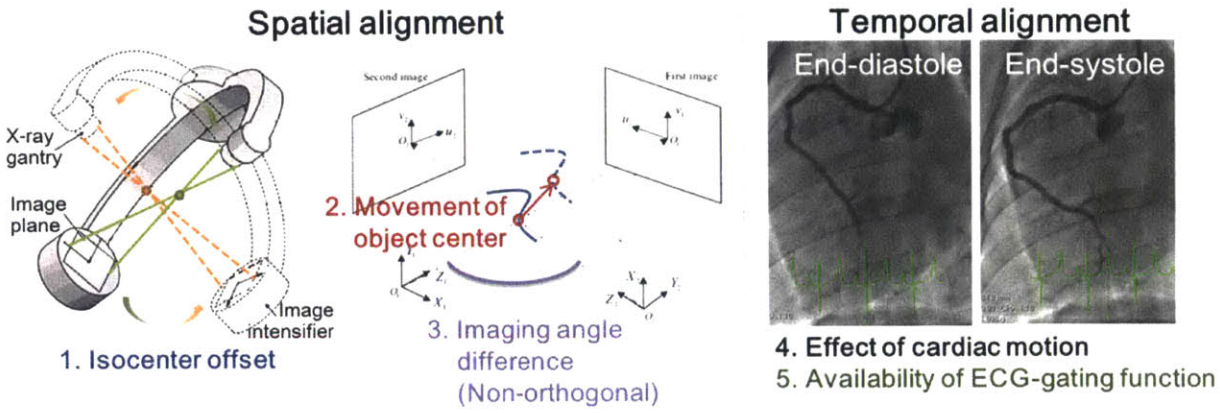

Figure 2-1 Five challenges in vessel centerline reconstruction method

1) Isocenter offset: The C-arm fluoroscopic angiography system itself has an isocenter offset.

2) Movement of the object center: Physicians may move the table during the procedure and/or patients themselves may move during the procedure.

3) Non-orthogonal views: A pair of images is often taken from non-orthogonal position to obtain better views.

4) Effect of cardiac motion: The morphological change in coronary arteries due to the cardiac motion may influence the vessel centerline reconstruction.

5) Availability of ECG-gating function: Most angiographic images are acquired without ECG-gating, which prevents us from avoiding the influence of the cardiac motion by selecting a specific cardiac phase.

Table 2-1 Comparison between the state-of-the-art methods and the proposed method

	Bourantas et al. [1]	Yang et al. [6]	Proposed method
Purpose for…	Angiography + IVUS, Native artery	Angiography (2D →3D), Native artery	Angiography + OCT, Stented artery
1. Isocenter offset	×	✓	✓
2. Movement of object center	×	✓	✓
3. Imaging angle difference	×	×	✓
4. Effect of cardiac motion	×	×	✓
5. Availability of ECG-gating function	×	×	✓

*Red box indicates the challenges that are addressed in this chapter.

2.3 Materials and Methods

2.3.1 Static Phantom Models

Static phantom models should satisfy the following requirements: (i) they can mimic geometries of human coronary arteries, (ii) they have matched mechanical properties to those of human native coronary arteries, (iii) their structures can be visualized with standard angiographic procedures, and (iv) stents can be placed inside them using unmodified intravascular interventional devices. Our laboratory has previously developed phantom models that satisfy all of these requirements [33]. Non-stented and stented (3.0 mm × 17 mm stent was placed) Y-shaped planar phantom models were used.

2.3.2 Image Acquisition

First, both phantom models were filled with radio-opaque contrast dye at a clinical usage concentration (contrast dye : saline = 1:1). Then, after confirming that isocenters were coincident from any projection angles, angiographic images were acquired at a rate of 30 frames/s while varying the projection angle to create the range of the angle between paired images from 20^0 to 130^0. To create a non-isocentric pair of angiographic images, the imaging table was moved on the horizontal plane with the maximum distance that the entire phantom model can be visualized in the angiographic images without changing the magnification. This criterion was determined based on the opinion from the catheter interventional physician. Then, the angiographic images were acquired again from various projection angles that were similar to the ones for isocentric images. All angiographic images were obtained with Innova 2100 (GE Healthcare, Cleveland, OH) at CBSET, Inc. (Lexington, MA) and stored in the DICOM format with all the imaging parameters, i.e., the position of the angiography system and the magnification of the images. The movement of the table was also recorded in the DICOM header. The resolutions of all angiographic images were 0.35 mm/pixel ± 0.04 mm/pixel.

2.3.3 Image Processing Software

All image processing algorithms, e.g., image analysis, mathematical and mechanistic model creation, and development of new computational frameworks, were created with MATLAB (MathWorks, Natick, MA). MATLAB is suitable because it has its own validated and easy-to-use functions for image processing and statistical analysis, and furthermore can incorporate a programming language to create algorithms for specialized commands based on our needs.

2.3.4 Vessel Centerline Reconstruction Method

Overall, the vessel centerline reconstruction method has four steps:

Step 1 – Select specific cardiac phase

Step 2 – Extract vessel centerline candidates in 2D images

Step 3 – Find corresponding points in paired images with epipolar constraints

Step 4 – Reconstruct in 3D space

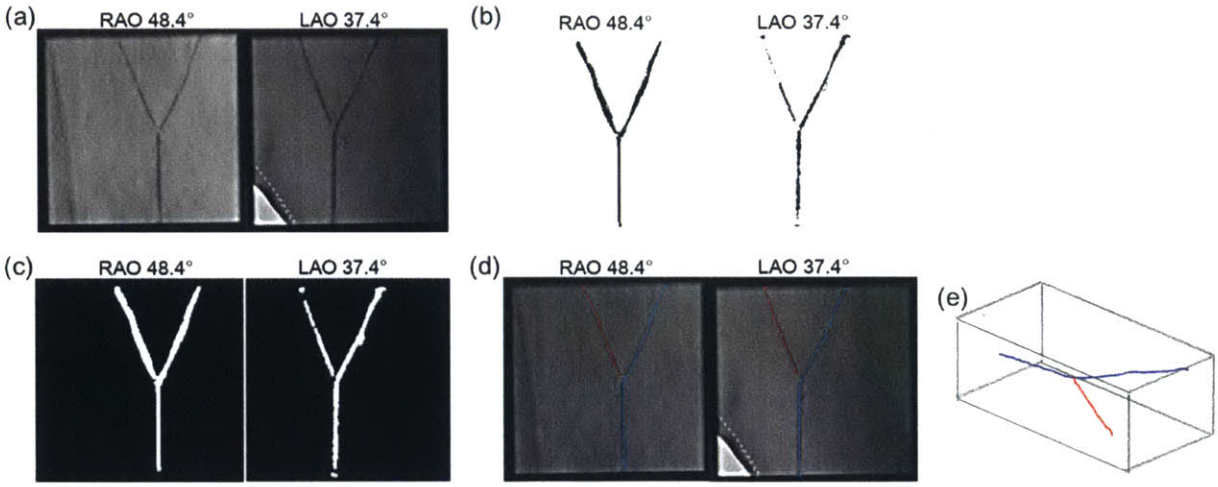

Figure 2-2 Steps of vessel centerline reconstruction

Selected images are imported to MATLAB **(a)**, and thresholded manually to make binary images **(b)**. Then, the edge is detected and the inside is filled morphologically **(c)**. After that, the images are skeletonized to yield the centerline candidates **(d)**. Finally, the corresponding pairs of points in both images are identified by applying epipolar constraints, and the centerline is reconstructed using stereoscopic relations **(e)**.

2.3.4.1 Step 1 – Select Specific Cardiac Phase

This step is required only in preclinical and clinical settings. The detailed explanation of cardiac phase selection is provided in 3.3.4.1.

2.3.4.2 Step 2 – Extract Vessel Centerline Candidates in 2D Images

First the selected images were imported to MATLAB and the contrast of the images was adjusted manually to enhance structures (Figure 2-2(a)). Then, the images were thresholded manually and binary images of the area of interest with approximately 5 mm margin were created (Figure 2-2(b)). Next, Sobel edge detection method was applied to the binary images, and the insides of the detected edges were filled morphologically (Figure 2-2(c)). The filled images were skeletonized to yield candidates of the centerline (Figure 2-2(d)). The edges of the skeletonized results, i.e., the skeletonized results in the marginal areas, were eliminated to remove the spurious nodes, which are obviously not centerline candidates but created through the skeletonization process.

2.3.4.3 Step 3 – Find Corresponding Points in Paired Images with Epipolar Constraints

Epipolar constraints identify corresponding points between two images [32]. These constraints arises from the existence of two viewpoints, either two different cameras at the same time or two different instants with one camera [32]. The two images are assumed to be obtained by pinhole cameras with a distinct optical center, i.e., viewpoints. Under this assumption, the relationship between $\boldsymbol{u_{1,i}}$, a projective coordinate vector of a point $u_{1,i}$ on the first image, and $\boldsymbol{l_{2,u1,i}}$, a projective coordinate vector of its corresponding epipolar line $l_{2,u1,i}$ on the second image is projective linear (Figure 2-3) and can be described with the 3×3 matrix, Fundamental matrix $\boldsymbol{F}$.

$$\boldsymbol{l_{2,u1,i}} \approx \boldsymbol{F u_{1,i}} \tag{2-1}$$

Since the corresponding point $u_{2,i}$ on the second image belongs to the line $l_{2,u1,i}$, a projective coordinate vector of $\boldsymbol{u_{2,i}}$ should satisfy the following equation.

$$\boldsymbol{u_{2,i}}^T \boldsymbol{F}\, \boldsymbol{u_{1,i}} = 0 \tag{2-2}$$

When the roles of the two images are reversed, the Fundamental matrix $\boldsymbol{F}$ is changed to its transpose. Therefore, the following relationship is derived.

$$\boldsymbol{u_{2,i}}^T \boldsymbol{F}\, \boldsymbol{u_{1,i}} = \boldsymbol{u_{1,i}}^T \boldsymbol{F}^T \boldsymbol{u_{2,i}} = 0 \tag{2-3}$$

In the case of finding corresponding points in two paired images with epipolar constraints, potential pairs of corresponding points are assumed to be given. Pairs are randomly chosen from these potential pairs and a Fundamental matrix $\boldsymbol{F}$ is calculated until the Fundamental matrix with which maximum pairs can satisfy Equation 2-3 is found. These pairs become the final corresponding points in the paired images.

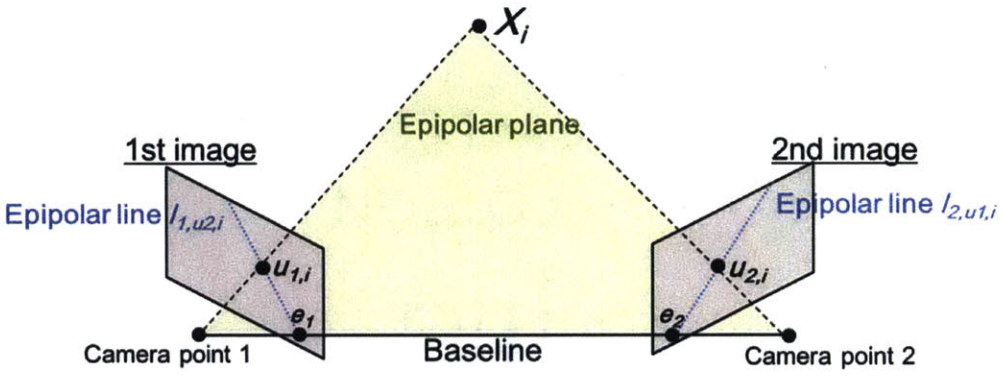

Figure 2-3 Epipolar constraint

Epipolar plane for each 3D point $\boldsymbol{X_i}$ is defined by $\boldsymbol{X_i}$ and two camera points. Epipolar lines are defined as the intersections of the Epipolar plane and 2D image planes. Since the points $u_{1,i}$ and $u_{2,i}$ are the projection of $\boldsymbol{X_i}$ to each 2D image plane, they are on the epipolar line in each plane.

From the centerline candidates that are extracted in Step 2, the potential corresponding point pairs between two projected angiographic images were selected based on the vertical distance from the bifurcation between the stented artery and the side branch. The magnifications were adjusted if they were different between the two images during this process. Then, the final corresponding pairs were identified by applying epipolar constraints three times: (i) only for the main segment (stented segment for the stented phantom model and in preclinical and clinical settings) (blue line in Figure 2-2(d)), (ii) only for the sub-segment (nearest side branch in

preclinical and clinical settings) (red line in Figure 2-2(d)), and (iii) for all the identified points in (i) and (ii). The epipolar constraints were applied three times to accommodate the difference in lengths of the stented artery and the nearest side branch in preclinical and clinical settings. To select the inliers, i.e., find corresponding point pairs from the potential pairs, random sample consensus (RANSAC) method was used for (i) and (ii), and least trimmed squares (LTS) method was used for (iii). RANSAC method is appropriate for the first two steps (i) and (ii) since the distance threshold between the point and epipolar line can be set, while LTS method is appropriate for (iii) because this method enables setting the minimum percentage of inliers, which allows including as many pairs that already meet correspondence at (i) and (ii) as possible can be included.

2.3.4.4 Step 4 – Reconstruct in 3D Space

From the corresponding pairs that were found in Step 3, the centerline was reconstructed in 3D space using projection matrix $\boldsymbol{P}$ (Figure 2-2(e)). This projection matrix $\boldsymbol{P}$ was derived mathematically from the stereoscopic theory [32] that describes the relationship between the actual 3D geometry (x, y, z) and the projected 2D geometry $(u,v) = (r_u/r_w,\ r_v/r_w)$ based on the rotation and the magnification of the imaging system, i.e., coronary angiography system (Equations 2-4 - 2-7, Figure 2-4). The first matrix of the projection matrix $\boldsymbol{P}$ represents intrinsic characteristics of the imaging system and the second matrix represents the rotation and the translation of the imaging plane. All the information of rotations and magnifications of the angiography system were recorded in the DICOM header.

$$[r_u \quad r_v \quad r_w]^T = \boldsymbol{P}[x \quad y \quad z \quad 1]^T \tag{2-4}$$

$$\boldsymbol{P} = \begin{bmatrix} -SID \cdot U/IS & 0 & U/2 \\ 0 & SID \cdot V/IS & V/2 \\ 0 & 0 & 1 \end{bmatrix} \begin{bmatrix} \ddots & & 0 \\ & \boldsymbol{R}_{PA} \cdot \boldsymbol{R}_{SA} & 0 \\ & \ddots & -SOD \end{bmatrix} \tag{2-5}$$

$$\boldsymbol{R}_{PA} = \begin{bmatrix} \cos\theta & 0 & -\sin\theta \\ 0 & 1 & 0 \\ \sin\theta & 0 & \cos\theta \end{bmatrix} \tag{2-6}$$

$$\boldsymbol{R}_{SA} = \boldsymbol{u}\boldsymbol{u}^T + \cos\phi\left(\begin{bmatrix}1 & 0 & 0\\ 0 & 1 & 0\\ 0 & 0 & 1\end{bmatrix} - \boldsymbol{u}\boldsymbol{u}^T\right) + \sin\phi\begin{bmatrix}0 & -u_z & u_y\\ u_z & 0 & -u_x\\ -u_y & u_x & 0\end{bmatrix} \quad (2\text{-}7)$$

where $\boldsymbol{u} = \boldsymbol{R}_{PA}{}^T[1 \quad 0 \quad 0]^T$

U, *V*: Dimension of the image in pixels

SID: Distance between X-ray source and image intensifier

SOD: Distance between X-ray source and object

IS: Intensifier size

θ: Primary angle (LAO/RAO, positive in LAO)

ϕ: Secondary angle (Cranial/Caudal, positive in Cranial)

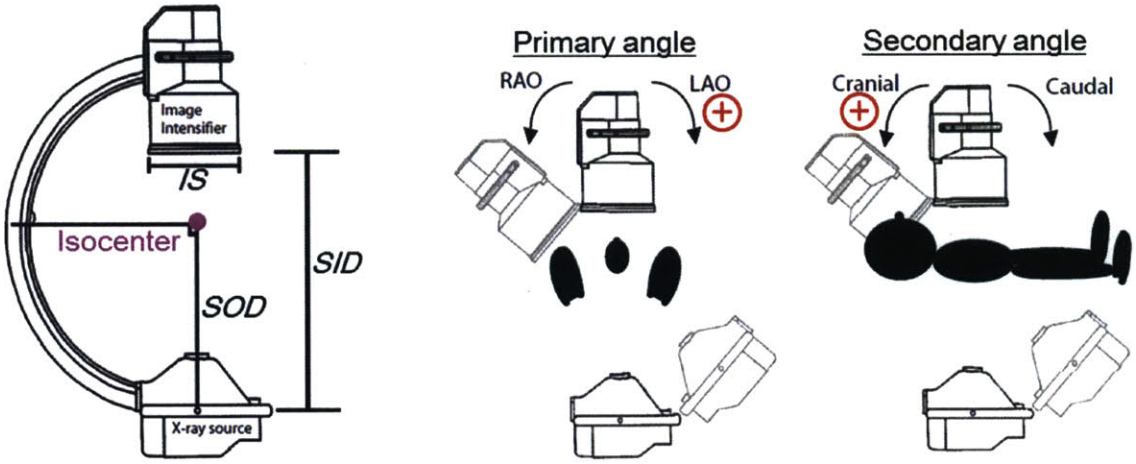

Figure 2-4 Configuration of angiographic system [12]

Isocenter is defined as the rotation center of the C-arm imaging system. IS, SID, and SOD stand for intensifier size, source (X-ray source) to intensifier distance, and source to objective (patient) distance, respectively. Geometric orientation of the C-arm imaging system is defined by the primary angle and the secondary angle. The primary angle represents the rotation around the axial direction (proximal to distal direction), while the secondary angle represents the rotation around the horizontal direction (perpendicular to the axial direction).

The reconstructed 3D points were smoothed using the cubic smoothing spline function (MATLAB csaps function) [34]. This function was selected because the smoothing parameter p, which can determine the closeness of the spline function to the actual data, can be set. The smoothing parameter p can determine the closeness of the spline function to the actual data. MATLAB suggests using the value that is calculated from:

$$p = \left(1 + \frac{h^3}{0.6}\right)^{-1} \tag{2-8}$$

where h is the average spacing of data. Since our average spacing was h = 0.9-1.2 pixel/point, the suggested smoothing parameter p was calculated to be p = 0.25-0.45. The parameter was explored within this range and experimentally determined to minimize the error between the skeletonized 2D points that were used for reconstruction and the 3D-to-2D back-projected points from the reconstructed centerline. The smoothing parameter was set as p = 0.3. Finally, the smoothed centerlines were transferred rigidly so that the bifurcation, i.e., the intersection of the main segment and the sub-segment, is coincident to the origin (0, 0, 0).

2.3.5 Implementation of Algorithm for Non-isocentric Paired Images

To make the developed vessel centerline reconstruction method applicable to non-isocentric pairs of images, the following algorithm was implemented. This algorithm was developed by modifying Yang et al.'s method [6]. First, a vessel centerline was reconstructed by assuming that there was no isocenter movement. To achieve this assumption, the second image was moved in the vertical direction to make the vertical location of the bifurcation in two images equal before applying the vessel centerline reconstruction method. Then, this initial 3D centerline geometry was back-projected to the 2D space by considering the total movements of the isocenter in each image, $\boldsymbol{m}_1$ and $\boldsymbol{m}_2$ (Equation 2-9 and 2-10, Figure 2-5). Next, $\boldsymbol{m}_1$ and $\boldsymbol{m}_2$ were found by minimizing the optimization function that is described by the sum of point transfer error (distance between the original 2D points extracted from angiographic images and the

corresponding 3D-to-2D back-projected points) and directional vector transfer error (distance between the original 2D direction vectors and the projected 3D directional vectors) (Equation 2-11).

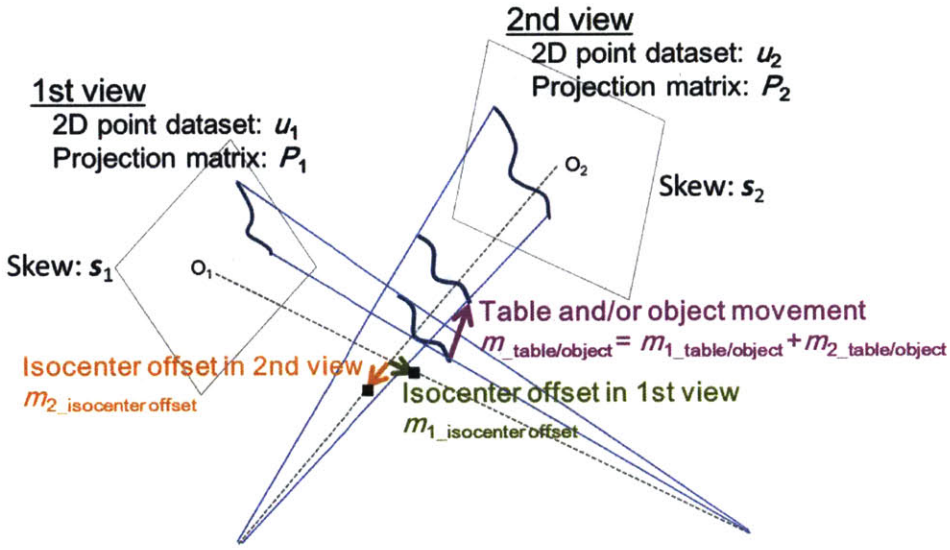

Figure 2-5 Potential causes of the isocenter movement

(a) Machine-origin isocenter offset: The angiography system itself has isocenter offset when it is rotated. This appears in each image as the difference between the center of view and the projected origin.

(b) Movement of the object center: During the procedure, the center of the object may move because physicians may move the table and/or patients themselves may move.

Objective function

$$\begin{cases} \boldsymbol{u}_{1,i} = \boldsymbol{P}_1 (\boldsymbol{X}_i + \boldsymbol{m}_1) & (2\text{-}9) \\ \boldsymbol{u}_{2,i} = \boldsymbol{P}_2 (\boldsymbol{X}_i + \boldsymbol{m}_2) & (2\text{-}10) \end{cases}$$

where (k=1, 2)

$$\boldsymbol{m}_k = \boldsymbol{m}_{k\_isocenter\_offset} + \boldsymbol{m}_{k\_table/object}$$

$$\boldsymbol{P}_k = \begin{bmatrix} -SID_k \cdot U/IS_k & s_k & U/2 \\ 0 & SID_k \cdot V/IS_k & V/2 \\ 0 & 0 & 1 \end{bmatrix} \begin{bmatrix} \ddots & & 0 \\ & \boldsymbol{R}_{PA,k} \cdot \boldsymbol{R}_{SA,k} & 0 \\ & & \ddots \quad -SOD_k \end{bmatrix}$$

Optimization function

$$f(\boldsymbol{m}_1, \boldsymbol{s}_1, \boldsymbol{m}_2, \boldsymbol{s}_2) = \sum_{i=1}^{n}\left[d\left(\boldsymbol{u}_{1,i} - \boldsymbol{P}_1(\boldsymbol{X}_i + \boldsymbol{m}_1)\right)^2 + d\left(\boldsymbol{u}_{2,i} - \boldsymbol{P}_2(\boldsymbol{X}_i + \boldsymbol{m}_2)\right)^2\right] + w\sum_{j=2}^{n}\left[\left\|\frac{\boldsymbol{u}_{1,j} - \boldsymbol{u}_{1,j-1}}{\|\boldsymbol{u}_{1,j} - \boldsymbol{u}_{1,j-1}\|} - \frac{\boldsymbol{P}_1(\boldsymbol{X}_j + \boldsymbol{m}_1) - \boldsymbol{P}_1(\boldsymbol{X}_{j-1} + \boldsymbol{m}_1)}{\|\boldsymbol{P}_1(\boldsymbol{X}_j + \boldsymbol{m}_1) - \boldsymbol{P}_1(\boldsymbol{X}_{j-1} + \boldsymbol{m}_1)\|}\right\|^2 + \left\|\frac{\boldsymbol{u}_{2,j} - \boldsymbol{u}_{2,j-1}}{\|\boldsymbol{u}_{2,j} - \boldsymbol{u}_{2,j-1}\|} - \frac{\boldsymbol{P}_2(\boldsymbol{X}_j + \boldsymbol{m}_2) - \boldsymbol{P}_2(\boldsymbol{X}_{j-1} + \boldsymbol{m}_2)}{\|\boldsymbol{P}_2(\boldsymbol{X}_j + \boldsymbol{m}_2) - \boldsymbol{P}_2(\boldsymbol{X}_{j-1} + \boldsymbol{m}_2)\|}\right\|^2\right] \quad (2\text{-}11)$$

Finally, using this optimal $\boldsymbol{m}_1$ and $\boldsymbol{m}_2$, the 3D centerline geometry was updated. The updated centerline was smoothed and transferred rigidly as explained in 2.3.4.

2.3.6 Method Validation

2.3.6.1 Comparison between Actual Geometry and Reconstructed Geometry

To validate the vessel centerline reconstruction method before implementing a new algorithm for a non-isocentric pair of images, the centerlines of the phantom models were first reconstructed from paired isocentric angiographic images, i.e., the images obtained without any table movements. The reconstructed geometries of both the non-stented and the stented phantom models from various imaging angle differences (20^0-130^0), i.e., the angle between paired images, were compared to the actual geometry in terms of lengths and bifurcation angle.

To validate the vessel centerline reconstruction method after implementing a new algorithm, the centerlines were reconstructed from paired non-isocentric angiographic images and were compared to the actual geometry in terms of lengths and bifurcation angle. In addition, to understand the influence of the implemented algorithm on the accuracy of the vessel centerline reconstruction, the errors of lengths and bifurcation angle after implementation were compared to those before implementation. All values were represented as mean ± standard deviation.

2.3.6.2 Comparison between Actual Movement and Estimated Movement

The total movement of the isocenter due to the machine-origin isocenter offset and the table movement can be estimated by applying the algorithm for a non-isocentric pair of images. This estimated movement was compared to the actual movement of the table that was recorded in the DICOM headers. All values were represented as mean ± standard deviation.

2.4 Results and Discussions

2.4.1 Validation of Vessel Centerline Reconstruction Method before Implementing New Algorithm for Non-isocentric Paired Images

The newly developed vessel centerline reconstruction method yielded quite similar centerline geometries to the actual geometry for all imaging angle differences (20^0-130^0) in both the non-stented and the stented phantom models (Figure 2-6). The static errors of the length and the bifurcation angle were 1.9 mm ± 1.4 mm and 2.6^0 ± 1.7^0 for the non-stented model, and 1.8 mm ± 1.5 mm and 1.5^0 ± 0.9^0 for the stented model, respectively (N=32) (Table 2-3). These errors were independent of the imaging angle differences.

2.4.2 Validation of Newly Implemented Algorithm for Non-isocentric Paired Angiographic Images

The new algorithm for non-isocentric paired angiographic images was validated by (i) comparing the estimated movement to the actual movement (2.4.2.1), (ii) comparing the reconstructed geometry to the actual geometry (2.4.2.2), and (iii) comparing the reconstructed geometries before and after implementing the algorithm (2.4.2.3).

2.4.2.1 Comparison between Actual Movement and Estimated Movement

This new algorithm enables the estimation of the total movement of the isocenter in each image, i.e., the sum of the machine-origin isocenter offset and the table and/or object movement. If the machine-origin isocenter offset can be assumed to be small, the estimated movement should be close to the actual movement of the table since the phantom models are static. Table 2-2 summarizes the differences between the actual movement and the estimated movement (N=32 for each phantom model). Since the information of the isocenter offset is not available,

these differences cannot be compared directly to the machine-origin isocenter offset; however, these differences represented less than 1% of the distance between X-ray source and the intensifier: 0.19% ± 0.10% for the non-stented model and 0.33% ± 0.09% for the stented model. In addition, these differences were 1-7% compared to the sizes of the phantom models (100 mm × 50 mm). Although this algorithm cannot be compared to the state-of-the-art methods as no methods can estimate the isocenter movement, these results strongly suggest that this new algorithm has an ability to estimate the total isocenter movement in each image correctly, which will allow calibrating and reconstructing a vessel centerline accurately.

Table 2-2 Comparison between the actual movement and the estimated movement (N=32)

	Actual movement [mm]	Estimated movement [mm]	Difference [mm]	Error [%]
Non-stented model	25.5	23.5±1.2	2.0±1.1	8.0±4.3
Stented model	35.2	31.6±1.0	3.6±1.0	10.4±2.8

2.4.2.2 Comparison between Reconstructed Geometry and Actual Geometry

After calibrating the isocenter movements in each image, the final geometries of the vessel centerlines from various imaging angle differences were reconstructed again. All the reconstructed geometries were quite similar to the actual geometry (Figure 2-6). The static errors of the length and the bifurcation angle were 1.7 mm ± 1.4 mm and $2.6^0 \pm 2.0^0$ for the non-stented model, and 1.8 mm ± 1.6 mm and $0.9^0 \pm 0.9^0$ for the stented model, respectively (N=32) (Table 2-3). These errors were independent of the imaging angle difference. These results demonstrate that this newly developed method has a high reproducibility across various imaging angle differences (20^0-130^0).

2.4.2.3 Comparison of Reconstructed Geometries between Before and After Implementing Algorithm

To evaluate the influence of the newly implemented algorithm on the vessel centerline reconstruction, the static errors of the length and bifurcation angle were compared between before and after the implementation. As summarized in Table 2-3, these values were quite similar to each other. This result suggests that the implementation of the algorithm does not affect the vessel centerline reconstruction.

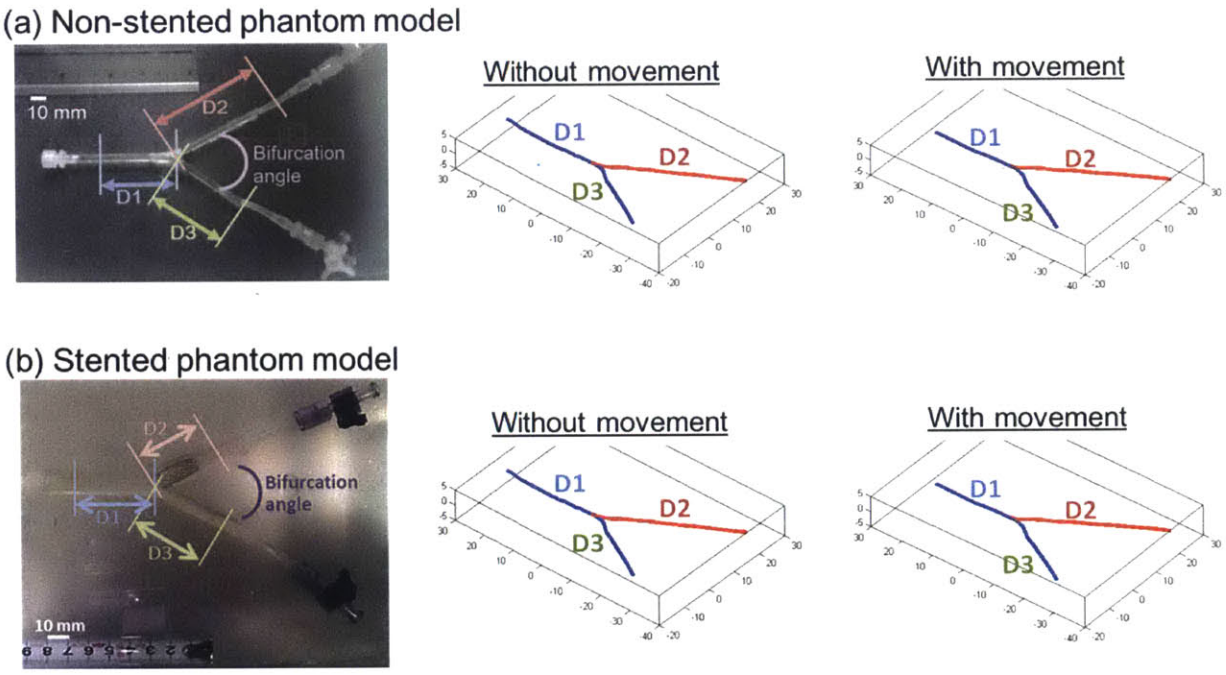

Figure 2-6 Phantom models and reconstructed centerline geometries

Using the pair of angiographic images of the non-stented and stented phantom models, the centerlines were reconstructed. All the centerlines reconstructed from various imaging angle differences (20^0-130^0) were similar in lengths and bifurcation angle to the actual geometry.

Table 2-3 Static errors of length and bifurcation angle

(a) non-stented phantom model (N=32) and (b) stented phantom model (N=32)

(a) Non-stented		Without movement		With movement	
Length	D1	1.9 mm ± 1.4 mm 4.8 pixel ± 3.5 pixel	7.4% ± 5.5%	1.3 mm ± 1.1 mm 3.3 pixel ± 2.9 pixel	5.2% ± 4.5%
	D2	1.5 mm ± 1.2 mm 3.9 pixel ± 3.1 pixel	3.6% ± 2.8%	1.7 mm ± 1.1 mm 4.2 pixel ± 2.9 pixel	3.9% ± 2.7%
	D3	2.4 mm ± 1.6 mm 6.1 pixel ± 4.0 pixel	7.0% ± 4.6%	2.1 mm ± 1.7 mm 5.5 pixel ± 4.3 pixel	6.3% ± 5.0%
	Total	1.9 mm ± 1.4 mm 4.9 pixel ± 3.6 pixel	6.0% ± 4.7%	1.7 mm ± 1.4 mm 4.4 pixel ± 3.5 pixel	5.0% ± 4.2%
Bifurcation angle		2.6° ± 1.7°	4.2% ± 2.7%	2.6° ± 2.0°	4.2% ± 3.2%

(b) Stented		Without movement		With movement	
Length	D1	1.5 mm ± 0.9 mm 3.4 pixel ± 2.6 pixel	3.7% ± 2.3%	1.4 mm ± 1.3 mm 3.5 pixel ± 3.4 pixel	3.5% ± 3.4%
	D2	2.1 mm ± 1.8 mm 4.9 pixel ± 3.8 pixel	5.3% ± 4.5%	2.2 mm ± 1.8 mm 5.7 pixel ± 4.5 pixel	5.6% ± 4.4%
	D3	1.8 mm ± 1.5 mm 5.8 pixel ± 4.5 pixel	4.6% ± 3.7%	1.7 mm ± 1.6 mm 4.3 pixel ± 4.1 pixel	4.1% ± 4.0%
	Total	1.8 mm ± 1.5 mm 4.7 pixel ± 3.8 pixel	4.5% ± 3.6%	1.8 mm ± 1.6 mm 4.4 pixel ± 4.3 pixel	4.4% ± 4.0%
Bifurcation angle		1.5° ± 0.9°	2.9% ± 1.7%	0.9° ± 0.9°	1.8% ± 1.7%

2.4.3 Effectiveness of Algorithm for Non-isocentric Paired Angiographic Images

2.4.3.1 3D-to-2D Back-projected Distance Error

To evaluate the effectiveness of the algorithm for non-isocentric pairs of images, the 3D-to-2D back-projected distance error after applying the algorithm was compared to that before applying the algorithm. The reconstructed 3D centerlines were back-projected onto 2D angiographic images and the distance between the 2D centerlines that were originally extracted from angiographic images and the 3D-to-2D back-projected points were measured. Then, the 3D-to-2D back-projected distance error was evaluated by calculating root mean square (RMS) error with Equation 2-12.

$$RMS\ error = \sqrt{\frac{\sum_{i=1}^{n}(distance)^2}{n}} \quad (2\text{-}12)$$

As summarized in Table 2-4, the RMS error has been improved by approximately 35-fold by applying this algorithm. In addition, the RMS error after applying this algorithm was similar to that of Yang et al.'s method (1.30 pixels) [6].

Table 2-4 Comparison of 3D-to-2D back-projected distance error

	Before applying	After applying
Non-stented model	18.1 mm, 46.2 pixel	0.458 mm, 1.17 pixel
Stented model	25.4 mm, 65.0 pixel	0.768 mm, 1.97 pixel

2.4.3.2 Importance of Directional Vector Transfer Error in Optimization Function

Optimization function (Equation 2-11) contains both point transfer error and directional vector transfer error. As described in Figure 2-7, although the point transfer error is minimal, the geometry may not be parallel to the actual geometry. To avoid this problem, the directional vector transfer error needs to be considered. To evaluate the importance of this component, the static errors in length and bifurcation angles were compared between cases of optimizing with and without this component. The bigger static errors were observed in 62.5% of cases for the non-stented phantom model and 48.5% of cases for the stented phantom model when the directional vector transfer error was not used. This result suggests that the existence of the directional vector transfer error enable reconstructing more precise vessel centerline from the non-isocentric paired images.

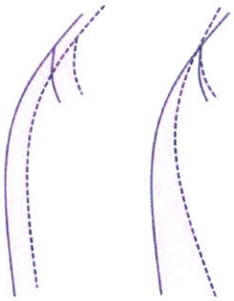

Figure 2-7 Extracted 2D centerline (solid line) and 3D-to-2D back-projected centerline (dotted line)
Although the point transfer error (area colored in pink) is the same, a more accurate centerline is reconstructed when these two geometries are parallel to each other (left) than when they are not parallel (right).

2.4.4 Advantages of Newly Developed Vessel Centerline Reconstruction Method

This newly developed vessel centerline reconstruction method is able to handle non-isocentric images, while most of the state-of-the-art methods except Yang et al.'s method are not. The only and important advantage of the newly developed method compared to Yang et al.'s method is that the total isocenter movement in each image can be estimated by this method with high accuracy as discussed in 2.4.2.1. Under the situation that the machine-origin isocenter offset is negligible, which is applicable to most cases, the estimated isocenter movement can be equal to the movement of the table and/or the patient during the procedure. Therefore, the information of the isocenter movement can be collected retrospectively. This is a key feature of this method because it allows convenient operations of the C-arm coronary angiography system in the catheterization lab as per normal and because it does not require any special considerations or preparation during the acquisition of the angiographic images.

This method is also superior to the currently available methods since it can handle non-orthogonal paired angiographic images. This method can reconstruct the vessel centerline from a pair of images with at least 20^0 of imaging angle difference, while the best state-of-the-art method requires at least 25^0 of imaging angle difference [4]. In addition, the static errors in both lengths and bifurcation angle were independent of the imaging angle differences (20^0-130^0), which suggests that this method is robust to the geometric orientation of the imaging system.

Finally, this method is comparable to the commercially available system. As shown in Figure 2-8, a strong 1:1 linear relationship between the actual length and the reconstructed length was observed for the non-stented phantom model: slope = 1.02, correlation coefficient R^2 = 0.89 for all non-isocentric/isocentric and non-orthogonal/orthogonal data (N=64). This is similar to the performance of the commercially available real-time 3D quantitative coronary angiography system, CardiOp-B System (Siemens Medical Systems, Germany) [35].

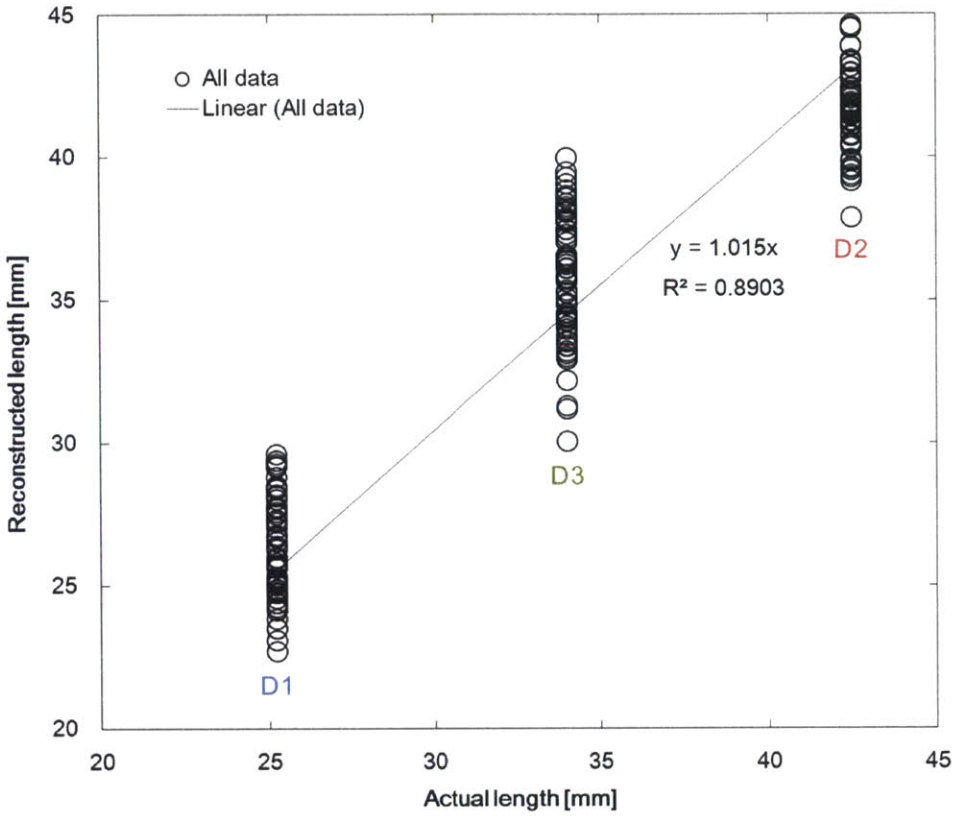

Figure 2-8 Relationship between the actual length and the reconstructed length

The comparison between the actual and the reconstructed lengths demonstrated a strong linear relationship for the non-stented phantom model.

References

1. Bourantas, C.V., et al., *A new methodology for accurate 3-dimensional coronary artery reconstruction using routine intravascular ultrasound and angiographic data: implications for widespread assessment of endothelial shear stress in humans.* EuroIntervention, 2013. **9**(5): p. 582-593.
2. Tu, S.X., et al., *In vivo comparison of arterial lumen dimensions assessed by co-registered three-dimensional (3D) quantitative coronary angiography, intravascular ultrasound and optical coherence tomography.* International Journal of Cardiovascular Imaging, 2012. **28**(6): p. 1315-1327.
3. Athanasiou, L.S., et al. *3D Reconstruction of Coronary Arteries using Frequency Domain Optical Coherence Tomography Images and Biplane Angiography.* in *34th Annual International Conference of the IEEE Engineering-in-Medicine-and-Biology-Society (EMBS)*. 2012. San Diego, CA.
4. Tu, S., et al., *Fusion of 3D QCA and IVUS/OCT.* Int J Cardiovasc Imaging, 2011. **27**(2): p. 197-207.
5. van der Giessen, A.G., et al., *3D fusion of intravascular ultrasound and coronary computed tomography for in-vivo wall shear stress analysis: a feasibility study.* International Journal of Cardiovascular Imaging, 2010. **26**(7): p. 781-796.
6. Yang, J., et al., *Novel approach for 3-d reconstruction of coronary arteries from two uncalibrated angiographic images.* IEEE Trans Image Process, 2009. **18**(7): p. 1563-72.
7. Slager, C.J., et al., *True 3-Dimensional Reconstruction of Coronary Arteries in Patients by Fusion of Angiography and IVUS (ANGUS) and Its Quantitative Validation.* Circulation, 2000. **102**(5): p. 511-516.
8. Bourantas, C.V., et al., *ANGIOCARE: An automated system for fast three-dimensional coronary reconstruction by integrating angiographic and intracoronary ultrasound data.* Catheterization and Cardiovascular Interventions, 2008. **72**(2): p. 166-175.
9. Bourantas, C.V., et al., *A method for 3D reconstruction of coronary arteries using biplane angiography and intravascular ultrasound images.* Computerized Medical Imaging and Graphics, 2005. **29**(8): p. 597-606.
10. Wahle, A., et al., *Fusion of angiography and intravascular ultrasound in vivo: establishing the absolute 3-D frame orientation.* Biomedical Engineering, IEEE Transactions on, 1999. **46**(10): p. 1176-1180.
11. Wahle, A., et al., *Geometrically correct 3-D reconstruction of intravascular ultrasound images by fusion with biplane angiography-methods and validation.* IEEE Transactions on Medical Imaging, 1999. **18**(8): p. 686-699.

12. Shekhar, R., et al. *Fusion of intravascular ultrasound and biplane angiography for three-dimensional reconstruction of coronary arteries.* in *Computers in Cardiology, 1996.* 1996.
13. Laban, M., et al. *ANGUS: a new approach to three-dimensional reconstruction of coronary vessels by combined use of angiography and intravascular ultrasound.* in *Computers in Cardiology 1995.* 1995.
14. Jang, I.-K., *Optical Coherence Tomography or Intravascular Ultrasound?* JACC: Cardiovascular Interventions, 2011. **4**(5): p. 492-494.
15. Nair, A., et al., *Coronary plaque classification with intravascular ultrasound radiofrequency data analysis.* Circulation, 2002. **106**(17): p. 2200-6.
16. Yock, P.G., et al., *Intravascular ultrasound guidance for catheter-based coronary interventions.* Journal of the American College of Cardiology, 1991. **17**(6s2): p. 39-45.
17. Nissen, S.E., et al., *Intravascular ultrasound assessment of lumen size and wall morphology in normal subjects and patients with coronary artery disease.* Circulation, 1991. **84**(3): p. 1087-99.
18. Templin, C., et al., *Coronary optical frequency domain imaging (OFDI) for in vivo evaluation of stent healing: comparison with light and electron microscopy.* Eur Heart J, 2010. **31**(14): p. 1792-801.
19. Murata, A., et al., *Accuracy of optical coherence tomography in the evaluation of neointimal coverage after stent implantation.* JACC Cardiovasc Imaging, 2010. **3**(1): p. 76-84.
20. Gonzalo, N., et al., *Reproducibility of quantitative optical coherence tomography for stent analysis.* Eurointervention, 2009. **5**(2): p. 224-32.
21. Bezerra, H.G., et al., *Intracoronary optical coherence tomography: a comprehensive review clinical and research applications.* JACC Cardiovasc Interv, 2009. **2**(11): p. 1035-46.
22. Suzuki, Y., et al., *In vivo comparison between optical coherence tomography and intravascular ultrasound for detecting small degrees of in-stent neointima after stent implantation.* JACC Cardiovasc Interv, 2008. **1**(2): p. 168-73.
23. Khaleel, H.H., et al., *A Review paper of 3D Surface Reconstruction of Coronary Arteries From Cardiovascular Angiography.* 2012 International Conference on Advanced Computer Science Applications and Technologies (Acsat), 2012: p. 419-435.
24. Sarwal, A. and A.P. Dhawan, *Three dimensional reconstruction of coronary arteries from two views.* Computer Methods and Programs in Biomedicine, 2001. **65**(1): p. 25-43.
25. Ellwein, L.M., et al., *Optical Coherence Tomography for Patient-specific 3D Artery Reconstruction and Evaluation of Wall Shear Stress in a Left Circumflex Coronary Artery.* Cardiovascular Engineering and Technology, 2011. **2**(3): p. 212-227.
26. Subramanian, K.R., et al., *Accurate 3D reconstruction of complex blood vessel geometries*

from intravascular ultrasound images: in vitro study. Journal of Medical Engineering & Technology, 2000. **24**(4): p. 131-140.

27. Zhang, W., Z. Chen, and X. Zhang, *3D Vessel Tree Reconstruction from Rotational C-arm Projections by Multi-view Stereo Reconstruction*, in *Apcmbe 2008: 7th Asian-Pacific Conference on Medical and Biological Engineering*, Y. Peng and X. Weng, Editors. 2008. p. 434-441.
28. Hoffmann, K.R., et al., *Biplane X-ray angiograms, intravascular ultrasound, and 3D visualization of coronary vessels.* Int J Card Imaging, 1999. **15**(6): p. 495-512.
29. Bourantas, C.V., et al., *Bioresorbable vascular scaffold treatment induces the formation of neointimal cap that seals the underlying plaque without compromising the luminal dimensions: a concept based on serial optical coherence tomography data.* EuroIntervention, 2014.
30. Papafaklis, M.I., et al., *Anatomically correct three-dimensional coronary artery reconstruction using frequency domain optical coherence tomographic and angiographic data: head-to-head comparison with intravascular ultrasound for endothelial shear stress assessment in humans.* . EuroIntervention, 2014(1969-6213 (Electronic)).
31. Shechter, G., et al., *Prospective motion correction of X-ray images for coronary interventions.* Medical Imaging, IEEE Transactions on, 2005. **24**(4): p. 441-450.
32. Faugeras, O., Q.-T. Luong, and T.o. Papadopoulo, *The geometry of multiple images : the laws that govern the formation of multiple images of a scene and some of their applications.* 2001, Cambridge, Mass.: MIT Press. xxiv, 644 p.
33. Martorell, J., et al., *Engineered arterial models to correlate blood flow to tissue biological response.* Annals of the New York Academy of Sciences, 2012. **1254**: p. 51-56.
34. Moses, D.A. and L. Axel, *Quantification of the curvature and shape of the interventricular septum.* Magnetic Resonance in Medicine, 2004. **52**(1): p. 154-163.
35. Gradaus, R., et al., *Clinical assessment of a new real time 3D quantitative coronary angiography system: evaluation in stented vessel segments.* Catheter Cardiovasc Interv, 2006. **68**(1): p. 44-9.

CHAPTER 3:

VALIDATION OF VESSEL CENTERLINE RECONSTRUCTION & DEVELOPMENT OF STRUCTURAL RECONSTRUCTION AND TIME-POINT REGISTRATION IN A PRECLINICAL SETTING

3.1 Abstract

Appreciation of vascular responses, optimization of catheter intervention, especially stent implantation, and prediction of clinical outcomes can only be achieved when the physiologically realistic endovascular environment is reconstructed in 3D space and when the vascular responses are tracked over time in 3D space on the stent-strut level. The vessel centerline can serve as a fusion path for structural reconstruction of lumen and stent by fusion of angiography and optical coherence tomography and as a registration path for registering the 3D structures across time. However, the morphology of the vessel centerline may change due to the cardiac motion and/or the vascular responses to intervention, which prevent the accurate reconstruction of the 3D structures and the precise registration across time. Cardiac motion may affect the structural reconstruction because it may induce lateral and longitudinal movements of the imaging catheter with which the intravascular images are acquired. Therefore, to develop a structural reconstruction method and a time-point registration method, first the vessel centerline reconstruction method needs to be validated under the conditions where the cardiac motion and the vascular responses to the intervention are to be considered. Then, the effect of the cardiac motion on the fusion of angiography and optical coherence tomography needs to be evaluated to understand its influence on the structural reconstruction. Finally, both the structural reconstruction method and the time-point registration method must be improved to be made robust in the presence of cardiac motion and/or the vascular responses.

3.2 Background

Since blood vessels move, grow, and respond to catheter intervention, the influences of the cardiac motion and the vascular morphological change over time on the vessel centerline reconstruction need to be considered to understand their influence on structural reconstruction by fusion of angiography and optical coherence tomography (OCT) and time-point registration. Cardiac motion directly affects the morphology of the coronary artery, which may change the morphology of the vessel centerline. Since the OCT images of the stented region are acquired over approximately a single cardiac cycle due to the fast pullback speed of OCT [1, 2], the morphological change of the vessel centerline over a cardiac cycle may result in the error in structural reconstruction by angiography-OCT fusion when the vessel centerline is used as a fusion path. Therefore, the vessel centerline reconstruction method needs to be validated under the condition where the influences of the cardiac motion are to be considered. The preclinical setting is suitable for validating the vessel centerline reconstruction developed in Chapter 2 because it provides not only real physiologic environment, i.e., effects of the cardiac motion, but also quantifiable metrics of the imaging environment, i.e., controlled isocenter movement.

This preclinical setting is also appropriate to develop a structural reconstruction method by angiography-OCT fusion and to improve it to make it robust to cardiac motion. The imaging catheter could move laterally and longitudinally due to the cardiac motion [3]. The previous study demonstrated using the four patients' data that the usage of the vessel centerline as a fusion path could overcome the lateral movement problem and induced a small error in angiography-OCT fusion due to the longitudinal movement of the catheter using the sample of four patients [3]. However, the accuracy of the structural reconstruction by angiography-OCT fusion has not been evaluated; and thus, the method has not been optimized yet in the presence of cardiac motion. Since all the procedures can proceed in the same manner as that in a clinical setting, while the procedures can be controlled and their precise information can be obtained, the

precision of the structural reconstruction method can be evaluated and the method itself can be improved so as to be robust to cardiac motion if it is developed in the preclinical setting.

Furthermore, the preclinical setting can provide quantifiable metrics of the evolution of vessel dimensions, i.e., vascular responses to controlled procedural scenarios. This time-course data that provides quantifiable information on vascular responses is ideal for developing a time-point registration method. To optimize the procedure of stent implantation and to predict the chronic outcomes before the procedure, the underlying mechanism of the vascular responses needs to be understood in 3D. Time-point registration is important because this understanding can be achieved only when the 3D structures of the same vessel at different time-points are registered precisely in 3D. Since the imaging catheter cannot be located at the exact same location over time, the imaging catheter cannot be a path for registering the structures of the same vessel across time. The state-of-the-art method uses side branches as the landmarks to compare the 2D images at different time-points [4]; however, this method is limited by the number of the available side branches. Neither can it track vascular responses in 3D, which prevents the full understanding of the vascular responses in a more physiologically and pathologically meaningful way. Stone et al. proposed a method that can compare the 3D structures in consecutive 3-mm segments between different time-points [5]. However, the influence of the stent-strut on the local vascular responses cannot be evaluated with this method because the resolution of this method (3 mm) is much larger than the stent-strut size (approximately 100 μm). On the other hand, the vessel centerline can serve as the set of landmarks that are necessary to register the structures over time. The advantage of using the vessel centerline as a registration path is that as many landmarks can be created as needed, which enable utilizing all the imaging data and comparing the 3D structures on the stent-strut level. However, the vascular responses may change the morphology of the vessel centerline over time, which may prevent accurate registration across time. To develop a time-point registration method, the points on the vessel centerline that are least or not affected by the

vascular responses need to be found by evaluating the morphological change of the vessel centerline due to the vascular responses to stent implantation.

In this chapter, the vessel centerline reconstruction method developed in Chapter 2 is first validated under the situation where the cardiac motion is to be affected (Table 3-1). Then, a structural reconstruction method is developed using angiography-OCT fusion. The effect of the cardiac motion on the morphology of the vessel centerline is evaluated and this structural reconstruction method is improved to make it robust in the presence of cardiac motion. Finally, the morphological change of the vessel centerline over time due to the vascular responses is evaluated and a new computational framework for time-point registration is created using, as the landmarks, the points on the vessel centerline that are insensitive to the vascular responses.

Table 3-1 Comparison between the state-of-the-art methods and the proposed method for vessel centerline reconstruction

	Bourantas et al. [6]	Yang et al. [9]	Proposed method
Purpose for...	Angiography + IVUS, Native artery	Angiography (2D →3D), Native artery	Angiography + OCT, Stented artery
1. Isocenter offset	×	✓	✓
2. Movement of object center	×	✓	✓
3. Imaging angle difference	×	×	✓
4. Effect of cardiac motion	×	×	✓
5. Availability of ECG-gating function	×	×	✓

*Red box indicates the challenges that are addressed in this chapter.

3.3 Materials and Methods

3.3.1 *In Vivo* Animal Models

Twelve coronary arteries (five right coronary arteries, four left anterior descending arteries, and three left circumflex arteries) from five Yorkshire swine (40-50 kg) were used. After anesthetizing the swine and accessing the coronary artery, heparin (50-200 U/kg) was administered so as to maintain an activated clotting time greater than 275 s. Coronary arteries were selectively cannulated with a 7F guide catheter (JL 3.5 VISTA BRITE TIP® Guiding Catheter, Cordis Corpolation, Dublin, OH) under fluoroscopic guidance. Several angiographic images were obtained and the arterial diameters were measured by quantitative coronary angiography analysis (2.84 mm ± 0.17 mm). Standard bare metal stents (3.0 mm × 17 mm) were implanted in the targeted arteries with standard procedures. The inflation pressure of the balloon catheter was selected as balloon : artery ratios of 1-1.1 to ensure minimal injury and to be in line with the current clinical guideline. Controlled stent underexpansion was created in the midportion of six vessels out of twelve vessels (two right coronary arteries, three left anterior descending arteries, and one left circumflex artery) with a specially-modified balloon catheter (Figure 3-1). The center of the balloon catheter was restricted from full inflation by placing a polyethylene terephthalate (PET) tube (2.8 mm × 5 mm or 2.5 mm × 5 mm) over the balloon catheter to effectuate an hourglass expansion (Figure 3-1). Since the diameter of PET tube is smaller than that of the balloon catheter (approximately 3.0 mm), the stent at this region cannot be fully apposed to the vessel wall (Figure 3-2). After implanting the stent in each vessel, the images at post-implantation were acquired with coronary angiography and optical coherence tomography (OCT) as described in 3.3.2. Those images were also acquired at 5-day and 28-day follow-ups. All animals survived for 28 days, and then were euthanized.

All animal studies were performed at GLP AAALAC accredited animal facility (CBSET, Inc, Lexington, MA) according to the US Department of Agriculture Animal Welfare Act and with the

guidelines described in the Guide for Care and Use of Laboratory Animals.

Figure 3-1 Specially-modified balloon catheter
To create underexpansion of the stent, the balloon catheter is restricted from its full expansion by placing a PET tube, whose diameter is smaller than that of the balloon catheter, over the balloon catheter in the middle region.

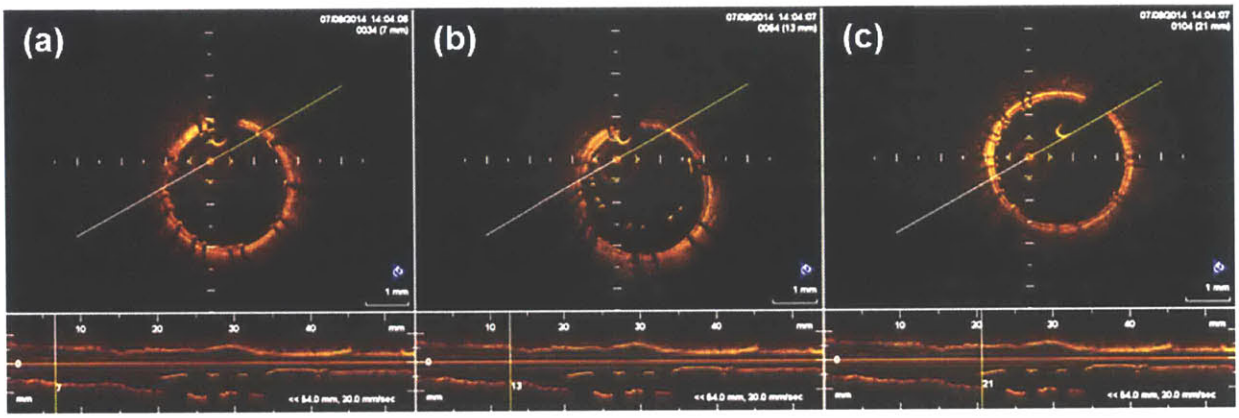

Figure 3-2 Underexpansion of the stent with the specially-modified balloon catheter
Using the specially-modified balloon catheter (Figure 3-1), the middle region of the stent is underexpanded and is not fully apposed to the vessel wall **(b)**. The stent is fully apposed to the vessel wall in the proximal **(a)** and in the distal regions **(c)**.

3.3.2 Image Acquisition

At all time-points (post-implantation, 5-day follow-up, and 28-day follow-up), the angiographic images and OCT images were acquired. After confirming that the isocenters were coincident with respect to any position of the monoplane angiographic system, the angiographic images of each stented artery were acquired from two different views at a rate of 30 frames/s with radio-opaque contrast dye injection through the guide catheter. The radio-opaque contrast dye was diluted the same as that for clinical usage (contrast dye : saline = 1:1). All angiographic images were taken with Innova 2100 (GE Healthcare, Cleveland, OH) and stored in the DICOM

format with all the imaging parameters,including the position of the angiography system and the magnification of the images. The resolution was 0.35 mm/pixel ± 0.04 mm/pixel. The OCT images were acquired with C7-XR OCT Intravascular Imaging System (St. Jude Medical, St. Paul, MN). The OCT catheter (C7 Dragonfly, St. Jude Medical, St. Paul, MN) was advanced approximately 5 mm distal to the edge of the stent. The images of 50-60 mm length/run were taken with 20 mm/s pullback speed during power contrast dye flushing (4-6 mL/s for 3 s). The images were acquired every 200 μm in the longitudinal direction (the preset OCT inter-frame distance). The procedure was repeated when motion artifacts and/or inadequate flushing were observed. After dimensional (z-offset) calibration, i.e., calibrating the imaging catheter size, the OCT images were stored in the DICOM and the AVI formats.

To validate the vessel centerline reconstruction method, additional angiographic images were acquired with specific conditions at post-implantation: (i) with ECG-gating function, (ii) from various positions of the angiographic system to create the range of the angle between paired images (imaging angle difference) from 50^0 to 130^0 and without moving the table to create the isocentric and non-orthogonal paired images, and (iii) from various positions of the angiographic system to create the range of the imaging angle difference from 20^0 to 130^0 and with moving the table to create the non-isocentric and non-orthogonal paired images. The movement of the table was also recorded in the DICOM format.

3.3.3 Image Processing Software

All the image processes except the processes for the OCT inter-frame distance estimation (3.3.6.3.1) were performed with MATLAB (MathWorks, Natick, MA). As described in 2.3.3, MATLAB is suitable because it has its own validated and easy-to-use functions for image processing and statistical analysis, and ability to create algorithms for specialized commands based on our needs. ImageJ was used to analyze the OCT inter-frame distance estimation.

ImageJ is a user-friendly image processing software; and thus, it is more appropriate for OCT image analysis where user inputs are more frequently required.

3.3.4 Vessel Centerline Reconstruction Method

The vessel centerline reconstruction method has six steps (Figure 3-3):

Step 1 – Select specific cardiac phase

Step 2 – Extract vessel centerline candidates in 2D images

Step 3 – Find corresponding points in paired images with epipolar constraints

Step 4 – Reconstruct initial 3D vessel centerline geometry

Step 5 – Estimate total isocenter movement in each image

Step 6 – Calibrate isocenter movement and reconstruct final 3D vessel centerline

3.3.4.1 Step 1 – Select Specific Cardiac Phase

Since the angiographic images from two viewpoints are acquired at different timings when a monoplane angiography system is used, the frame that is captured at the same cardiac phase needs to be selected from each run of angiographic images to reconstruct the vessel centerline. The specific cardiac phase was selected manually based on the shape of the heart: the end-diastolic phase is the time that the heart size (the ventricular size) is maximum and the end-systolic phase is the time that the heart size (the ventricular size) is minimum. This manual selection was validated with the angiographic images that were acquired with ECG-gating function. The mid-diastolic and the mid-systolic phases were selected as the median time between the end-diastolic and the end-systolic phases.

3.3.4.2 Step 2 – Extract Vessel Centerline Candidates in 2D Images

The detailed explanation is provided in 2.3.4.2.

3.3.4.3 Step 3 – Find Corresponding Points in Paired Images with Epipolar Constraints

The detailed explanation is provided in 2.3.4.3.

3.3.4.4 Step 4 – Reconstruct Initial 3D Vessel Centerline

The detailed explanation is provided in 2.3.4.4.

3.3.4.5 Step 5 – Estimate Total Isocenter Movement in Each Image

The detailed explanation is provided in 2.3.5.

3.3.4.6 Step 6 – Calibrate Isocenter Movement and Reconstruct Final 3D Vessel Centerline

The detailed explanation is provided in 2.3.5.

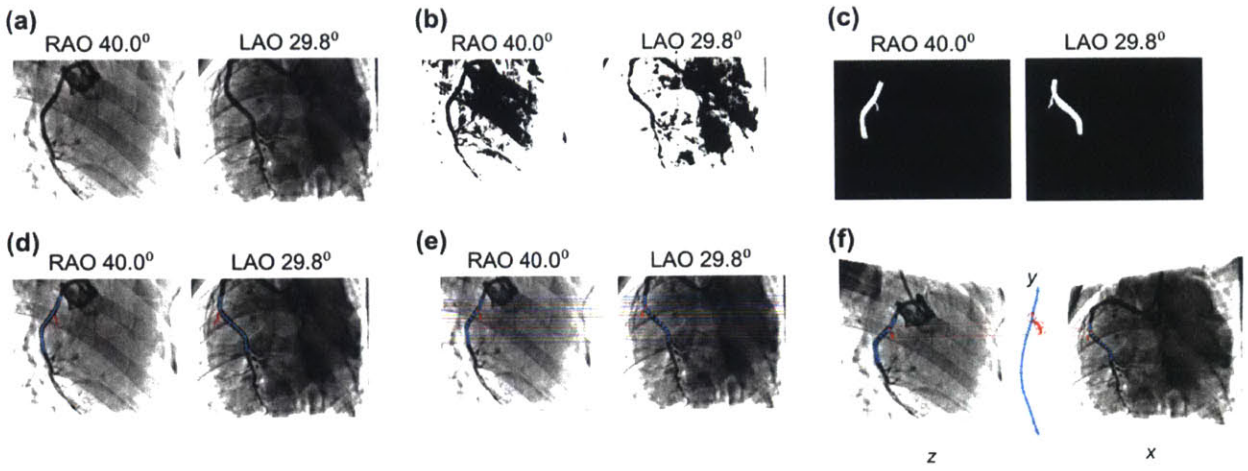

Figure 3-3 Steps of vessel centerline reconstruction

First the specific cardiac phase images are selected and imported to MATLAB **(a)**. The imported images are thresholded manually to make binary images **(b)**. Then, the edge is detected and the inside is filled morphologically **(c)**. Next, the images are skeletonized to yield the centerline candidates **(d)**. After that, the corresponding pairs of points in both images are identified by applying epipolar constraints **(e)**, and the initial vessel centerline is reconstructed using stereoscopic relations **(f)**. Following these steps, the total isocenter movement is estimated in each image. After that, the isocenter movement is calibrated and the final geometry of the vessel centerline is reconstructed.

3.3.5 Validation: Vessel Centerline Reconstruction Method

3.3.5.1 Comparison between Actual Movement and Estimated Movement

The total isocenter movement due to the machine-origin isocenter offset and the table movement can be estimated at Step 5. The estimated movement was compared to the actual movement of the table that was recorded in the DICOM headers. In addition, the difference between the estimated and the actual movements was compared to that which was evaluated in the stented phantom model (2.4.2.1).

3.3.5.2 Comparison to State-of-the-art Method

Using the same *in vivo* angiographic images, the reconstructed vessel centerline from the newly-developed method was compared with the reconstructed vessel centerline from Bourantas et al.'s method [6], which does not use the projection matrix. The root mean square error, i.e., the average distance between the reconstructed vessel centerlines, was evaluated in the stented segment.

3.3.5.3 Reproducibility across Imaging Angle Differences

After reconstructing the final geometries of the vessel centerlines from various imaging angle differences either with or without the table movement, the centerlines from the same vessel were registered on the centerline that was reconstructed from a pair of isocentric and orthogonal angiographic images by rotating rigidly to minimize the distance between two landmarks, Landmarks 1 and 2. Landmark 1 is located on the stented segment at 21 mm downstream from the intersection of the stented segment and the nearest side branch, and Landmark 2 is located on the side branch at 2 mm downstream from the intersection. The registration algorithm was defined as: (i) rotating about the origin until the distance between corresponding Landmarks 1 is minimized, and (ii) defining a vector through the origin and Landmark 1, and rotating about this vector until the distance between corresponding Landmarks 2 is minimized (Figure 3-4). Landmark 1 was used to evaluate the effect on the vessel centerline

reconstruction in the stented segment since the location of a stent can be approximately marked with the bifurcation (proximal end) and Landmark 1 (distal end). Landmark 2 is used to evaluate the uncertainty in determining the orientation of each intravascular image.

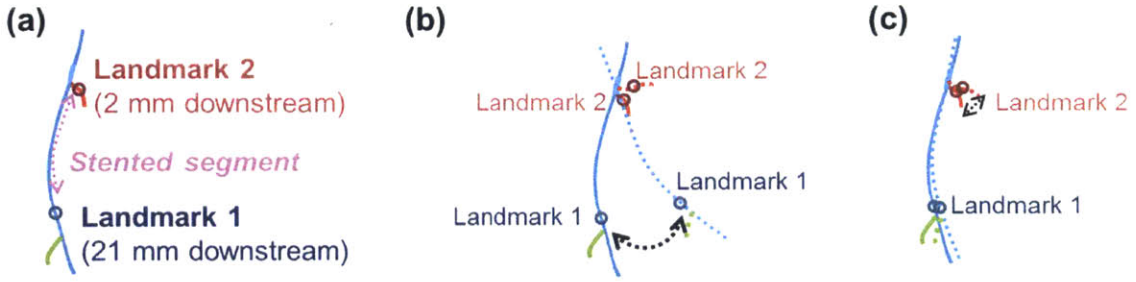

Figure 3-4 Algorithm for vessel centerline registration

First, two landmarks, Landmark 1 and 2 are set **(a)**. Then, the secondary geometry (dotted line) is rotated about the origin until the distance between corresponding Landmarks 1 is minimized **(b)**. Next, a vector through the origin and Landmark 1 is defined. Finally, the secondary geometry is rotated again about this vector until the distance between corresponding Landmarks 2 is minimized **(c)**. The solid lines represent the centerlines from orthogonal paired images or end-diastolic phase images. The dotted lines represent the centerlines from non-orthogonal paired images or from different cardiac phase images.

After registering the vessel centerlines, the reproducibility of vessel centerline reconstruction across various imaging angle differences was evaluated by comparing them to the centerline from isocentric and orthogonal paired images: (i) the difference in the stented segment length between two side branches, (ii) the distance between Landmarks 1, (iii) the difference in the maximum curvature of the stented segment, (iv) the error of the bifurcation angle, (v) the distance between Landmarks 2, and (vi) the angle between Landmarks 2. The maximum curvature in the stented segment was measured by evaluating the change in the tangent vector T along the curve s, i.e., the reconstructed vessel centerline of the stented segment, or

$$\kappa_{max} = max\left(\left\|\frac{dT(s)}{ds}\right\|\right) \quad (3\text{-}1)$$

where κ_{max} = 0 designates a straight line, and as κ_{max} approaches 1, the curvature closely represents that of a unit sphere.

3.3.5.4 Reproducibility between Different Cardiac Cycles

After reconstructing the vessel centerlines from two different end-diastolic phases, two centerlines were registered as described in Figure 3-4. Then, the reproducibility between different cardiac cycles were evaluated in terms of (i) error of stented segment length between two side branches, (ii) distance between Landmarks 1, (iii) error of the maximum curvature of the stented segment, (iv) error of the bifurcation angle, (v) distance between Landmarks 2, and (vi) angle between Landmarks 2.

3.3.6 Structural Reconstruction Method

In this thesis, angiography-OCT fusion is selected as a means of structural reconstruction of the lumen and the stent. As shown in Figure 3-5, the structural reconstruction method by angiography-OCT fusion can be separated in four steps:

Step 1 – Reconstruct vessel centerline from paired angiographic images

Step 2 – Detect lumen and stent-struts in OCT images

Step 3 – Place 2D information of lumen and stent-strut on vessel centerline

Step 4 – Interpolate lumen and stent structures

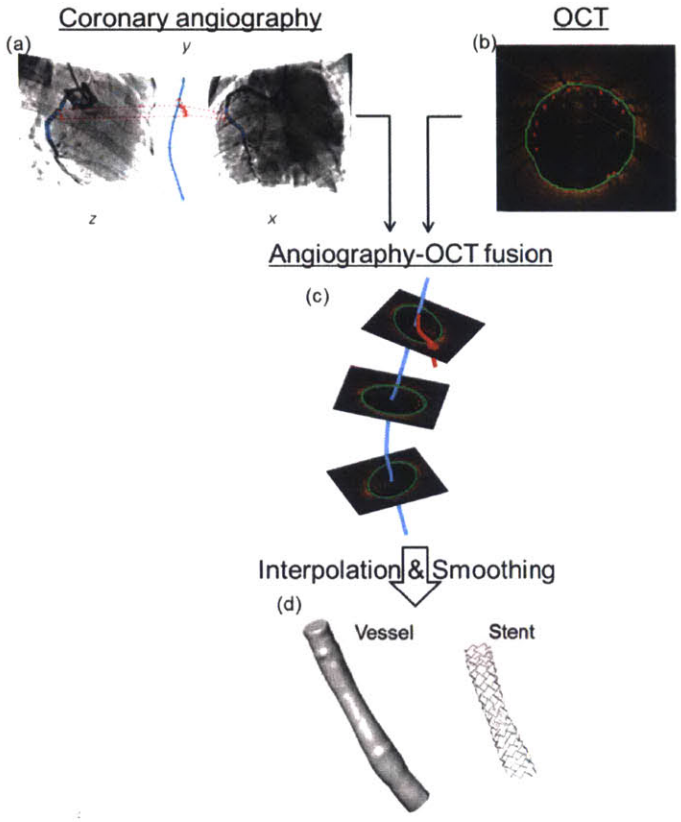

Figure 3-5 Steps for the structural reconstruction method

Step 1: The vessel centerline is reconstructed from paired coronary angiographic images **(a)**.

Step 2: The lumen surface and the stent-struts are detected in each OCT frame **(b)**.

Step 3: The information of the detected lumen surface and stent-struts are transformed in 3D space via the 3D vessel centerline that is reconstructed in Step 1 **(c)**.

Step 4: The 2D-to-3D transformed information is interpolated and smoothed to reconstruct the anatomically accurate 3D representation of the lumen and the stent **(d)**.

3.3.6.1 Step 1 – Reconstruct Vessel Centerline from Paired Angiographic Images

Since the OCT images of the stented segment are acquired over a cardiac cycle due to the fast pullback speed of OCT [1, 2], the effect of the cardiac motion on the vessel centerline needs to be evaluated to use the vessel centerline as a fusion path.

The vessel centerlines from four different cardiac phases, i.e., end-diastolic phase, mid-systolic phase, end-systolic phase, and mid-diastolic phase, were reconstructed and registered onto the end-diastolic vessel centerline with the algorithm described in Figure 3-4. The deformation of the vessel centerline over a cardiac cycle was evaluated in terms of (i) the difference in the stented segment length between two side branches, (ii) the distance between Landmarks 1, (iii) the difference in the maximum curvature of the stented segment, (iv) the difference in the bifurcation angle, (v) the distance between Landmarks 2, and (vi) the angle between Landmarks 2.

3.3.6.2 Step 2 – Detect Lumen and Stent-struts in OCT Images

From each OCT run, the range of OCT frames on which further analysis would proceed was selected. The first OCT frame was designated to be the one in which the side branch could be first distinguished from the stented artery, and the last frame was selected as the one that was an additional 10 frames from the frame that corresponded to the further end of the stent.

First, the coordinate of each OCT frame was changed from a Cartesian coordinate system to a polar coordinate system (Figure 3-6(a)). Then, the intensity distribution was evaluated in the radial direction for each θ (Figure 3-6(b)). Next, the intensity distribution was convolved with Gaussian wavelet function that is shifted by a and scaled by s in space (Equation 3-2) to assess the location of peak intensity in the radial direction (a) and the width of intensity distribution (s).

$$\frac{1}{s} f * g\left(\frac{r-a}{s}\right) dr \tag{3-2}$$

where $f(r)$: intensity distribution

$g(a,s)$: Gaussian wavelet function

After that, the lumen and the stent-strut were classified based on the scaling factor s (Figure 3-6(c)). Since the stent-strut has a narrower intensity distribution compared to the lumen in OCT images, the scaling factor of the lumen is bigger than that of the stent-strut, which enables the classification between the lumen and the stent-strut based on the scaling factor. Then, the lumen surface was interpolated and smoothed using a kernel smoothing function. A polynomial function representing the smoothed lumen surface position $\hat{r}(\theta)$ was approximated using a weighted least square estimate from the detected lumen surface data in the range of $[\theta - h(\theta), \theta + h(\theta)]$, where $h(\theta)$ is the bandwidth of the window. Tukey's tri-weight function was used to weight data points, and 0.2 was selected as a window size. This step is necessary since the stent-strut can create a shadow on the underneath structure, i.e., lumen, in the OCT images (Figure 3-6(d)). Finally, the detected lumen and stent-strut information was converted from the polar coordinate system to the Cartesian coordinate system (Figure 3-6(e)).

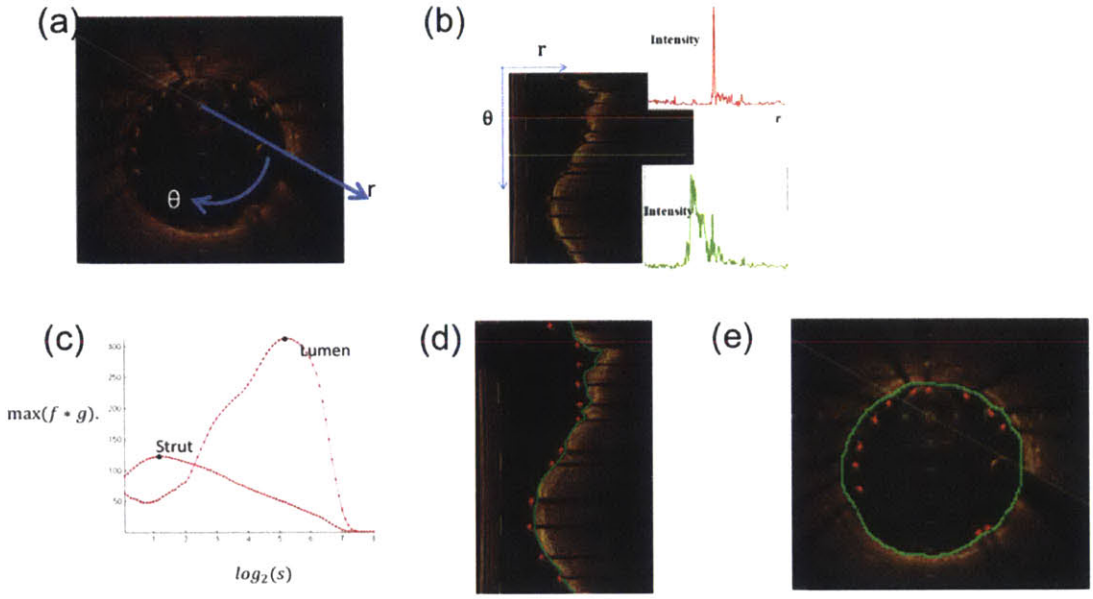

Figure 3-6 Detection of lumen surface and stent-struts in OCT images

First, he coordinate system of the image is changed from a Cartesian coordinate system to a polar coordinate system **(a)**. The intensity distribution is then evaluated in the radial direction for each angle θ **(b)**. Next, the intensity distribution is convolved with Gaussian wavelet function that is shifted by a and scaled by s in space, and the lumen and the stent-strut were classified based on the scaling factor s **(c)**. Then, the lumen surface is interpolated at the location where the stent-struts create the shadow to the underneath structure **(d)**. Finally, the detected lumen surface and stent-struts information was converted from the polar coordinate system to the Cartesian coordinate system **(e)**.

3.3.6.3 Step 3 – Place 2D Information of Lumen and Stent-strut on Vessel Centerline

To reconstruct the 3D structures of lumen and stent, the detected lumen and stent-strut information needs to be transferred to 3D space by placing each OCT frame perpendicularly onto the vessel centerline. This placement procedure has three steps: (i) estimation of the OCT inter-frame distance (3.3.6.3.1), (ii) determination of the orientation of the first OCT frame (3.3.6.3.2), and (iii) determination of the orientation of the subsequent OCT frames (3.3.6.3.3).

3.3.6.3.1 Estimation of OCT Inter-frame Distance

Since the imaging catheter can move laterally and longitudinally during each OCT run due to the cardiac motion, the effect of these movements needs to be considered in angiography-OCT fusion. The usage of the vessel centerline as a fusion path has solved the problem of lateral movement [3]; however, the problem of the longitudinal movement has not been addressed yet. Because the OCT inter-frame distance varies from its preset distance due to the longitudinal movement of the imaging catheter, the OCT inter-frame distance needs to be estimated accurately before fusing OCT images onto the vessel centerline that is reconstructed from paired angiographic images to overcome this problem.

First, the coordinate of each OCT frame was changed from a Cartesian coordinate system to a polar coordinate system (Figure 3-7 (a) and (b)). Then, the lumen surface was detected in each θ by setting the intensity threshold and smoothed with a kernel smoothing function. The intensity threshold and the bandwidth size were set experimentally as 254 in 8-bit image and 31 pixels, respectively. Next, each row, i.e., the gray scale intensity information in each θ, was translated in r-direction so that the lumen surface was located at the constant r. After this translation, the coordinate system was set as r'-θ, and the lumen surface was located at $r' = 0$ for all θ (Figure 3-7 (c)). The translated images of each OCT frame were accumulated in z-direction (Figure 3-7 (d)). After that, the stack of images was resliced in r'-direction and the image in which the stent-struts (the shadow of the stent-struts) can be clearly detected was selected (Figure 3-7 (e)). In the selected image, each row, i.e., the gray scale intensity information in each z, is moved in θ-direction to make the guidewire (the shadow of the guidewire) straight (Figure 3-7 (f)), i.e., the middle of the two edges of the guidewire (the shadow of the guidewire) was located at the constant θ. This step was necessary to compensate the twisting of the imaging catheter relative to the guidewire due to cardiac motion. Then, the heights of each stent-cell were measured based on the prior knowledge of the stent-cell shape and the preset inter-frame distance (0.2 mm for C7-XR) (Figure 3-8(g)). Next, the ratio of the measured stent-cell height over the actual

stent-cell height was calculated and the initial OCT inter-frame distance was evaluated using Equation 3-3 in the longitudinal direction.

$$\text{Intial OCT inter-frame distance} = 0.2\ \text{mm} \times \frac{\text{Measured stent-cell height}}{\text{Actual stent-cell height}} \quad (3\text{-}3)$$

After that, the updated OCT inter-frame distance x was estimated by interpolating the initial OCT inter-frame distance as a sinusoidal wave with the heart rate information that was recorded during the procedure (Equation 3-4). The sinusoidal wave was selected because cardiac motion is a repetitive pattern with a frequency of the heart rate and because automatic cardiac motion tracking was performed with a sinusoidal wave modeling for MRI cardiac imaging [7, 8]

$$x = Amp \times \sin\left(\frac{2\pi}{T} \times (t - t_p)\right) + Baseline \quad (3\text{-}4)$$

where

$$Amp = \frac{\text{Maximum initial inter-frame distance - Minimum initial inter-frame distance}}{2}$$

$$T = \frac{60\ \text{s}}{\text{Heart rate [bpm]}}$$

$$t_p = \text{Median time of maximum initial inter-frame distance} - \frac{T}{4}$$

$$Baseline = \frac{\text{Maximum initial inter-frame distance + Minimum initial inter-frame distance}}{2}$$

Finally, to consider the effect of the cardiac motion on the preset inter-frame distance, the sum of the updated OCT inter-frame distance in the stented segment was calculated for each OCT run. Then, the final estimation of the OCT inter-frame distance was determined by adjusting the updated inter-frame distance based on the difference between this sum and the actual stent length (17 mm) (Equation 3-5).

$$\text{Final OCT inter-frame distance} = \text{Updated inter-frame distance} \times \frac{\text{Actual stent length}}{\text{Sum in the stented segment}} \quad (3\text{-}5)$$

The interpolation as a sinusoidal wave is necessary to obtain the information of the OCT inter-frame distances for the frames between the edge of the stent and the nearest side branch. All the processes up to the determination of the initial OCT inter-frame distance can proceed only in the stented segment; in contrast, the nearest side branch is not always located at the proximal

or the distal edge of the stent. Therefore, the extrapolation outside of the stented segment using the physiological interpolation, i.e., the interpolation as a sinusoidal wave based on the heart rate information, is important to obtain the physiologically meaningful OCT inter-frame distance for all the regions that are used for angiography-OCT fusion.

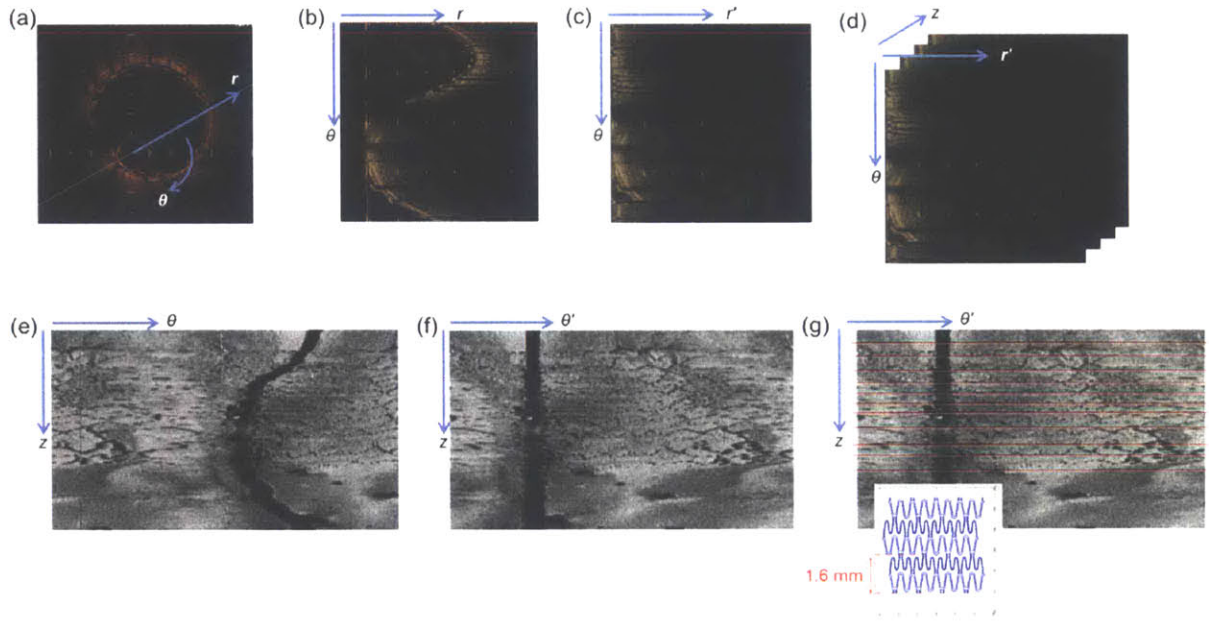

Figure 3-7 Pre-processing for the OCT inter-frame distance estimation

First, the coordinate system of each OCT frame is changed from a Cartesian coordinate system **(a)** to a polar coordinate system **(b)**. Then, the lumen surface is detected for each rotational angle of the catheter (θ) and translated in the radial direction(r) for each θ to flatten the surface of the lumen (lumen surface is located at $r' = 0$ in r'-θ coordinate system) **(c)**. Next, the translated images of each OCT frame are accumulated in z-direction **(d)**. After that, the stack of the images is resliced in r'-direction. From resliced images, the image in which the stent-struts can be clearly detected is selected **(e)**. Then, the location of the guidewire (the shadow of the guidewire) is made to be straight in the selected image **(f)**. The heights of each stent-cell are measured based on the prior knowledge of the stent-cell shape and the preset inter-frame distance (0.2 mm) **(g)**. Using the measured stent-cell heights and the actual stent-cell height, the initial OCT inter-frame distance is evaluated. This initial OCT inter-frame distance is interpolated as a sinusoidal wave with a frequency that is matched with the heart rate. The final estimation of the OCT inter-frame distance is determined by adjusting the interpolated OCT inter-frame distance based on the actual stent length (17 mm).

3.3.6.3.2 Determination of Orientation of First OCT Frame

To determine the orientation of the first OCT frame, the geometrical orientation of the nearest side branch relative to the stented segment is required. First, the position on the centerline of the stented segment at which the distance between the centerline of the stented segment and that of the side branch $|r|$ is similar to the radius of the stented artery was searched (Figure 3-8 (a)). Then, the centroid of the lumen was found in the first OCT frame, i.e., the frame in which the side branch was first distinguished from the stented artery. Next, the first OCT frame was placed at the searched position on the centerline via the centroid and was rotated until the side branch in the OCT frame was aligned with the centerline of the side branch (Figure 3-8 (b)).

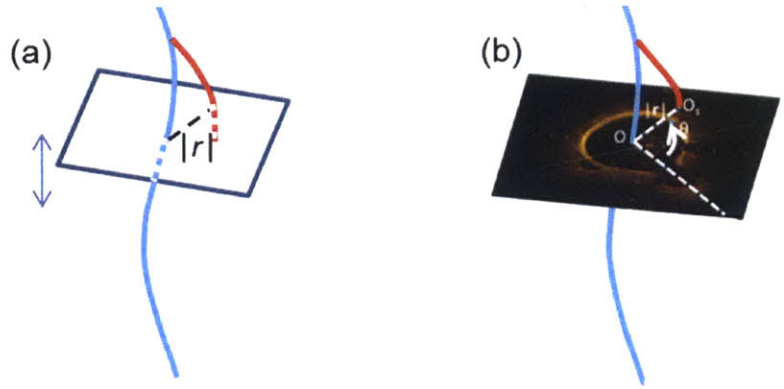

Figure 3-8 Determination of the orientation of the first OCT frame

First the location on the stented segment centerline where the distance between the centerlines of the stented segment and the side branch is similar to the radius f the stented artery is searched **(a)**. Then, the first OCT frame is placed at this location perpendicularly to the vessel centerline of the stented segment. After that, the OCT frame is rotated so that the side branch in OCT frame is coincident with the side branch centerline **(b)**.

3.3.6.3.3 Determination of Orientation of Subsequent OCT Frames

After determining the orientation of the first OCT frame, the orientations of the subsequent OCT frames needs to be determined. First, the centroid of the lumen was found in each OCT frame. Then, the second OCT frame was placed perpendicularly on the centerline of the stented segment via the centroid with an arbitrary distance from the first OCT frame and rotated by angle α that is determined by sequential triangulation method [9] so that the twisting of the imaging catheter relative to the guidewire (rotational movement of the imaging catheter due to cardiac motion) could be taken into account (Figure 3-9(a)). Next, the distance between the catheter points of both OCT frames d was measured (Figure 3-9(b)). If d was smaller than the estimated OCT inter-frame distance, the second OCT frame was replaced with a different distance from the first OCT frame and the processes were repeated. Once the orientation of the second OCT frame was determined, all the processes were repeated until the orientation of the last OCT frame was determined. An arbitrary distance was used to place the subsequent OC frames because this distance is the distance along the centerline, while the estimated OCT inter-frame distance is the distance along the imaging catheter path.

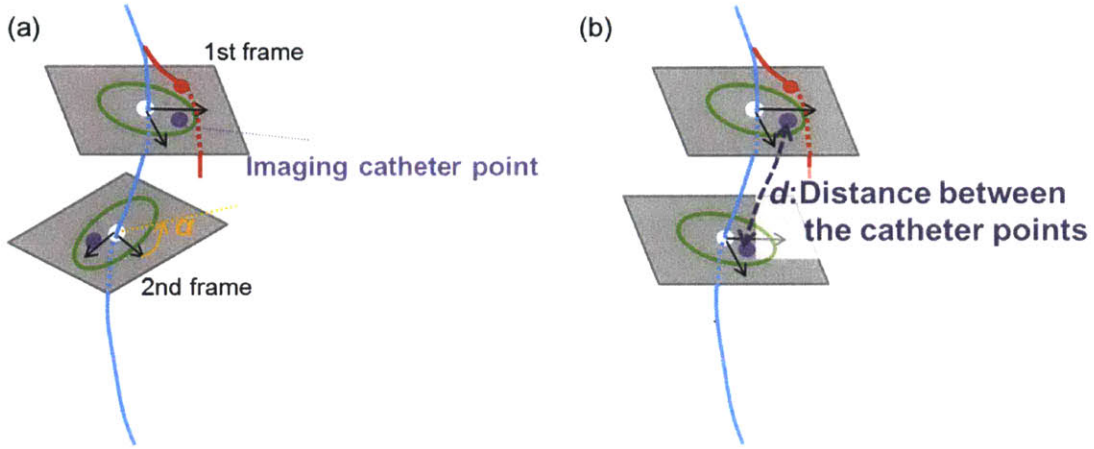

Figure 3-9 Determination of the orientation of the subsequent OCT frames

The second OCT frame is first placed perpendicularly on the stented segment centerline with the arbitrary distance from the first OCT frame. Then, it is rotated by angle α that is determined by sequential triangulation method **(a)**. Next, the distance between the catheter points of both OCT frames d is measured **(b)**. These steps are repeated until d is equal to or bigger than the estimated OCT inter-frame distance. Once the orientation of the second OCT frame is determined, all the steps are repeated for the subsequent OCT frames until the orientation of the last OCT frame is determined.

3.3.6.4 Step 4 – Interpolate Lumen and Stent structures

Since information is missing between adjacent OCT frames, the 2D-to-3D transformed information of the detected lumen and stent-strut needs to be interpolated to reconstruct smooth and physiologically realistic structures of the lumen and the stent as a final step (Figure 3-10).

For the lumen structure, the transformed points were interpolated as a bib0uniform rotational basis spline (NURBS) surface along the longitudinal direction. For the stent structure, the transformed points were interpolated with *a priori* knowledge of the stent design using a non-rigid point matching algorithm [10]. For this algorithm, the ideal stent structure was first created as a point cloud data based on the known design of the stent. Then, the transformed stent-strut information was fitted to this point cloud data non-rigidly.

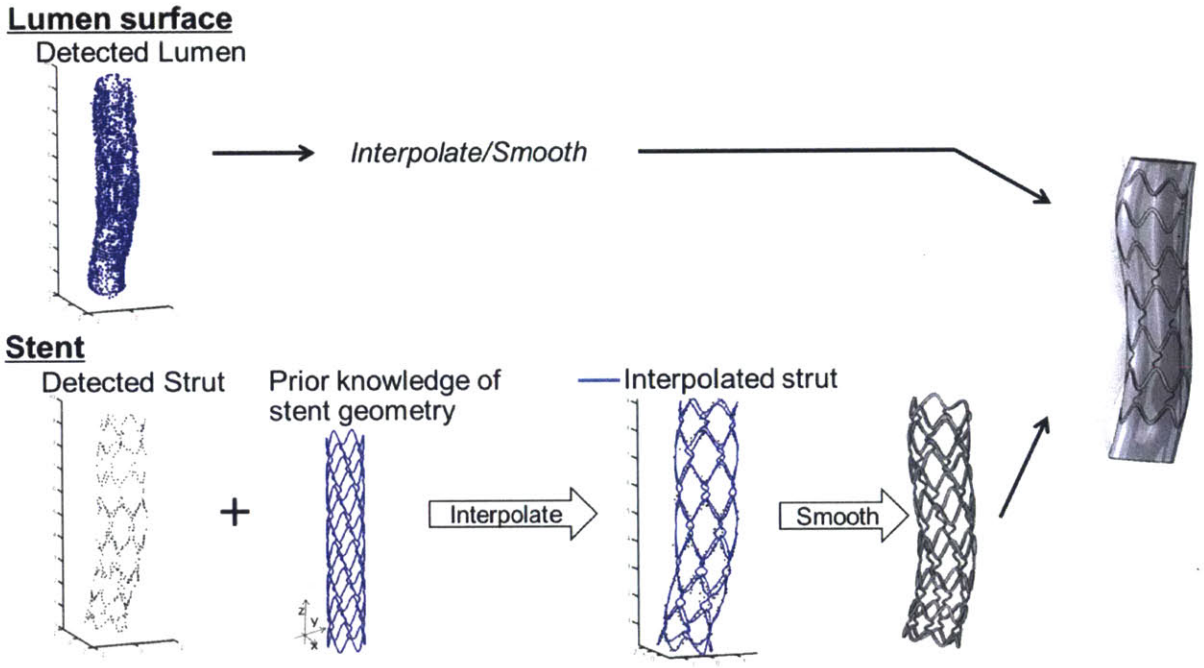

Figure 3-10 Interpolation of lumen and stent structures

As a final step of the structural reconstruction, the 3D structures of the lumen and the stent need to be interpolated and smoothed. For the lumen structure, the reconstructed geometry is interpolated and smoothed along the longitudinal direction. For the stent structure, the reconstructed geometry is interpolated using *a priori* knowledge of the stent design with a non-rigid point matching algorithm.

3.3.7 Validation: Structural Reconstruction Method

3.3.7.1 Comparison between Actual Stent Length and Reconstructed Stent Length

After reconstructing the structures of the lumen and the stent, the lengths of stents were evaluated based on the length of the stented segment centerline. All the measured stent lengths were compared to the actual stent length (17 mm).

3.3.7.2 Comparison of Reconstructed Stent Lengths between Different Time-points

Since the stent length should be the same between different time-points (post-implantation, 5-day follow-up, and 28-day follow-up), the reconstructed stent lengths were compared between post-implantation and follow-ups.

3.3.8 Time-point Registration Method

To track the vascular responses over time in 3D space, the reconstructed structures need to be registered across time. The vessel centerline can also serve as a path for time-point registration.

First, the vessel centerline was registered across time via two landmarks, Landmarks 1 and 2 as described in Figure 3-4. The accuracy of this registration relies on the accuracy of the side branch vessel centerline reconstruction. Since the side branch itself may grow and/or changeover time and since the side branch does not have any anchor for the motion, the vessel centerline reconstruction of the side branch might not be as accurate as the one of the stented artery. Therefore, a secondary registration path that is more robust to the morphological change of the vessel is necessary to improve and ensure the accuracy. Because stent structure is more rigid compared to the vessel, the stent centroid geometry that is defined after reconstructing the structures of the lumen and the stent was used as the secondary registration path. After registering the vessel centerlines at follow-ups to the one at post-implantation (Figure 3-11(a)), the stent centroid geometries at follow-ups were rigidly translated so that the both ends of the stent centroid geometries are coincident between post-implantation and follow-ups. Then, the stent centroid geometries at follow-ups were rotated around the axis that connects two ends of the stent centroid geometry at post-implantation until the total distance between the stent centroid geometries at different time-points was minimized (Figure 3-11(b)). All the interpolated structures of the lumen and the stent were translated rigidly in the same manner.

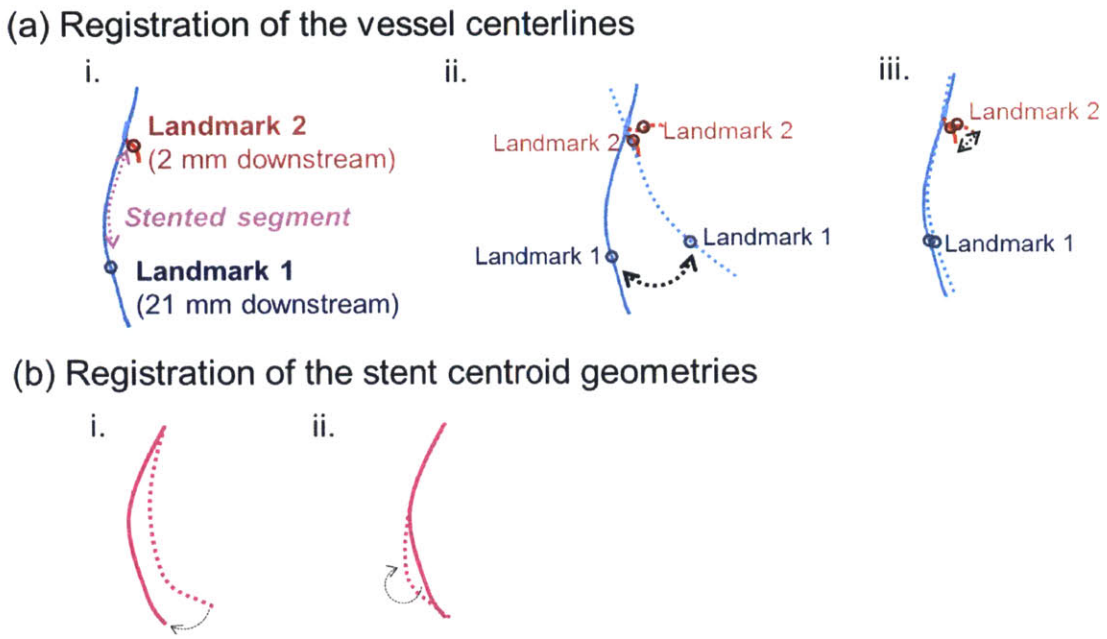

Figure 3-11 Steps for the time-point registration method

First, the vessel centerline at follow-up is registered to the vessel centerline at post-implantation **(a)**. Two landmarks, Landmark 1 and 2, are set on each reconstructed centerline **(a-i)**. Then, the centerline at follow-up is rotated around the origin to minimize the distance between the corresponding Landmarks 1 **(a-ii)**. Next, the vector between the origin and Landmark 1 is determined and the vessel centerline at follow-up is rotated around this vector until the distance between the corresponding Landmark 2 is minimized **(a-iii)**.

Secondary, the stent centroid geometry at follow-up is registered to that at post-implantation **(b)**. The stent centroid geometry at follow-up is rigidly translated so as that the both ends of the stent centroid geometries at different time-points are coincident to each other **(b-i)**. Then, the stent centroid geometry at follow-up is rotated around the axis that connects two ends of the stent centroid geometry to minimize the distance between two geometries **(b-ii)**.

The solid lines represent the vessel centerlines or the stent centroid geometry at post-implantation and the dotted lines represent those at follow-up.

3.3.9 Validation: Time-point Registration Method

The error of the time-point registration method was evaluated by the shift of stent-strut from post-implantation to 5-day or 28-day follow-up. The interpolated stent structure was represented as a point cloud. Since this interpolation proceeded from the same point cloud datasets of the stent design and since the original data (pre-interpolated 2D-to-3D translated stent geometries) were already aligned between different time-points, the corresponding points between different time-points can be easily found. The stent-strut shift was evaluated by measuring the distances of the corresponding points between post-implantation and follow-ups.

3.4 Results and Discussions

3.4.1 Vessel Centerline Reconstruction Method

The vessel centerline reconstruction method was validated in a preclinical setting using *in vivo* swine model by (i) comparing the estimated total isocenter movement to the actual table movement (3.4.1.1), (ii) evaluating 3D-to-2D back-projected distance before and after applying the algorithm for non-isocentric paired angiographic images (3.4.1.2), (iii) comparing this method to the state-of-the-art method (3.4.1.3), (iv) evaluating the reproducibility across imaging angle differences (3.4.1.4), and (v) evaluating the reproducibility between different cardiac cycles (3.4.1.5). All the values were represented as mean ± standard deviation.

3.4.1.1 Comparison between Actual Movement and Estimated Movement

As explained in 2.3.5, the new algorithm for non-isocentric paired angiographic images can estimate the total isocenter movement in each image. Table 3-2 summarizes the difference between the actual movement and the estimated movement (N = 64 in total, N = 32 for left anterior descending artery and N=32 for left circumflex artery). Since the new algorithm cannot distinguish between the machine-origin isocenter offset and the table and/or object movement, the difference between the actual movement and the estimated movement can be considered as the machine-origin isocenter offset and/or the object movement. Similar to the static phantom model result (2.4.2.1), these differences represent less than 1% of the distance between the X-ray source and the intensifier: 0.23% ± 0.10% for left anterior descending artery and 0.34% ± 0.13% for left circumflex artery at maximum. In addition, these differences are quite similar to the ones in the stented phantom model (2.4 mm ± 1.0 mm and 3.6 mm ± 1.3 mm vs. 3.6 mm ±1.0 mm), so is the error (10.1% ± 4.1% and 15.1% ± 5.3% vs. 10.4% ± 2.8%). Slight differences between the preclinical results and the stented phantom model are likely caused by as the movement of the object, i.e., the swine itself. Since the swine is anesthetized during the procedure, the object movement is expected to be minimal, which is consistent with the finding.

Table 3-2 Comparison between the actual movement and the estimated movement

LAD: Left anterior descending artery (N=32), LCX: Left circumflex artery (N=32)

		Actual movement [mm]	Estimated movement [mm]	Difference [mm]	Error [%]
Preclinical data	LAD	23.8	26.2±1.0	2.4±1.0	10.1±4.1
	LCX	23.8	27.4±1.3	3.6±1.3	15.1±5.3
Stented phantom model		35.2	31.6±1.0	3.6±1.0	10.4±2.8

3.4.1.2 3D-to-2D Back-projected Distance Error

Another way to evaluate the effectiveness of the new algorithm for non-isocentric paired angiographic images is to compare 3D-to-2D back-projected distance errors that are calculated with Equation 2-12 before and after applying this new algorithm. As summarized in Table 3-3, the 3D-to-2D back-projected distance error was improved by approximately 30-fold by applying the new algorithm. Moreover, the errors in the preclinical setting were similar to or only slightly larger than the ones measured in the stented phantom model. This result and the result in 3.4.1.1 demonstrate that the new algorithm is effective in the preclinical setting and that its accuracy and precision are quite similar to those with the stented phantom model.

Table 3-3 Comparison of 3D-to-2D back-projected distance error

LAD: Left anterior descending artery (N=32), LCX: Left circumflex artery (N=32)

		Before applying	After applying
Preclinical data	LAD	16.9 mm, 50.0 pixel	0.778 mm, 2.30 pixel
	LCX	16.7 mm, 49.4 pixel	0.437 mm, 1.29 pixel
Stented phantom model		25.4 mm, 65.0 pixel	0.768 mm, 1.97 pixel

3.4.1.3 Comparison to State-of-the-art Method

To understand the improvement in the accuracy of the newly developed vessel centerline reconstruction method, the reconstructed vessel centerline with this method was compared to the one with Bourantas et al.'s method [6] using the same pair of angiographic images.

Bourantas et al.'s method [6] was selected because it does not use the projection matrix, which is used in the newly developed method. As shown in Figure 3-12, the newly developed vessel centerline reconstruction method yielded a quite similar shape in the stented segment. The root mean square error between these two vessel centerline in the stented segment was 0.27 mm or 0.76 pixel, which is similar to or smaller than the error with Yang et al.'s method (0.26 mm or 1.3 pixel) [11]. This result suggests that the newly developed method is comparable to the state-of-the-art method. As summarized in Table 3-1, the newly developed method is superior to the state-of-the-art methods because it can handle both non-isocentric and non-orthogonal paired angiographic images and because it can estimate the total isocenter movement in each image.

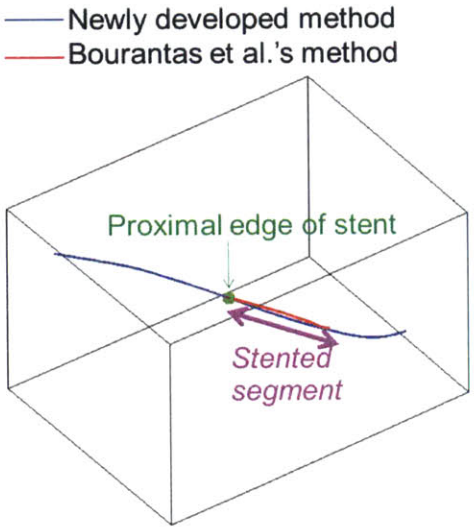

Figure 3-12 Comparison between the newly developed vessel centerline reconstruction method and the state-of-the-art method
The vessel centerline reconstructed with the newly developed method had a quite similar shape to that with Bourantas et al.'s method in the stented segment. The root mean square error between these two vessel centerlines was similar or smaller than the error with Yang et al.'s method (0.27 mm or 0.76 pixel vs. 0.26 mm or 1.3 pixel).

3.4.1.4 Reproducibility across Imaging Angle Differences

The reproducibility across imaging angle differences was evaluated using two sets of angiographic images: isocentric images whose imaging angle differences varied from 50^0 to 130^0 (N = 48; 4 vessels, 12 patterns of imaging angle difference/vessel) and non-isocentric images whose imaging angle differences varied from 20^0 to 130^0 (N=64; 2 vessels, 16 patterns of

imaging angle difference/vessel, 2 movement patterns/imaging angle difference). For isocentric images, the reproducibility was evaluated in terms of the distance between Landmarks 1, the distance between Landmarks 2, of the difference in the bifurcation angle, the angle between Landmarks 2, and the difference in the maximum curvature of the stented segment. For non-isocentric images, the reproducibility was evaluated in terms of the difference in the stented segment length between two side branches, the distance between Landmarks 1, the distance between Landmarks 2, and the angle between Landmarks 2. All the results are summarized in Table 3-4. All the evaluation was performed based on the vessel centerline from the isocentric and orthogonal paired images and presented as mean ± standard deviation. Figure 3-13 shows all the registered vessel centerlines from one stented vessel.

Table 3-4 Reproducibility of the vessel centerline reconstruction across imaging angle differences

	Difference in stented segment length between two branches	Distance between pair of Landmark 1	Distance between pair of Landmark 2	Difference in bifurcation angle	Angle between pair of Landmark 2	Difference in maximum curvature of stented segment
Isocentric images		(0.11±0.10) mm (0.39±0.34) pixel	(0.83±0.58) mm (2.90±2.01) pixel	$13.7^{o}\pm10.8^{o}$	$24.3^{o}\pm17.4^{o}$	0.11±0.09
Non-isocentric images	(3.3±2.2) mm (9.8±6.4) pixel	(0.46±0.28) mm (1.37±0.82) pixel	(0.38±0.47) mm (1.12±1.38) pixel		$10.9^{o}\pm16.6^{o}$	
Stented phantom model	Error of length: (1.8 ±1.6) mm, (4.4 ±4.3) pixel			Error of angle: $0.9^{o}\pm0.9^{o}$		

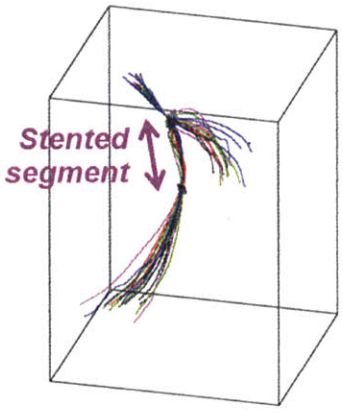

Figure 3-13 Reproducibility of the vessel centerline reconstruction across various imaging angle differences (20^{0}-130^{0})

All the vessel centerlines from non-orthogonal pairs of angiographic images were registered to the centerline from an orthogonal pair of angiographic images. The vessel centerlines in the stented segment from various imaging angle differences (20^{0}-130^{0}) were aligned well after the registration.

Although the difference in the stented segment length between two side branches was bigger than that of the stented phantom model, these two values have similar order when compared to the based length or the actual length (8.8% ± 5.9% vs. 4.4% ± 4.0%). Moreover, the distances between Landmarks 1 were smaller than the static error of length and the distance from the intersection of the stented segment and the nearest side branch (21 mm) in both isocentric and non-isocentric paired angiographic images. In addition, the difference in the maximum curvature of the stented segment was quite small. These results suggest that the newly developed vessel centerline reconstruction method is as robust to the imaging angle differences (20°-130°) in the preclinical setting as in the stented phantom model. On the other hand, the difference in the bifurcation angle was bigger than that in the stented phantom model. This is likely due to the twisting of the side branch over time because the side branch does not have any constraints to its movement, unlike the relatively rigid stented segment. The facts that the distance between Landmarks 2 is bigger than the static error of length and that the angle between Landmarks 2 is widely varied support this possibility that the side branch twisting us responsible for the large difference in the bifurcation angle.

The potential error in angiography-OCT fusion due to the imaging angle differences can be estimated based on the distance between Landmarks 2 and the angle between Landmarks 2 since the orientation of the first OCT frame, i.e., the location on the centerline of the stented segment and the in-plane rotation angle, is determined by the geometrical relationship between the stented segment centerline and the nearest side branch centerline. The location on the centerline of the stented segment is determined by the distance between the stented segment centerline and the nearest side branch centerline; thus, this error can be predicted from the distance between Landmarks 2. For non-isocentric images, the distance between Landmarks 2 was 0.38 mm ± 0.47 mm, which is 2.2% ± 2.8% of the actual stent length. The angle between Landmarks 2 can predict the error of in-plane rotation angle because in-plane rotation angle is determined by the direction from stented segment centerline to the side branch centerline. For

non-isocentric images, the angle between Landmarks 2 was $10.9^0 \pm 16.6^0$, which is 3.03% ± 4.61% of the entire rotation (360^0). From these results, the potential error of the structural reconstruction due to the imaging angle differences can be estimated as approximately 2-3%, which is quite small.

3.4.1.5 Reproducibility between Different Cardiac Cycles

Since the paired angiographic images are acquired at different timings and since the OCT images are acquired before or after the angiographic images are acquired, the reproducibility of the vessel centerline from different cardiac cycles needs to be evaluated to understand the influence of the different cardiac cycles on the vessel centerline reconstruction itself and angiography-OCT fusion. The reproducibility between different cardiac cycles was also evaluated using two sets of angiographic images: isocentric and non-isocentric image datasets. For isocentric images, the reproducibility was evaluated in terms of the distance between Landmarks 1, the distance between Landmarks 2, of the difference in the bifurcation angle, the angle between Landmarks 2, and the difference in the maximum curvature of the stented segment. For non-isocentric images, the reproducibility was evaluated in terms of the difference in the stented segment length between two side branches, the distance between Landmarks 1, the distance between Landmarks 2, and the angle between Landmarks 2. All the results are summarized in Table 3-5. The evaluation was performed based on the vessel centerline from the first end-diastolic phase and presented as mean ± standard deviation. Figure 3-14 shows all the registered vessel centerlines from two stented vessels.

Table 3-5 Reproducibility of the vessel centerline reconstruction between different cardiac cycles

	Difference in stented segment length between two branches	Distance between pair of Landmark 1	Distance between pair of Landmark 2	Difference in bifurcation angle	Angle between pair of Landmark 2	Difference in maximum curvature of stented segment
Isocentric images		(0.06±0.07) mm (0.22±0.26) pixel	(0.40±0.13) mm (1.40±0.44) pixel	9.7°±5.9°	11.6°±3.8°	0.065±0.029
Non-isocentric images	(3.0±1.6) mm (8.8±4.7) pixel	(0.30±0.13) mm (0.89±0.38) pixel	(0.23±0.15) mm (0.69±0.44) pixel		3.6°±2.8°	
Stented phantom model	Error of length: (1.8 ±1.6) mm, (4.4 ±4.3) pixel			Error of angle: 0.9°±0.9°		

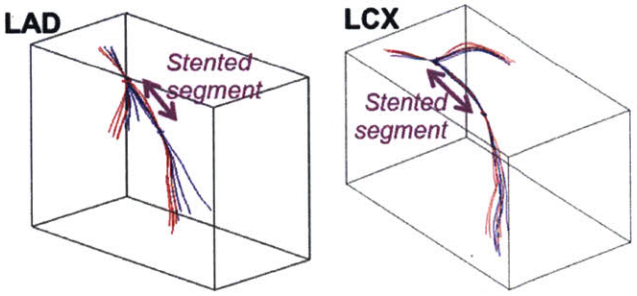

Figure 3-14 Reproducibility of the vessel centerline reconstruction between different cardiac cycles
The vessel centerlines from different cardiac cycles were aligned well, especially in the stented segment, after the registration. Blue and red lines represent different cardiac cycles.
LAD and LCX stand for left anterior descending artery and left circumflex artery, respectively.

The reproducibility between different cardiac cycles shows the similar findings to those of the reproducibility across imaging angle differences. The difference in the stented segment length between two side branches was larger than the static error of length, but these two values have similar order when compared to the based length or the actual length (7.9% ± 4.3% vs. 4.4% ± 4.0%). The distances between Landmarks 1 were smaller than the static error of length and the distance from the intersection of the stented segment and the nearest side branch in both imaging sets. The difference in the maximum curvature of the stented segment was quite small. These results suggest that the newly developed vessel centerline reconstruction method has a high reproducibility between different cardiac cycles in the stented segment. In contrast,

due to the twisting of the side branch, the difference in the bifurcation angle was bigger than the static error of the bifurcation angle. This is also supported by the bigger distance between Landmarks 2 and the widely-varied angle between Landmarks 2.

The potential error in angiography-OCT fusion due to the usage of the different cardiac cycles can be estimated in a similar manner to the one done in 3.4.1.4. For non-isocentric images, the distance between Landmarks 2 was 0.23 mm ± 0.15 mm, which represents 1.4% ± 0.9% of the stent length, and the angle between Landmark 2 was $3.6^0 \pm 2.8^0$, which is 1.0% ± 0.8% of the entire rotation. Since these values are smaller than those due to the imaging angle differences, the error of the structural reconstruction due to the usage of the different cardiac cycles can be considered to be within the error due to the imaging angle differences.

3.4.2 Structural Reconstruction Method

As explained in 3.3.6, the structural reconstruction method has four steps. This method was validated at each step.

3.4.2.1 Deformation of Vessel Centerline over a Cardiac Cycle

Since the OCT images of the stented segment are acquired over approximately a single cardiac cycle due to the fast pullback speed of OCT [1, 2], the deformation of the vessel centerline needs to be evaluated to understand the potential error in angiography-OCT fusion when the vessel centerline is used as a fusion path. The vessel centerlines were reconstructed from four different cardiac phases, i.e., end-diastolic, mid-systolic, end-systolic, and mid-diastolic phases, and registered to the centerline from the end-diastolic phase. The deformation of the vessel centerline over a cardiac cycle was also evaluated with two sets of angiographic images: isocentric and non-isocentric images. For isocentric images, the deformation was evaluated in terms of the distance between Landmarks 1, the distance between Landmarks 2, of the difference in the bifurcation angle, the angle between Landmarks 2, and the difference in the

maximum curvature of the stented segment. For non-isocentric images, the reproducibility was evaluated in terms of the difference in the stented segment length between two side branches, the distance between Landmarks 1, the distance between Landmarks 2, and the angle between Landmarks 2. All the results are summarized in Table 3-6 and all the values were represented as mean ± standard deviation. Figure 3-15 shows all the registered vessel centerlines from two stented vessels.

Table 3-6 Deformation of the vessel centerline over a cardiac cycle

	Difference in stented segment length between two branches	Distance between pair of Landmark 1	Distance between pair of Landmark 2	Difference in bifurcation angle	Angle between pair of Landmark 2	Difference in maximum curvature of stented segment
Isocentric images		(0.42 ±0.54) mm (1.47 ±0.26) pixel	(0.49±0.38) mm (1.69±1.32) pixel	13.7°±10.9°	14.0°±11.1°	0.072±0.061
Non-isocentric images	(4.3±1.7) mm (12.7±4.9) pixel	(0.33±0.21) mm (0.97±0.61) pixel	(0.38±0.29) mm (1.11±0.87) pixel		7.1°±6.0°	
Stented phantom model	Error of length: (1.8 ±1.6) mm, (4.4 ±4.3) pixel			Error of angle: 0.9°±0.9°		

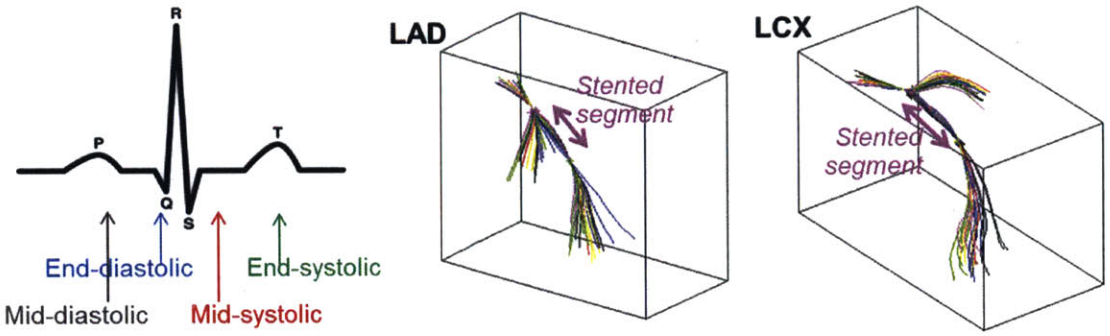

Figure 3-15 Deformation of the vessel centerline over a cardiac cycle

The vessel centerline did not deform significantly within the stented segment because the stent can serve as an anchor for the cardiac motion over a cardiac cycle.

Blue, red, green, and black lines represent the vessel centerlines at end-diastolic, mid-systolic, end-systolic, and mid-diastolic phases, respectively, as shown in the ECG pattern.

LAD and LCX stand for left anterior descending artery and left circumflex artery, respectively.

The difference in the stented segment length between two side branches was larger than the static error of length, butthe distances between Landmarks 1 were smaller than the static error of length and the distance from the intersection of the stented segment and the nearest side branch in both imaging sets. The difference in the maximum curvature of the stented segment was quite small. In addition, all the results were quite similar to the reproducibility results (3.4.1.4, Table 3-4 and 3.4.1.5, Table 3-5). These findings suggest that the vessel centerline in the stented segment does not deform significantly over a cardiac cycle. On the other hand, the difference in bifurcation angle was bigger than the static error, and the distance between the pair of Landmarks 2 was also bigger than the root mean square error that was evaluated in 3.4.1.3. But, considering that both of them and the angle between the pair of Landmarks 2 were similar to the results of reproducibility between different cardiac cycles, the twisting of the side branch over time is likely to be at the root of these results.

The potential error in angiography-OCT fusion due to the deformation of the vessel centerline over a cardiac cycle was also evaluated based on the distance between Landmarks 2 and the angle between Landmarks 2. For non-isocentric images, the distance and the angle between Landmarks 2 were 0.38 mm ± 0.29 mm and 7.1^0 ± 6.0^0, respectively. These values represent 2.2% ± 1.7% of the actual stent length and 2.0% ± 1.7% of the entire rotation; therefore, the error of the structural reconstruction due to the deformation of the vessel centerline over a cardiac cycle can be estimated to be approximately 2%. Combined with the results of the reproducibilities across imaging angle differences and between different cardiac cycles, the potential error in the structural reconstruction from the vessel centerline reconstruction part can be predicted to be approximately 3%, which is relatively small.

Based on the fact that no significant deformation of the vessel centerline was observed in the stented segment over a cardiac cycle, the vessel centerline from the end-diastolic phase was selected as a fusion path. The end-diastolic phase was chosen for two reasons: (i) blood perfusion into the coronary artery mainly occurs at the diastolic phase [12, 13], and (ii) higher

reproducibility was achieved experimentally when the end-diastolic phase was used as opposed to other cardiac phases.

3.4.2.2 Sensitivity and Specificity of Lumen and Stent-struts Detection in OCT Images

To understand the potential error in the 3D structural reconstruction, the accuracy of the lumen and stent-strut detection in OCT images was evaluated using one stented vessel. This detection is performed automatically with the classifier, i.e., the value of scale factor *s*, that was trained in advance with several imaging data and human inputs that tell the classification between lumen and stent-struts. The receiver-operator characteristic curve (Figure 3-16) showed an area under the curve for the detection of the stent-struts to be 0.99 and the lumen to be approximately 1.0 with high sensitivity (0.94-1.0) and high specificity (0.83-0.99).

In addition, the automatic detection results were compared to the conventional manual detection results from the console. The average difference between lumen and stent areas between the two methods were 0.42 ± 0.13 mm^2 or 5.4% ± 0.19% (N = 62 frames, R^2 = 0.97) and 0.20 ± 0.17mm^2 or 3.1% ± 0.4% (N = 57 frames, R^2 = 0.98), respectively.

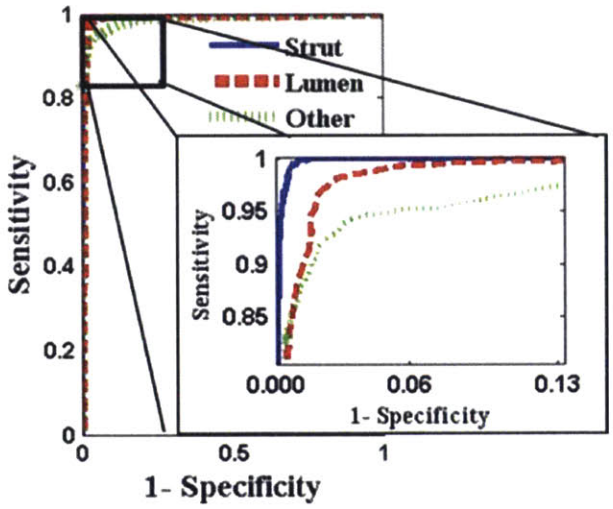

Figure 3-16 Receiver-operator characteristic curve for lumen and stent-strut detection

The area under the curve for the detection of the stent-struts was 0.99 and that of the lumen was approximately 1.0. The sensitivity was 0.94-1.0 and the specificity was 0.83-0.99.

3.4.2.3 Effectiveness of OCT Inter-frame Distance Correction

The correction of the OCT inter-frame distance can overcome the problem that arises from the longitudinal movement of the imaging catheter due to the cardiac motion. This correction is based on the heart rate and the expansion/shrinkage of the measured stent-cell height in the OCT images relative to the actual stent-cell height. By interpolating the measured OCT inter-frame distance as a sinusoidal wave with the recorded heart rate, the estimation of the OCT inter-frame distance becomes more physiologically realistic and meaningful (Figure 3-17). The effectiveness of the OCT inter-frame distance correction can be seen in two aspects. First, when the resliced OCT image was reorganized based on the estimated OCT inter-frame distance, all stent-cells were equally distributed in the longitudinal direction (Figure 3-18). Second, the reconstructed stent structures with the estimated OCT inter-frame distance had similar length to the actual stent length (17 mm), while those with the preset OCT inter-frame distance had quite variable abd inaccurate length compared to its actual length (Figure 3-19).

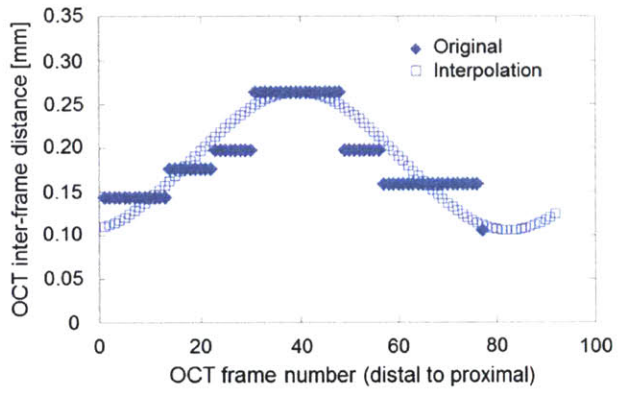

Figure 3-17 Initial OCT inter-frame distance and its interpolated result
The initial OCT inter-frame distance is obtained based on the measured stent-cell height. It is interpolated as a sinusoidal wave with a frequency that was calculated from the recorded heart rate. This interpolation enables evaluating the inter-frame distance in a physiologically realistic and meaningful way. It also enables the extrapolation of the OCT inter-frame distance outside of the stented segment.

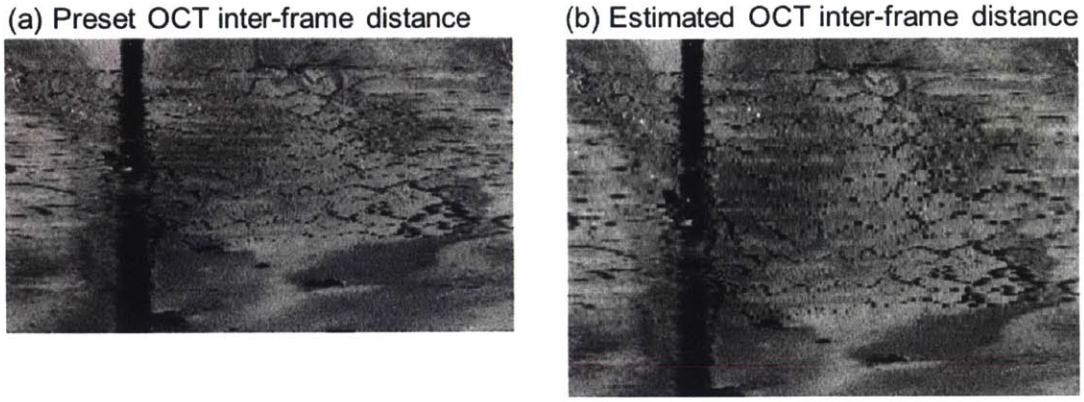

Figure 3-18 Resliced OCT image with the preset OCT inter-frame distance (a) and with the estimated OCT inter-frame distance (b)

When the preset, constant OCT inter-frame distance is used, the stent-cell is not equally distributed in the longitudinal direction due to the longitudinal movement of the imaging catheter **(a)**. This longitudinal movement problem is overcome by correcting with the estimated OCT inter-frame distance, and the stent-cell is equally distributed in the longitudinal direction **(b)**.

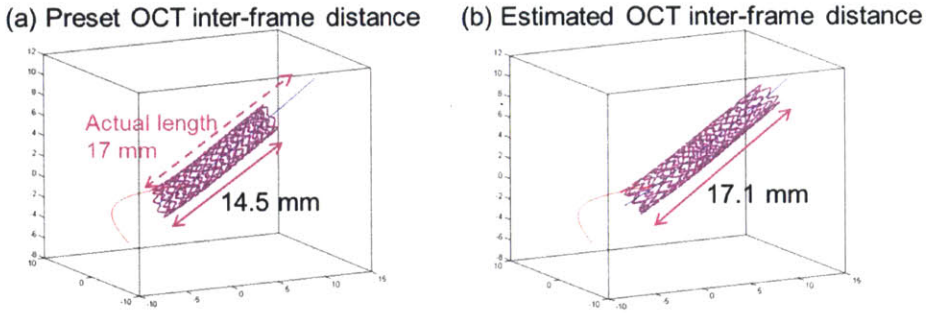

Figure 3-19 Reconstructed stent structures with the preset OCT inter-frame distance (a) and with the estimated OCT inter-frame distance (b)

When the preset OCT inter-frame distance is used, the stent length is widely varied from its actual length **(a)**. In contrast, when corrected with the estimated OCT inter-frame distance, the stent length is similar to its actual length **(b)**.

The effectiveness of the OCT inter-frame distance correction was evaluated in terms of (i) the difference between the actual stent length and the reconstructed stent length and (ii) the difference of the reconstructed stent length between post-implantation and follow-ups. Both values were compared between the cases when the preset OCT inter-frame distance (0.2 mm)

was used and when the estimated OCT inter-frame distance was used. As summarized in Table 3-7 and 3-8, by using the estimated OCT inter-frame distance, the difference between the actual stent length and the reconstructed stent length was improved by approximately 2.3-fold and the difference between different time-points was improved by approximately 2.1-fold. In addition, when the estimated OCT inter-frame distance was used, the difference between the actual stent length and the reconstructed stent length was similar order to the one with Tu et al.'s method [14] that was evaluated from the length between two landmarks using phantom models (-0.19 mm ± 0.50 mm vs. 0.05 mm ± 0.25 mm). These results suggest that more accurate 3D reconstruction of the lumen and the stent structures can be achieved by correcting the OCT inter-frame distance and that this method has a similar accuracy in the preclinical setting where the cardiac motion affects the results in a more physiologically realistic situation than the static phantom model setting. Therefore, the effect of cardiac motion, especially the longitudinal movement of the imaging catheter caused by cardiac motion, is considered to be overcome with this newly developed structural reconstruction method.

Table 3-7 Difference between the actual stent length and the reconstructed stent length

All values were represented as mean ± standard deviation.

Pre-processing (Preset inter-frame distance)		Post-processing (Estimated inter-frame distance)	
Absolute difference	Error	Absolute difference	Error
0.94 mm±0.76 mm	5.5%±4.5%	0.41 mm±0.34 mm	2.4%±2.0%

Table 3-8 Difference of the reconstructed stent length between post-implantation and follow-ups

All values were represented as mean ± standard deviation.

Pre-processing (Preset inter-frame distance)		Post-processing (Estimated inter-frame distance)	
Absolute difference	Error	Absolute difference	Error
1.20 mm±0.99 mm	7.0%±5.6%	0.56 mm±0.41 mm	3.3%±2.3%

3.4.3 Time-point Registration Method

3.4.3.1 Importance of Stent Centroid Geometry for Time-point Registration Method

Since the vessel grows, changes, and moves over time and especially since no constraints to the motion exist in the side branch, unlike the stented segment, the morphology and the anatomical position of the side branch may change over time and its geometrical relationship to the stented segment may also change over time. These changes may affect the vessel centerline reconstruction of the nearest side branch, which leads to the error in time-point registration when the vessel centerline only is used as a fusion path. Therefore, a secondary registration path is necessary that is more robust to the physiological change of the vessel over time. Because the stent is more rigid than the vessel, the stent centroid geometry was selected as the secondary registration path. To understand the effectiveness and the importance of this secondary registration path, the stent-strut shift between post-implantation and 5-day or 28-day follow-up was evaluated (Figure 3-20, Table 3-9). By using the stent centroid as a secondary registration path, the stent-strut shift was improved approximately 1.6-fold. In addition, the lumen structures that were proximal and distal to the stent, i.e., the regions where no vascular responses to stent implantation have occurred, were coincident between different time-points, while the lumen became narrower within the stented segment due to the vascular responses (Figure 3-21).

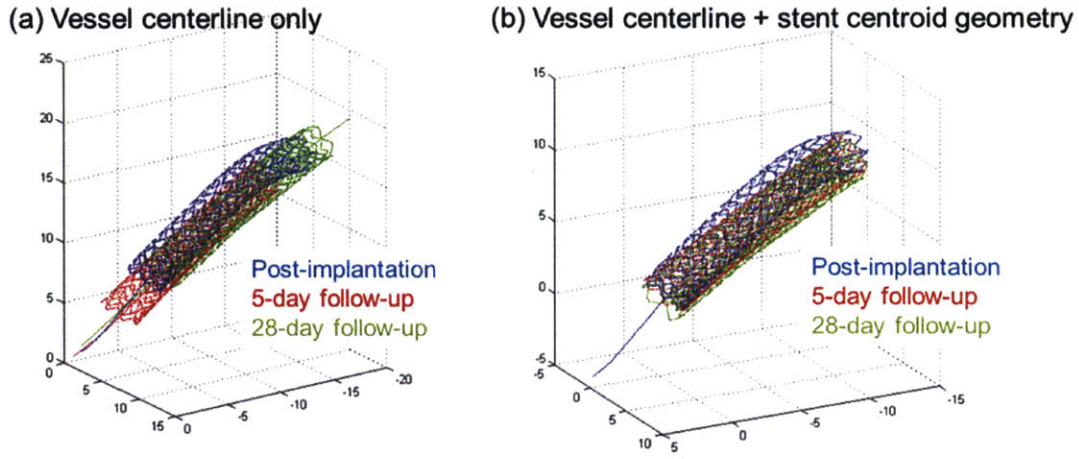

Figure 3-20 Comparison of the time-point registration method between the vessel centerline only being used (a) and both the vessel centerline and stent centroid geometry being used (b)

When the vessel centerline only is used as a fusion path, the reconstructed stent structures at different time-points are not aligned well **(a)**. By using the stent centroid geometry as a secondary fusion path, the alignment of the reconstructed structures is improved **(b)**.

Table 3-9 Error of the time-point registration method:
The stent-strut shift between post-implantation and follow-ups
All values were represented as mean ± standard deviation.

Vessel centerline only		Vessel centerline + stent centroid geometry	
Averaged absolute difference from post-implantation	Relative to stent length	Averaged absolute difference from post-implantation	Relative to stent length
2.6 mm ± 1.4 mm	15.0% ± 8.0%	1.6 mm ± 0.5 mm	9.2% ± 3.0%

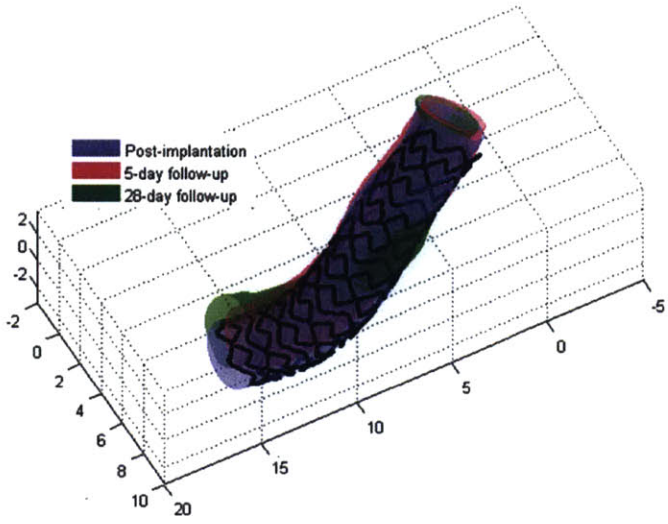

Figure 3-21 Time-point registration: Registered lumen structures

The lumen surfaces of the proximal and distal regions to the stent aligned well. In contrast, due to the vascular responses to stent implantation, the lumen became narrower at follow-ups than at post-implantation.

3.4.3.2 Potential Causes for Error in Time-point Registration

Although the error of the time-point registration was improved by using the stent centroid geometry as a secondary registration path, the residual error was still significant. The stent-strut shift between post-implantation and follow-up images was 1.6 mm ± 0.5 mm or 9.2% ± 3.0% of the actual stent length, which is approximately 3 times larger than the error in the structural reconstruction (0.56 mm ± 0.41 mm or 3.3% ± 2.3%). The newly developed time-point registration method assumes that the stent centroid geometry will not change over time; however, this assumption may not be true. The stent itself may deform over time because the pressure on the stent may not be equally distributed due to (i) the difference in the tissue types that surround the artery and (ii) the difference in vascular responses to stent implantation (Figure 3-22).

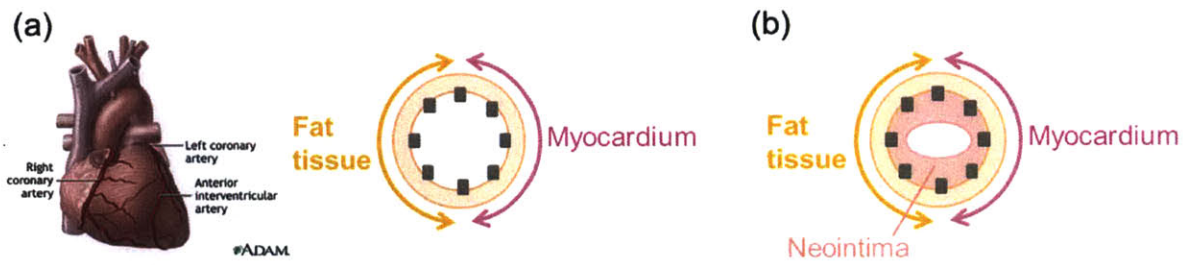

Figure 3-22 Potential causes of stent deformation over time

(a) Since the coronary artery is located between the myocardium and fat tissue layers and since the mechanical resistance to stent expansion and creep of each layer are different, higher pressure is applied from the myocardium layer compared to the fat tissue layer. Since the stent is apposed to the coronary artery wall, the pressure from the myocardium and the fat tissue may deform the stent and the pressure difference between these layers may affect the stent deformation shape.

(b) Neointima formation may also induce stent deformation because the neointima may exert the force that pushes the stent from inside to outside. Since the neointima is usually formed eccentrically, the pressure from the neointima on the stent may also be unequally distributed.

To evaluate the stent deformation over time, stent area A and eccentricity ε were evaluated at three time-points (post-implantation, 5-day follow-up, and 28-day follow-up) for each stented vessel. The frames in which at least one stent-strut was detected in each quadrant were selected.

In each selected OCT frame, the detected stent-struts were fitted as an oval and the lengths of the semi-major axis a_{major} and the semi-minor axis a_{minor} were measured. The stent area A and the eccentricity ε were calculated with Equation 3-6 and 3-7, respectively.

$$A = \pi \times a_{major} \times a_{minor} \tag{3-6}$$

$$\varepsilon = \sqrt{1 - \left(\frac{a_{minor}}{a_{major}}\right)^2} \tag{3-7}$$

when the two axes are equal, ε = 0, designating a circle; when the minor axis approaches the limit of negligibility, ε approaches 1, and the oval closely represents a line. For each vessel, the stent area and the eccentricity were averaged over the entire stented segment. After averaging all the twelve vessels' data, it was found that the stent area decreased slightly at 28-day follow-up and that the eccentricity tended to increase over time (Figure 3-23). No statistically significant differences were observed between any time-points for both the stent area and the eccentricity. In addition, no correlations were observed between the stent area and the eccentricity at any time-points (Figure 3-24) or between the stent area change and the eccentricity change from post-implantation to 5-day or 28-day follow-up (Figure 3-25). From this result, it can be concluded that the stent area remains same although the stent shape is changed over time, i.e., the eccentricity is changed. Thus, for further analysis, the eccentricity was selected as the parameter for the stent deformation.

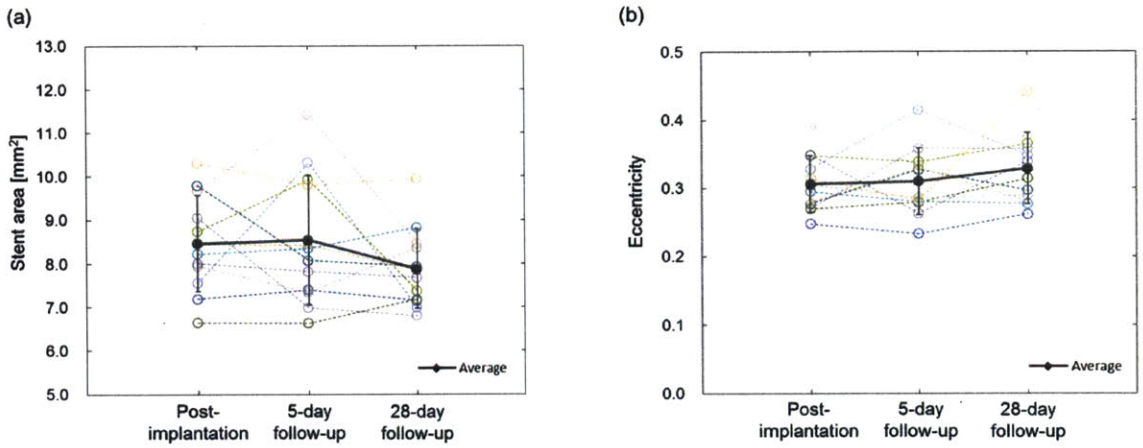

Figure 3-23 Stent deformation analysis: (a) Stent area and (b) eccentricity

The stent area slightly decreased at 28-day follow-up **(a)**. The eccentricity tends to increase over time **(b)**. No statistically significant differences were observed between any time-points for both the stent area and the eccentricity.

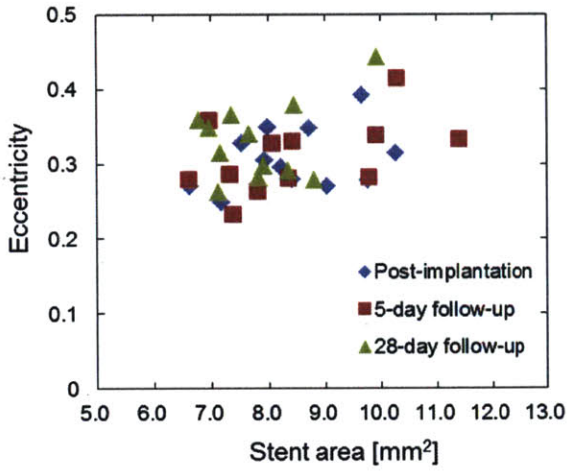

Figure 3-24 Relationship between stent area and eccentricity

No correlation was observed between the stent area and the eccentricity at all time-points (R^2 = 0.12 and p = 0.2 for post-implantation, R^2 = 0.23 and p = 0.12 for 5-day follow-up, and R^2 = 0.17 and p = 0.26 for 28-day follow-up).

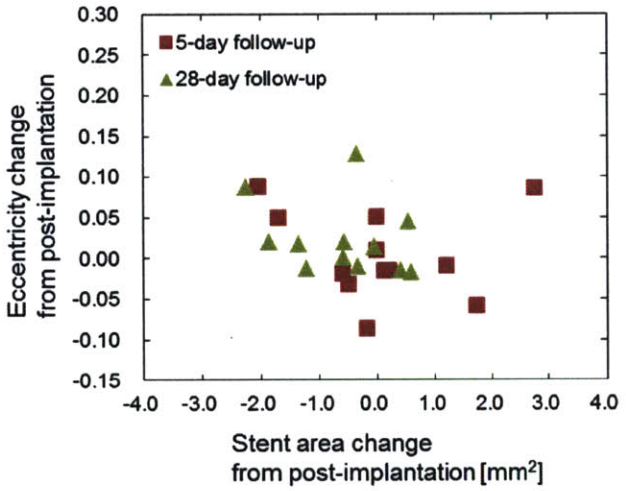

Figure 3-25 Relationship between stent area change and eccentricity change

No correlation was observed between the stent area change from post-implantation and the eccentricity change from post-implantation at both follow-ups (R^2 = 0.018 and p = 0.68 for 5-day follow-up, and R^2 = 0.077 and p = 0.38 for 28-day follow-up).

Since the eccentricity change is not correlated with the stent area change, the geometrical cause of the eccentricity change was explored by evaluating the change of the semi-major axis length and the semi-minor axis length change over time. At each time-point, the semi-major axis length and the semi-minor axis change were averaged over the entire stented segment. Then, the changes of the lengths were calculated by comparing between post-implantation and 5-day or 28-day follow-up. As shown in Figure 3-26, both the semi-major axis length and the semi-minor axis length decreased as the eccentricity increased. The decreased rate of the semi-minor axis length is larger than that of the semi-major axis length (p = 0.0075 for 5-day follow-up, and p = 0.15 for 28-day follow-up); and thus, the eccentricity increases.

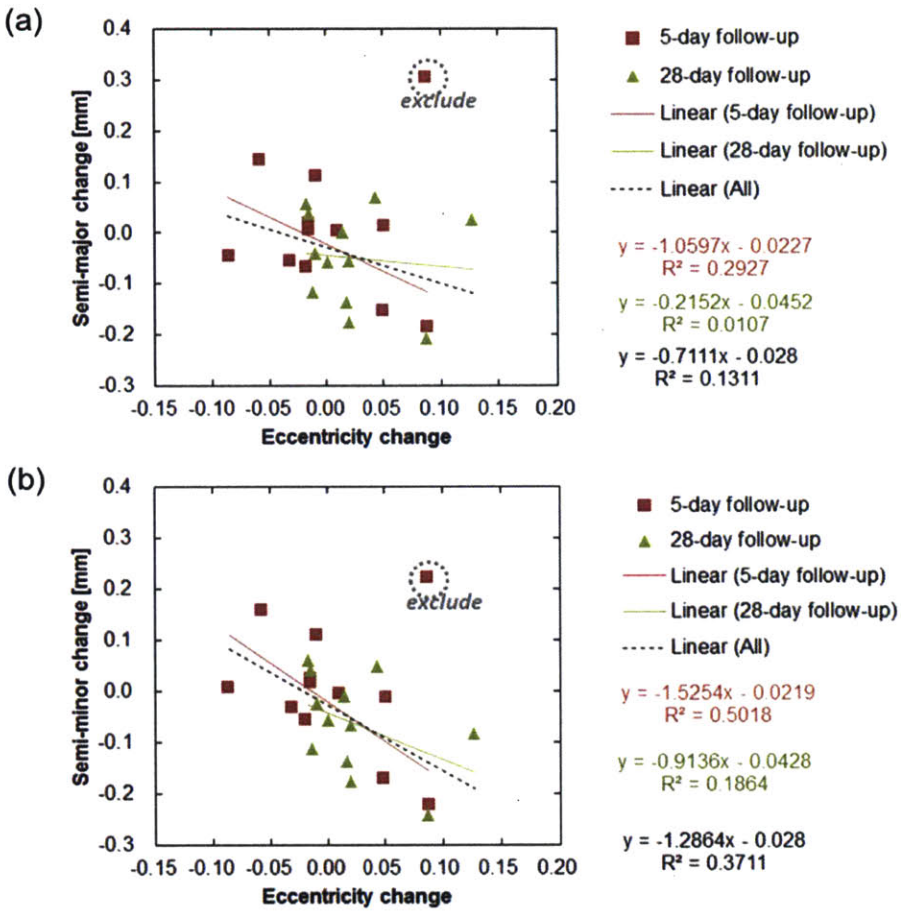

Figure 3-26 Relationship between eccentricity change and semi-major axis length change (a) and semi-minor axis length change (b)

As the eccentricity increases at follow-ups from post-implantation, both the semi-major axis length and the semi-minor axis length decrease. The decreased rate is bigger in the semi-minor axis length than in the semi-major axis length (p = 0.0075 for 5-day follow-up, p = 0.15 for 28-day follow-up); that is the reason why the eccentricity increases at follow-ups. In addition, the slopes of both relationships are steeper at 5-day follow-up than at 28-day follow-up, suggesting that this is an ongoing process.

The liner regression model was obtained by robust estimation. From all the data points, an outlier(s) was manually selected. The residual data points, i.e., the inliers, modeled as a least square regressin line and the distance between this line and each data point was measured, If the distance (s) between the line and the manually selected outlier(s) was out of the four standard deviation of the distances between the line and the inliers, the outlier(s) was confirmed as an outlier(s). If not, the least square regression line was re-calculated from the data points that included the point(s) that was newly categorized as an inlier(s).

To understand the physiological cause of the eccentricity change over time, the effect of the tissue orientation, i.e., the orientation of the myocardium and the fat tissue relative to the coronary artery, on the eccentricity was first evaluated. From the OCT images of the stented segment for all twelve vessels, the frames that satisfied all the following criteria were selected: (i) the stent is fully apposed to the vessel wall, (ii) the myocardium and the fat tissue can be clearly distinguished, and (iii) the similar cross-sectional planes can be found in all three time-points. For criteria (iii), the number and the location of stent-struts and/or the side branch in the OCT frame were used to find the similar cross-sectional planes. In all OCT frames, the location of the guidewire was corrected by rotating the frame rigidly around the center of the image so that the guidewire was always located under the imaging catheter. Eight to ten frames/time-point were selected for each vessel of the fully-apposed cases (six vessels), and three to five frames/time-point were selected for each vessel of the underexpanded cases (six vessels). After selecting the OCT frames, a line defining the axis that separated the myocardium and the fat tissue was set manually. In OCT image, the myocardium is characterized by the presence of more homogeneous backscattering and the presence of small vessels (side branches from the main coronary arteries), while the fat tissue was characterized as having highly reflecting dots that are relatively evenly space, which represent the reflectance from the top and the bottom of large adipocytes. The distinction between the myocardium and the fat tissue was performed under the supervision of an experienced pathologist and OCT reader (Dr. Guillermo Tearney). Then, in each OCT frame, the angle of the boundary between the myocardium and the fat tissue from the y-axis φ and the angle of the fitted oval's major axis from the y-axis ψ were measured (Figure 3-27).

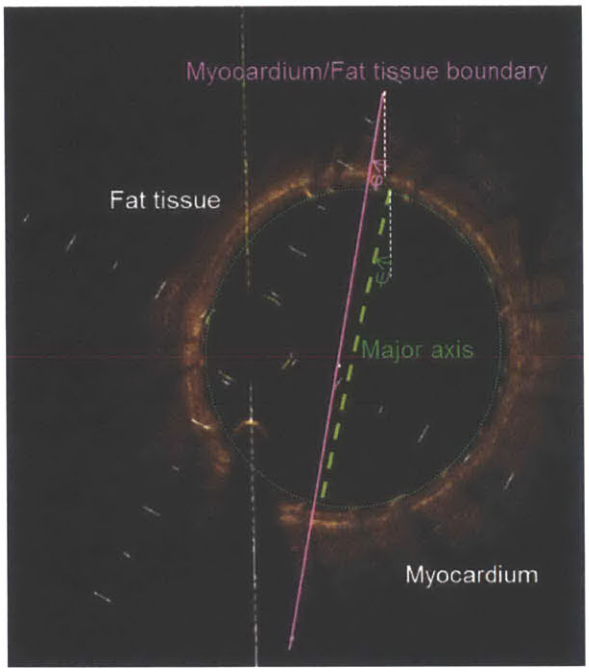

Figure 3-27 Myocardium and fat tissue distinction in the OCT image and definition of myocardium/fat tissue boundary angle φ and the major axis angle ψ

In the OCT image, the myocardium shows a layered structure, while the fat tissue shows a dotted texture. This difference is used to distinguish between the myocardium and the fat tissue.

The angle of the myocardium/fat tissue boundary φ and the angle of the major axis ψ are measured from y-axis.

Strong 1:1 linear relationships between the myocardium/fat tissue boundary angle and the major axis angle were observed for each time-point and for all time-points (Figure 3-28). These relationships at follow-ups were independent of the relationship at post-implantation (Figure 3-29). These results suggest that the stent is deformed due to an unequal pressure distribution that is created by the orientation of the myocardium and the fat tissue. One plausible explanation for this finding is that the myocardium is more rigid than the fat tissue. Therefore, the side that is close to the myocardium is more compressed or less expanded over time. As a result, the stent becomes an oval whose the major axis is parallel to the boundary of the myocardium and the fat tissue. In addition, because this strong 1:1 linear relationship was observed at 28-day follow-up when the neointima was significantly formed inside the stent area, it suggests that this unequal pressure distribution due to the tissue orientation is the primary factor that governs the stent deformation in the healthy artery despite the existence of the significant vascular responses to stent implantation.

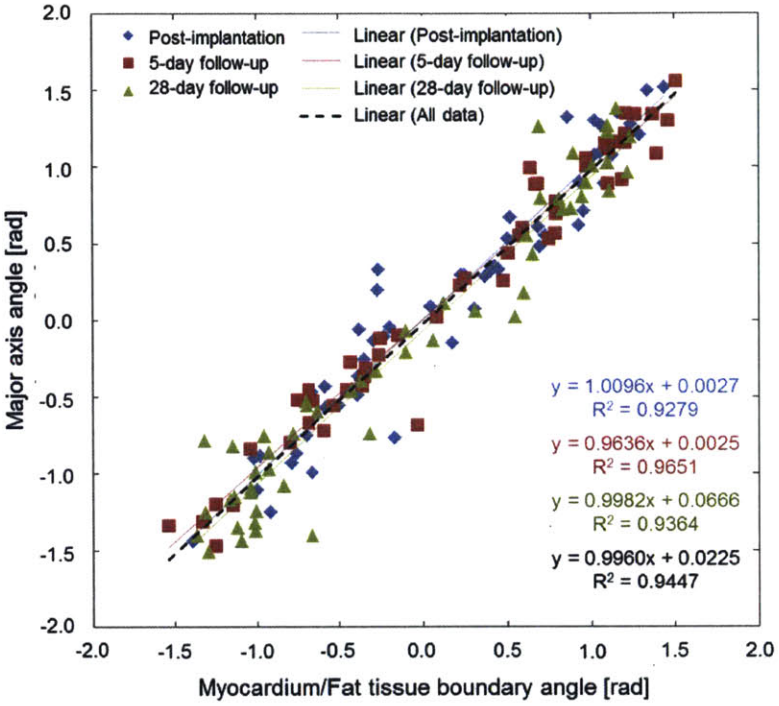

Figure 3-28 Relationship between the myocardium/fat tissue boundary angle and major axis angle

Strong 1:1 linear relationships between the myocardium/fat tissue boundary angle and major axis angle are observed at each time-point and for all time-points. This result suggests that the orientation of the myocardium and the fat tissue induces the stent deformation.

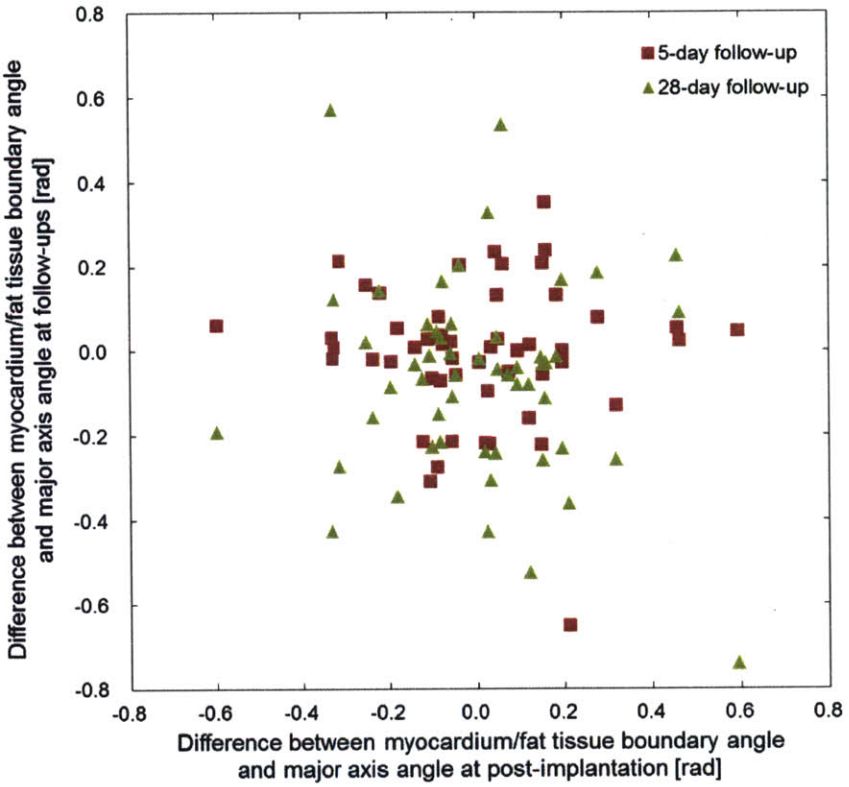

Figure 3-29 Comparison of the angle difference between the myocardium/fat tissue boundary and the major axis at post-implantation to that at follow-ups

No correlation was observed between post-implantation and follow-ups. This result suggests that the strong linear relationships that were observed in Figure 3-27 are independent of time-points.

The effect of the vascular responses was evaluated to understand another physiological, potentially pathological, cause of the eccentricity change over time. Since no significant neointima formation was observed at 5-day follow-up for all stented vessels, the effect of the vascular responses was evaluated by comparing 5-day follow-up and 28-day follow-up. The absolute change of the eccentricity from post-implantation to 5-day follow-up was 0.043 ± 0.031 and that from post-implantation to 28-day follow-up was 0.032 ± 0.037. Although no statistically significant difference was observed between 5-day and 28-day follow-up, the average of the absolute eccentricity change was smaller at 28-day follow-up than at 5-day follow-up. In addition,

as shown in Figure 3-26, the slopes of the relationship between the eccentricity change and the semi-major axis length change or the semi-minor axis length change were steeper when post-implantation and 5-day follow-up were compared than those when post-implantation and 28-day follow-up were compared. These result suggests that the stent started to return to a circular shape from 5-day to 28-day follow-ups because of the neointima formation that exerted opposing forces to those from the myocardium/fat tissue orientation.. This effect is considered smaller than the one due to the orientation of the myocardium and the fat tissue (25% based on the average of the absolute eccentricity change: the difference in the absolute eccentricity change between 5-day follow-up and 28-day follow-up relative to the absolute eccentricity change at 5-day follow-up), as discussed in the previous paragraph.

As shown in Figure 3-23(b), the eccentricity changes over time differently in each vessel. Since the time-point registration method uses the vessel centerline and the stent centroid geometry as registration paths, this eccentricity change over time may cause the error of the time-point registration. To understand this relationship, the vessel centerline shift in the stented segment was evaluated and correlated with the eccentricity change. The vessel centerline shift from post-implantation to 5-day or 28-day follow-up was measured in the stented segment with its direction, i.e., toward myocardium or toward fat tissue. The geometrical location of the myocardium relative to the vessel centerline in the stented segment was determined using the side branch location relative to the stented segment from the angiographic images. The measured vessel centerline shift was averaged over the stented segment.

Figure 3-30 shows the relationship between the vessel centerline shift and the eccentricity change. The eccentricity increased as the vessel centerline shift toward the myocardium increased. Since the stent was continuously pushed from the myocardium side due to cardiac motion, the stent became more oval over time, as discussed above. However, because coronary arteries are connected to the myocardium, the vessel centerline became closer to the myocardium when the stent became more oval. In addition, the slope was steeper at 5-day

follow-up than at 28-day follow-up (p = 0.036). This suggests the possibility that neointima exerts opposing mechanical forces that pushes the stent from inside to outside, which leads to a slight recovery of the stent shape to circular at 28-day follow-up.

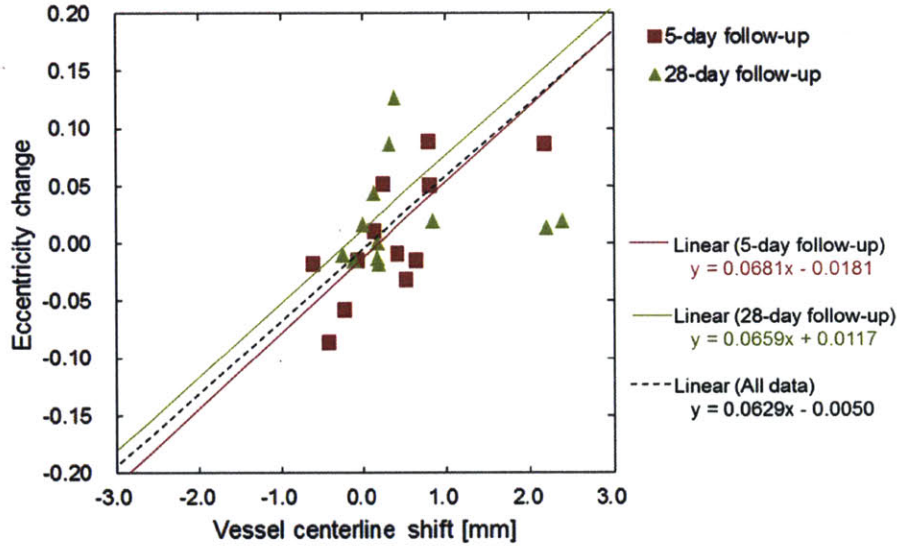

Figure 3-30 Relationship between the vessel centerline shift and eccentricity change from post-implantation

If the vessel centerline shifts toward the myocardium at follow-ups from post-implantation, the vessel centerline shift shows as a positive value.

The eccentricity increases as the vessel centerline shift toward the myocardium increases. Since the stent is pushed continuously from the myocardium side and since the coronary artery is connected to the myocardium, the vessel centerline, i.e., lumen centroid, moves toward the myocardium when the stent shape becomes more oval. The steeper slope is observed at 5-day follow-up compared to 28-day follow-up, which reflect the influence of the neointima at 28-day follow-up.

3.4.3.3 Vessel Centerline Shift and Stent-strut Shift

In 3.4.3.2, the stent deformation, i.e., the eccentricity change, over time was correlated with the vessel centerline shift. Since this stent deformation is considered to induce the error in time-point registration, the stent-strut shift should correlate with the vessel centerline shift. Figure 3-31 shows the relationship between the vessel centerline shift and the stent-strut shift from

post-implantation to follow-ups. Both shifts were measured with their direction: the positive value represents the direction toward the myocardium and the negative value represents the direction toward the fat tissue. A linear correlation was observed at both follow-ups (R^2 = 0.62 for 5-day follow-up and R^2 = 0.58 for 28-day follow-up). This result supports the hypothesis that the error of the time-point registration is induced by the stent deformation, which leads to the vessel centerline shift over time. In addition, the fact that both slopes are less than 1 is considered to reflect the eccentric stent deformation over time. As discussed in 3.4.3.2, when the vessel centerline shifts toward the myocardium, the stent shape becomes more oval. Thus, the magnitude of stent-strut shift varies in the angular direction on each cross-sectional plane: the bigger magnitude would be observed near the semi-minor axis, while the smaller magnitude would be observed near the semi-major axis, which is consistent with the results in Figure 3-26.

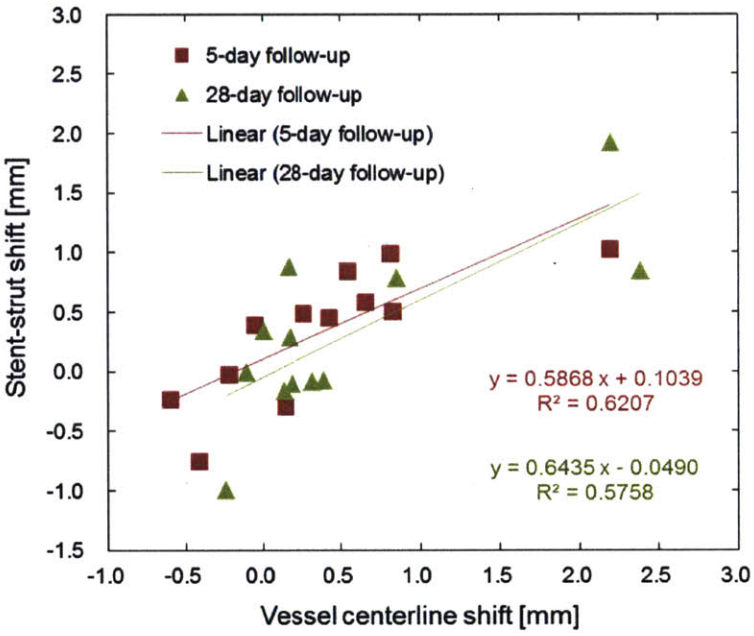

Figure 3-31 Relationship between the vessel centerline shift and the stent-strut shift
The stent-strut shift is linearly correlated with the vessel centerline shift at both follow-ups. This result supports that the error of the time-point registration method is induced by the vessel centerline shift due to the stent deformation over time. The fact that both slopes are less than 1 reflects the eccentric stent deformation (a shape change from a circle to an oval).

3.4.4 Preliminary Data: Underlying Mechanism of Vascular Responses

To understand the influence of the underexpansion on the chronic vascular responses, the stent-cell level analysis was performed. Since the error in time-point registration was 1.6 mm ± 0.5 mm and since the stent-cell length was 1.7 mm, this analysis was performed by grouping every two stent-cells. This grouping was achieved by measuring the length of the vessel centerline from the edge of the stent. In each OCT frame, the wall-to-stent distance was evaluated by averaging the distances between the lumen surface and each detected stent-strut. This distance is positive if the stent-strut is located inside the lumen. Then, all the evaluated wall-to-stent distances from the OCT frames that were within every each two stent-cells were averaged. The stent-cells were numbered from 1 to 10 in the direction of proximal to distal.

All the underexpansions were resolved at 5-day follow-up due to the acute vascular recoil by the smooth muscle cells in the arterial wall (Figure 3-32). A significant amount of the neointima was formed at 28-day follow-up, while no neointima was formed at 5-day follow-up for all twelve stented vessels (both fully-apposed cases and underexpanded cases) (Figure 3-32). More neointima was formed in the underexpanded cases compared to the fully-apposed cases for all the groups (Figure 3-33). In addition, the most neointima was formed at the distal regions to the area where the underexpansion was created (stent-cells #7&#8 and #9&#10) (Figure 3-33). This finding is consist with the well-known mechanism of the vascular response: the blood flow disruption due to stent implantation itself and/or underexpansion of stent induces the variation of the wall shear stress in the stented artery, resulting in more formation of the neointima on the chronic phase (1.2.4) [5, 15-17].

As discussed in 3.4.3.2, the stent deformed over time mainly because of the tissue orientation of the myocardium and the fat tissue. As shown in Figure 3-31, the underexpansion was resolved at 5-day follow-up, and the range of the eccentricity change was not different between the fully-apposed cases and the underexpanded cases (Figure 3-34, *x*-axis), which also

supports the hypothesis that the stent deformation is mainly induced by the continuous pressure only from the myocardium side. To understand the effect of the stent deformation on the vascular responses, i.e., the neointima formation on the chronic phase, the relationship between the eccentricity change from post-implantation to 5-day follow-up and the wall-to-stent distance at 28-day follow-up was evaluated. No significant relationship was observed in the fully-apposed cases (Figure 3-34(a)). Neither were significant differences between each stent-cell group observed (Figure 3-34(a)). In contrast, in the underexpanded cases, the linear relationships were observed between the eccentricity change and the wall-to-stent distance for all stent-cell groups (Figure 3-34(b)). In addition, the slope became steeper in the stent-cell groups where the underexpansion was achieved at post-implantation (stent-cell #5&#6) and where the area was distal to the underexpansion (stent-cell #7&#8 and #9&#10) (Table 3-10). This result suggests that eccentricity change on the acute phase (from post-implantation to 5-day follow-up) might be another factor that determines the degree of the vascular responses, i.e., the amount of the neointima on the chronic phase, only in the underexpansion cases.

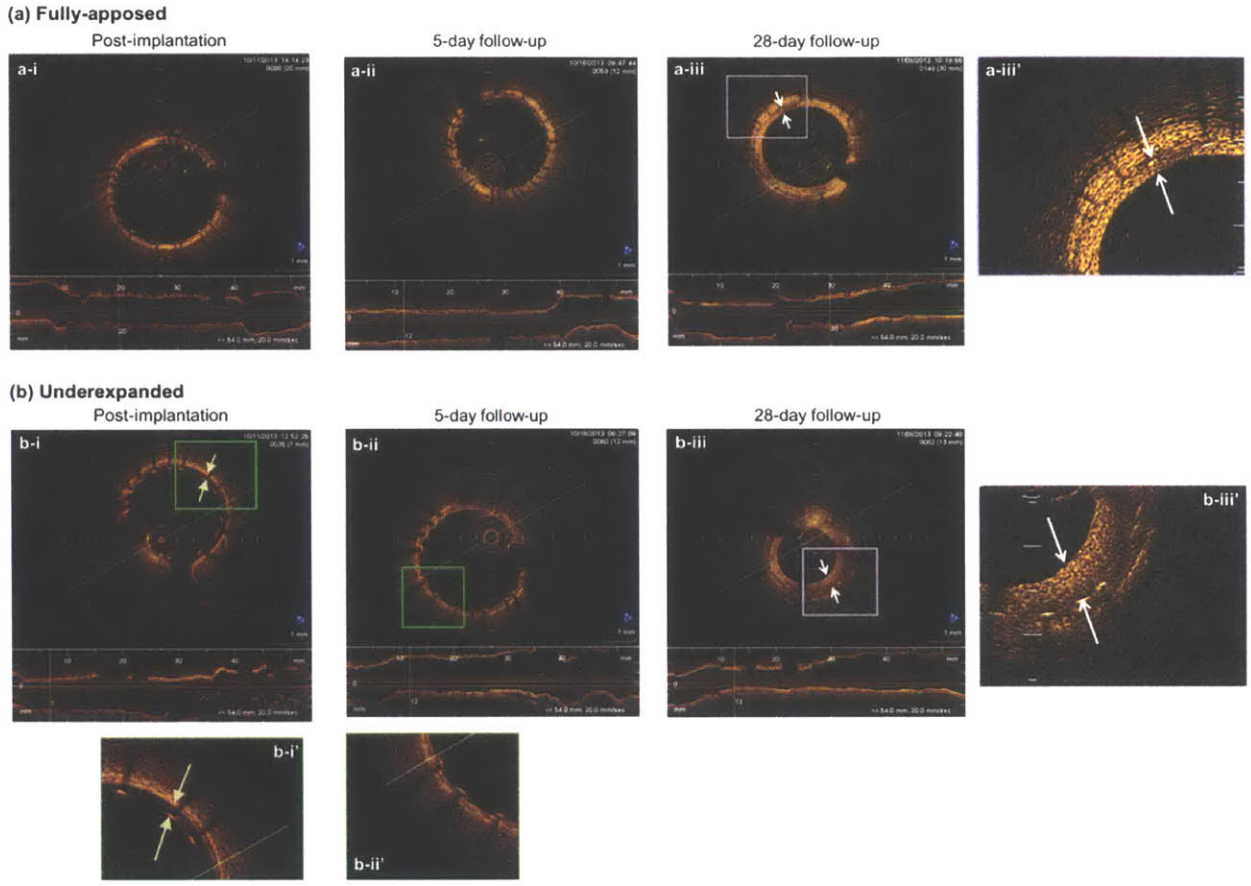

Figure 3-32 Time-course images of cross-sectional plane in the middle of the stented region with OCT: (a) Fully-apposed case and (b) underexpanded case

For all the underexpanded cases, the distance between the stent-strut and the lumen surface was observed at post-implantation **(b-i, b-i')**, but no distance was observed at 5-day follow-up due to the vessel recoil **(b-ii, b-ii')**.

For all cases, no neointima was formed at 5-day follow-up **(a-ii, b-ii)**, while the significant neointima responses were observed at 28-day follow-up **(a-iii, a-iii', b-iii, b-iii')**.

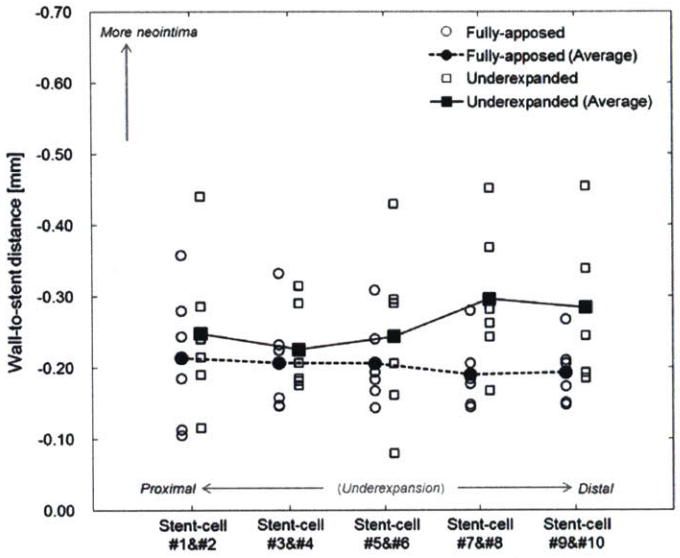

Figure 3-33 Wall-to-stent distance at 28-day follow-up for each stent-cell group

More neointima was formed in the underexpanded cases than in the fully-apposed cases. In the underexpanded cases, more neointima was observed in the distal regions of the area where the underexpansion was originally created.

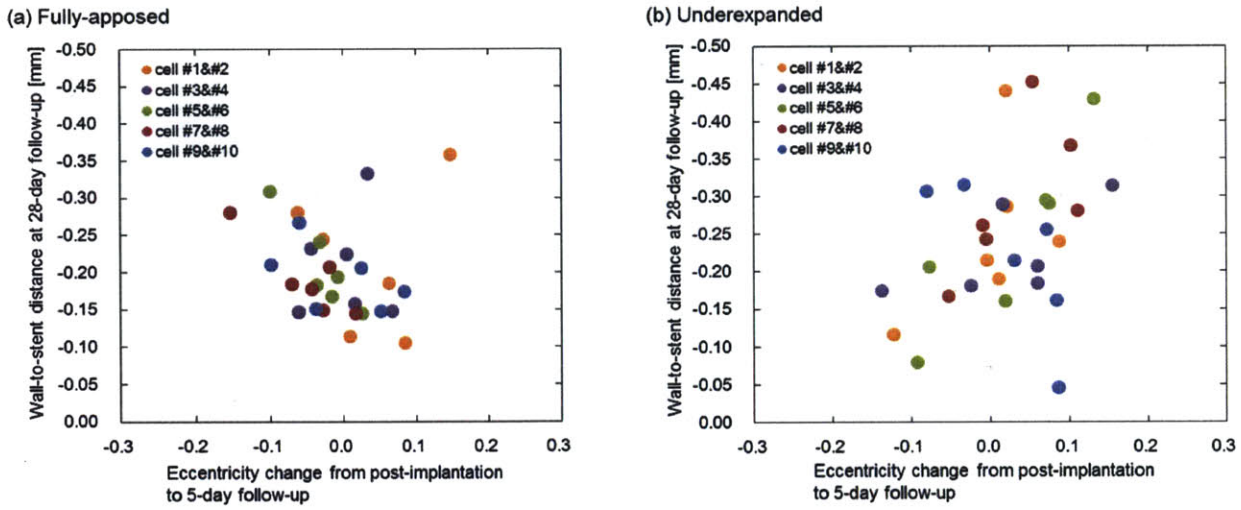

Figure 3-34 Relationship between the wall-to-stent distance at 28-day follow-up and the eccentricity change from post-implantation to 5-day follow-up

In the underexpanded cases, the wall-to-stent distance at 28-day follow-up was linearly correlated with the eccentricity change for all the stent-cell groups **(b)**.

Table 3-10 Linear regression lines for the relationship between the neointima thickness and the eccentricity change in the underexpanded cases (Figure 3-33(b))

Stent-cell group	Linear regression line
Stent-cell #1 & #2	$y = -0.8347\,x - 0.2458$ ($R^2 = 0.27$)
Stent-cell #3 & #4	$y = -0.4007\,x - 0.2167$ ($R^2 = 0.42$)
Stent-cell #5 & #6	$y = -1.1978\,x - 0.2182$ ($R^2 = 0.77$)
Stent-cell #7 & #8	$y = -0.9835\,x - 0.2628$ ($R^2 = 0.42$)
Stent-cell #9 & #10	$y = -1.1383\,x - 0.2527$ ($R^2 = 0.60$)

3.4.5 Significances of Newly Developed Methods

3.4.5.1 Vessel Centerline Reconstruction Method

This newly developed vessel centerline reconstruction method is significant because: (i) it can handle both non-isocentric and non-orthogonal paired angiographic images (3.4.1), (ii) it has high reproducibility across various imaging angle differences (20^{o}-130^{o}) and between different cardiac cycles, specifically in the stented segment (3.4.1.4 and 3.4.1.5), (iii) it is robust to the cardiac motion (3.4.1.4 and 3.4.1.5), and (iv) it can estimate accurately the total isocenter movement in each image (3.4.1.1. All of these advantages suggest that this new method will be applicable in the clinical setting. As discussed in 2.4.4, most of the state-of-the-art methods have not been validated for the non-isocentric and/or non-orthogonal paired angiographic images. Tu et al.'s method [14] can handle the non-orthogonal pair if the imaging angle difference is at least 25^{0}, while this method can handle the paired images with at least 20^{0} of imaging angle difference. Yang et al.'s method [11] can handle the non-isocentric images, but it cannot estimate the total isocenter movement in each image, while this method can. In addition, none of the currently available methods have evaluated their reproducibility between different cardiac cycles although the paired angiographic images are acquired at the different timings when the monoplane angiography system is used. Neither has the influence of the cardiac motion on these methods been evaluated.

The accuracy of this new method is comparable to that of the state-of-the-art method. This method yielded a vessel centerline in the stented segment similar to that yielded by the currently available method [6] with the root mean square error between two vessel centerlines similar to that with Yang et al.'s method [11] (3.4.1.3).

3.4.5.2 Structural Reconstruction Method

Although many structural reconstruction methods by angiography-OCT fusion have been proposed [2, 3, 14, 18-20], the effect of the cardiac motion on these methods has not been evaluated; and thus, the structural reconstruction by angiography-OCT fusion has not been optimized. The cardiac motion changes the morphology of the coronary artery itself, which may affect the morphology of the vessel centerline. It also induces the lateral and the longitudinal movement of the OCT imaging catheter. The lateral movement problem can be overcome by using the vessel centerline as a fusion path [3]; however, the longitudinal movement problem has not been addressed. The longitudinal movement of the imaging catheter may affect the OCT inter-frame distance, which leads to the error in fusing the OCT images on the vessel centerline that is reconstructed from paired angiographic images.

This newly developed structural reconstruction method is significant because: (i) the cardiac phase at which the vessel centerline is reconstructed was determined by evaluating its deformation over a cardiac cycle (3.4.2.1), and (ii) the problem due to the longitudinal movement of the OCT imaging catheter was overcome by estimating the OCT inter-frame distance based on *a priori* knowledge of the stent design and the physiological information, i.e., the recorded heart rate (3.4.2.3). The error of the reconstructed stent length relative to the actual stent length was approximately 2-3% and it was improved by approximately 2-fold by using the estimated OCT inter-frame distance. In addition, the potential error in the structural reconstruction from the vessel centerline reconstruction was estimated as 2-3%, which suggests that the error of the reconstructed stent length is primarily induced by the error in the vessel centerline reconstruction. This error in vessel centerline reconstruction cannot be improved because it is similar to the resolution of the angiographic images, i.e., 1 pixel, as shown as the value of distance between Landmarks 1 in Table 3-6. Moreover, this method is superior to the state-of-the-art methods since the difference of the reconstructed stent length between time-points was improved approximately 2-fold by estimating the OCT inter-frame distance.

3.4.5.3 Time-point Registration Method

The underlying mechanism of the vascular responses to stent implantation cannot be fully understood unless the vascular responses can be tracked in 3D on the stent-strut level. The newly developed method enables comparing the different time-point data in 3D by registering the accurately reconstructed structures from different time-points via a vessel centerline and a stent centroid geometry. In addition, it allows using all the images, unlike Gutierrez-Chico et al.'s method that the OCT images that contain the same side branch across time only are used [4]. However, the analysis on the stent-strut level has not been achieved yet due to the stent deformation over time (3.4.3.2). This stent deformation is primarily induced by the tissue orientation of the myocardium and the fat tissue that surrounds the coronary artery. Since the degree of the stent deformation was correlated with the vessel centerline shift, there is a possibility to achieve the stent-strut level analysis by correcting the vessel centerline shift across time.

References

1. Jang, I.-K., *Optical Coherence Tomography or Intravascular Ultrasound?* JACC: Cardiovascular Interventions, 2011. **4**(5): p. 492-494.
2. Athanasiou, L.S., et al. *3D Reconstruction of Coronary Arteries using Frequency Domain Optical Coherence Tomography Images and Biplane Angiography.* in *34th Annual International Conference of the IEEE Engineering-in-Medicine-and-Biology-Society (EMBS)*. 2012. San Diego, CA.
3. Papafaklis, M.I., et al., *Anatomically correct three-dimensional coronary artery reconstruction using frequency domain optical coherence tomographic and angiographic data: head-to-head comparison with intravascular ultrasound for endothelial shear stress assessment in humans.* . EuroIntervention, 2014(1969-6213 (Electronic)).
4. Gutierrez-Chico, J.L., et al., *Vascular Tissue Reaction to Acute Malapposition in Human Coronary Arteries Sequential Assessment With Optical Coherence Tomography.* Circulation-Cardiovascular Interventions, 2012. **5**(1): p. 20-U81.
5. Stone, P.H., et al., *Prediction of progression of coronary artery disease and clinical outcomes using vascular profiling of endothelial shear stress and arterial plaque characteristics: the PREDICTION Study.* Circulation, 2012. **126**(2): p. 172-81.
6. Bourantas, C.V., et al., *A new methodology for accurate 3-dimensional coronary artery reconstruction using routine intravascular ultrasound and angiographic data: implications for widespread assessment of endothelial shear stress in humans.* EuroIntervention, 2013. **9**(5): p. 582-593.
7. Arts, T., et al., *Mapping Displacement and Deformation of the Heart With Local Sine-Wave Modeling.* Ieee Transactions on Medical Imaging, 2010. **29**(5): p. 1114-1123.
8. Dimitris N. and Metaxas, L.A., *Functional Imaging and Modeling of the Heart*. 2011: Springer.
9. Wahle, A., et al., *Geometrically correct 3-D reconstruction of intravascular ultrasound images by fusion with biplane angiography-methods and validation.* IEEE Transactions on Medical Imaging, 1999. **18**(8): p. 686-699.
10. Myronenko, A. and S. Xubo, *Point Set Registration: Coherent Point Drift.* Pattern Analysis and Machine Intelligence, IEEE Transactions on, 2010. **32**(12): p. 2262-2275.
11. Yang, J., et al., *Novel approach for 3-d reconstruction of coronary arteries from two uncalibrated angiographic images.* IEEE Trans Image Process, 2009. **18**(7): p. 1563-72.
12. Ramanathan, T. and H. Skinner, *Coronary blood flow.* Continuing Education in Anaesthesia, Critical Care & Pain, 2005. **5**(2): p. 61-64.
13. Kaazempur-Mofrad, M.R. and C.R. Ethier, *Mass Transport in an Anatomically Realistic Human Right Coronary Artery.* Annals of Biomedical Engineering, 2001. **29**(2): p. 121-127.

14. Tu, S., et al., *Fusion of 3D QCA and IVUS/OCT.* Int J Cardiovasc Imaging, 2011. **27**(2): p. 197-207.
15. Chen, H.Y., et al., *Impact of stent mis-sizing and mis-positioning on coronary fluid wall shear and intramural stress.* Journal of Applied Physiology, 2013. **115**(2): p. 285-292.
16. Stone, P.H., et al., *Effect of endothelial shear stress on the progression of coronary artery disease, vascular remodeling, and in-stent restenosis in humans: in vivo 6-month follow-up study.* Circulation, 2003. **108**(4): p. 438-44.
17. Rikhtegar, F., et al., *Compound Ex Vivo and In Silico Method for Hemodynamic Analysis of Stented Arteries.* Plos One, 2013. **8**(3).
18. Hebsgaard, L., et al., *Co-registration of optical coherence tomography and X-ray angiography in percutaneous coronary intervention. The Does Optical Coherence Tomography Optimize Revascularization (DOCTOR) fusion study.* Int J Cardiol, 2015. **182**(0): p. 272-278.
19. Tu, S., et al., *In Vivo Flow Simulation at Coronary Bifurcation Reconstructed by Fusion of 3-Dimensional X-ray Angiography and Optical Coherence Tomography.* Circulation: Cardiovascular Interventions, 2013. **6**(2): p. e15-e17.
20. Tu, S.X., et al., *In vivo comparison of arterial lumen dimensions assessed by co-registered three-dimensional (3D) quantitative coronary angiography, intravascular ultrasound and optical coherence tomography.* International Journal of Cardiovascular Imaging, 2012. **28**(6): p. 1315-1327.

CHAPTER 4:

VALIDATION OF STRUCTURAL RECONSTRUCTION AND TIME-POINT REGISTRATION IN A CLINICAL SETTING

4.1 Abstract

In the actual clinical setting, the patients who undergo catheter intervention, especially stent implantation, have occlusions in the coronary arteries due to atherosclerotic plaques. The presence of the underlying disease may affect the accuracy of the newly developed structural reconstruction and time-point registration methods. Although these new methods have been validated in the preclinical setting using *in vivo* swine model, and their accuracy has been shown to be similar or superior to that of the state-of-the-art methods, the precision and the limitations of these methods need to be evaluated in the clinical setting prior to clinical usage.

4.2 Background

In Chapter 3, the vessel centerline reconstruction method was validated and the structural reconstruction and the time-point registration methods were developed with the datasets that consider the controlled isocenter movement and the time changes from seconds (within a cardiac cycle) to days (from post-implantation to follow-up). The newly developed methods have been shown to be robust enough to reconstruct the accurate 3D structures of the lumen and the stent and to register them over time in 3D space when catheter intervention is performed in healthy animal arteries; however, the accuracy and the robustness of these methods may be affected by the existence of disease and the physiological and pathological differences between animals and humans. Moreover, the unknown or unquantifiable clinical imaging environment and the uncontrolled vascular responses to stent implantation may influence the structural reconstruction and the time-point registration methods. The clinical datasets are suitable for validation both the structural reconstruction and the time-point registration methods because these datasets are affected by unknown isocenter movements and uncontrolled vascular responses to stent implantation and clinical outcomes and because the precise procedural information and the pre-interventional information of each patient can be obtained from them using standard operating procedures.

In this chapter, the vessel centerline reconstruction method will be validated through comparing it with the reconstruction from clinically available computed tomography angiography. The structural reconstruction and the time-point registration will be validated using clinical datasets. The accuracy and the robustness of both methods are presented, and their clinical applicability will be discussed.

4.3 Materials and Methods

4.3.1 Clinical Datasets

Two clinical datasets were used: (i) computed tomography angiography images and coronary angiographic images to validate the vessel centerline reconstruction method, and (ii) coronary angiographic images and optical coherence tomography (OCT) images to validate the structural reconstruction and the time-point registration methods. All the clinical datasets were provided by the collaborators from Brazil (Dr. Pedro Lemos, Dr. Augusto Celso de Araujo Lopes Jr, and Dr. Micheli Galon).

4.3.1.1 Images with Computed Tomography Angiography and Coronary Angiography

The images from eighteen patients were obtained with computed tomography angiography and coronary angiography. All the images were acquired before stent implantation.

All the computed tomography angiography images were acquired with Aquilion Prime or Aquilion One (Toshiba Medical Systems, Japan) and saved in the DICOM format. The in-plane resolution was 0.39 mm/pixel and the lateral resolution was 0.5 mm. All the coronary angiographic images were acquired with Allura Xper (Philips Medical Systems, Netherland) and saved in the DICOM format. The in-plane resolution was 0.26 mm/pixel and the frame rate was 15 frames/s.

4.3.1.2 Images with Coronary Angiography and OCT

The images from nineteen stented coronary arteries from seventeen patients were obtained with coronary angiography and OCT. Only one type of stent, sirolimus-eluting stent (Inspiron, SCITECH, Brazil), was used. For each vessel, several coronary angiographic images were acquired before the procedure. Based on these images, the sizes of the balloon catheter and the stent (diameter: 2.5 mm, 3.0 mm, 3.5 mm; length: 13 mm, 16 mm, 19 mm, 23 mm, 29 mm) were determined. Then, the stent was implanted with nominal pressure (10 atm). After that, in-stent post-dilation was performed with a non-compliant balloon of the same diameter with

inflation pressure of 14-16 atm. Additional post-dilation was performed with the higher inflation pressure if needed. Angiographic images from at least two viewpoints and OCT images were acquired after each balloon inflation. All inflations were maintained for 30 seconds to ensure pressure equalization. The follow-up images were acquired 18-26 months later using coronary angiography and OCT.

All the coronary angiographic images were acquired with Allura Xper (Philips Medical Systems, Netherland) and saved in the DICOM format. The in-plane resolution was 0.26 mm/pixel and the frame rate was 15 frames/s or 30 frames/s. The image acquisition settings, including the orientation of the angiography system and frame rates, were saved in the DICOM headers of the corresponding DICOM file. All the OCT images were acquired with C7-XR OCT Intravascular Imaging System (St. Jude Medical, St. Paul, MN) and saved in the OCT format. The pullback speed of the OCT was 20 mm/s and the images were taken every 200 μm.

4.3.2 Validation: Vessel Centerline Reconstruction Method

From the data of eighteen patients, five vessels (one left main artery, two left anterior descending arteries, and two left circumflex arteries) from three patients were selected based on the available frame number in the computed tomography angiography run. The selected vessels had more than 400 frames of the computed tomography angiography, which is adequate for reconstructing the structures of coronary arteries in 3D.

4.3.2.1 Reconstruction from Computed Tomography Angiography Images

The selected coronary arteries were reconstructed from the computed tomography angiography images with ScanIP (Simpleware Ltd., United Kingdom). First, the images were segmented to extract the coronary arteries and the neighboring tissue in each frame. Then, the extracted structures were interpolated in the longitudinal direction (proximal to distal direction). After that, the neighboring tissue was deleted manually and the surface of the coronary arteries

was smoothed by applying a Gaussian smoothing filter. Finally, the vessel centerline was extracted by skeletonizing the surface structure of the coronary arteries.

4.3.2.2 Reconstruction from Coronary Angiographic Images

The vessel centerline of the same vessel was reconstructed with the newly developed vessel centerline reconstruction method. The detailed explanation for all the steps of this method is available in 3.3.4.

4.3.2.3 Comparison of Reconstructed Vessel Centerline Length

To evaluate the accuracy of the newly developed method, the length of the reconstructed vessel centerline between two side branches was compared between two methods: the newly developed coronary angiography-based method (4.3.2.2) and the clinically available computed tomography angiography-based method (4.3.2.1).

4.3.2.4 Reproducibility between Different Cardiac Cycles

To understand the clinical reproducibility of the vessel centerline reconstruction between different cardiac cycles, the vessel centerlines were reconstructed from two different end-diastolic phase images with the newly developed method. The reconstructed vessel centerlines were registered with the algorithm that is explained in Figure 3-4. The reproducibility was evaluated in terms of (i) error of stented segment length between two side branches, (ii) distance between Landmarks 1, (iii) distance between Landmarks 2, and (iv) angle between Landmarks 2. These results were compared to the reproducibility results in the preclinical setting (3.4.1.5).

4.3.3 Validation: Structural Reconstruction Method

From nineteen stented coronary arteries, five stented arteries (one right coronary artery and four left anterior descending arteries) were selected based on the atherosclerotic plaque characteristics for the validation of the structural reconstruction method and the time-point

registration method. To estimate the OCT inter-frame distance with the method that is described in 3.3.6.3(i), the stent needs to be fully expanded and apposed to the vessel wall. To achieve this, the atherosclerotic plaque needs to be soft, i.e., the lipid needs to be rich in the plaque. This selection was made using the pre-interventional OCT images.

4.3.3.1 Deformation of Vessel Centerline over a Cardiac Cycle

To evaluate the influence of the vessel centerline reconstruction on the structural reconstruction method, the deformation of the vessel centerline over a cardiac cycle was first evaluated. For each stented vessel, the vessel centerlines were reconstructed from four different cardiac phases: the end-diastolic phase, the mid-systolic phase, the end-systolic phase, and the mid-diastolic phase. The reconstructed vessel centerlines were registered onto the end-diastolic vessel centerline with the algorithm that is explained in Figure 3-4. The deformation was evaluated in terms of (i) the difference in the stented segment length between two side branches, (ii) distance between Landmarks 1, (iii) distance between Landmarks 2, and (iv) angle between Landmarks 2. These results were compared to the deformation results in the preclinical setting (3.4.2.1).

4.3.3.2 Reconstruction of Lumen and Stent Structures

The structures of the lumen and the stent were reconstructed with the newly developed structural reconstruction method. The detailed explanation of this method is available in 3.3.6. Briefly, the vessel centerline at the end-diastolic phase was first reconstructed from paired angiographic images. Then, the lumen and stent-struts were detected in each OCT frame. Next, the OCT inter-frame distance was corrected. After that, the detected lumen and stent-struts information was transformed from 2D to 3D by perpendicularly placing the information from each OCT frame onto the reconstructed vessel centerline using the corrected OCT inter-frame distance. Finally, the structures of the lumen and the stent were reconstructed by interpolating and smoothing the 2D-to-3D transformed information.

4.3.3.3 Comparison between Actual Stent Length and Reconstructed Stent Length

After reconstructing the structures of the lumen and the stent, the lengths of the stents were evaluated based on the length of the stented segment centerline. All of the measured stent lengths were compared to the actual stent length. This result was compared to that in the preclinical setting (Table 3-7).

4.3.3.4 Comparison of Reconstructed Stent Lengths between Different Time-points

Since the stent length should be the same between different time-points (post-implantation and follow-up), the reconstructed stent lengths were compared between post-implantation and follow-up. This result was compared to that in the preclinical setting (Table 3-8).

4.3.4 Validation: Time-point Registration Method

4.3.4.1 Registration of Reconstructed Structures across Time

First, the reconstructed structures of the lumen and stent at follow-up were registered to those at post-implantation with the newly developed time-point registration method. The detailed explanation of the time-point registration is available in 3.3.8. Briefly, the vessel centerline at follow-up was first registered to the vessel centerline at post-implantation. Then, the stent centroid geometry at follow-up was registered to the stent centroid geometry at post-implantation. Finally, the reconstructed structures of the lumen and the stent at follow-up were translated accordingly to be registered to those at post-implantation.

4.3.4.2 Error Evaluation of Time-point Registration Method

The error of the time-point registration method was evaluated by measuring the stent-strut shift from post-implantation to follow-up. This result was compared to that in the preclinical setting (Table 3-9).

4.4 Results and Discussions

4.4.1 Vessel Centerline Reconstruction Method

The vessel centerline reconstruction method was validated in a clinical setting by (i) comparing the lengths of the vessel centerlines between two side branches (one was reconstructed with the newly developed method and the other was reconstructed from computed tomography angiography images) (4.4.1.1), and (ii) evaluating the reproducibility between different cardiac cycles and comparing it to that in the preclinical setting (4.4.1.2).

4.4.1.1 Comparison of Lengths of Vessel Centerlines between Two Side Branches

Computed tomography angiography is a clinically-used imaging modality to reconstruct the structure of the lumen. Although its sensitivity for detecting coronary arteries is not as high as that of coronary angiography, the 3D structures of the coronary arteries can be reconstructed with sufficient accuracy to evaluate its dimension.

The newly developed vessel centerline reconstruction method yielded the quite similar vessel centerlines to those from the computed tomography angiography images for all five vessels (Figure 4-1). From the vessel centerlines reconstructed with both methods, the lengths of the vessel centerlines between two side branches were measured. As shown in Table 4-1, the difference between two methods was 4.4% ± 3.2%, which is smaller than the static error of length.

(a) Computed tomography angiography-based reconstruction

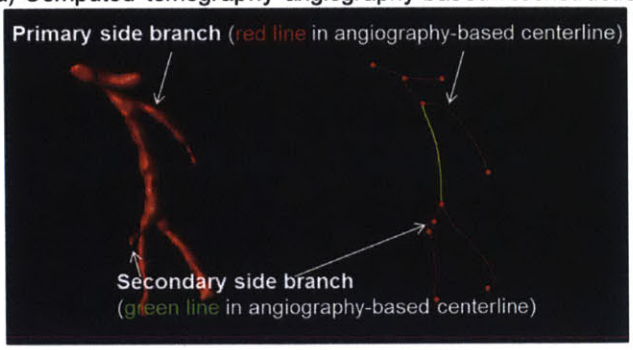

(b) Coronary angiography-based reconstruction

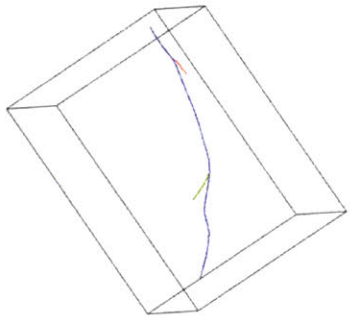

Figure 4-1 Reconstructed vessel centerlines with the clinically available computed tomography angiography method (a) and with the newly developed coronary angiography method

The reconstructed vessel centerlines with two different methods had quite similar shapes for all five vessels.

Table 4-1 Difference between the reconstructed vessel centerline length between the newly developed coronary angiography method and the clinically available computed tomography angiography method

All the values were represented as mean ± standard deviation.

	Error [mm]	Error [pixel]	Error [%]
Clinical data	1.4±1.1	5.4±4.1	4.4±3.2
Non-stented phantom	1.9±1.4	4.9±3.6	6.0±4.7

4.4.1.2 Reproducibility between Different Cardiac Cycles

The reproducibility between different cardiac cycles is another important metric to validate the newly developed vessel centerline reconstruction method. As discussed in 3.4.1.5, the paired angiographic images are acquired at the different timings and the OCT images are acquired before or after the angiographic images are acquired. Therefore, the reproducibility of the vessel centerline from different cardiac cycles needs to be evaluated to understand the potential error in structural reconstruction by angiography-OCT fusion.

The reconstructed vessel centerlines from two different cardiac cycles had quite similar

shapes (Figure 4-2). As summarized in Table 4-2, the reproducibility results with the clinical data were quite similar to that with the preclinical data.

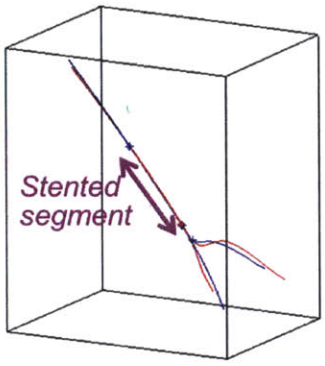

Figure 4-2 Reconstructed vessel centerlines from two different cardiac cycles (one patient result)
The vessel centerlines that were reconstructed from two different cardiac cycles had quite similar shapes, especially in the stented segment. Blue and red lines represent the vessel centerlines from two different cardiac cycles.

Table 4-2 Reproducibility of the vessel centerline between different cardiac cycles (N=5)
All the values were represented as mean ± standard deviation.

	Difference in length between two side branches	Distance between Landmarks 1	Distance between Landmarks 2	Angle between Landmarks 2
Clinical data	(2.9±1.4) mm (8.4±4.0) pixel	(0.12±0.05) mm (0.36±0.16) pixel	(0.25±0.07) mm (0.73±0.20) pixel	$7.0^0 \pm 2.2^0$
Preclinical data	(3.0±1.6) mm (8.8±4.7) pixel	(0.30±0.13) mm (0.89±0.38) pixel	(0.23±0.15) mm (0.69±0.44) pixel	$3.6^0 \pm 2.8^0$

4.4.2 Structural Reconstruction Method

The newly developed structural reconstruction method was validated by (i) evaluating the deformation of the vessel centerline over a cardiac cycle, (ii) comparing the reconstructed stent length to its actual length, and (iii) comparing the reconstructed stent length between post-implantation and follow-up.

4.4.2.1 Deformation of Vessel Centerline over a Cardiac Cycle

Since the OCT images of the stented segment are acquired over approximately a single cardiac cycle due to the fast pullback speed of OCT [1, 2], the deformation of the vessel centerline needs to be evaluated to understand the potential error in angiography-OCT fusion

when the vessel centerline is used as a fusion path. The vessel centerlines were reconstructed from four different cardiac phases, i.e., end-diastolic, mid-systolic, end-systolic, and mid-diastolic phases, and registered to the centerline from the end-diastolic phase.

The vessel centerlines from four different cardiac phases showed quite similar shapes, especially in the stented segment, for all three patients (Figure 4-3). As summarized in Table 4-3, all four parameters that were used for the evaluation of the deformation were similar between the cases where the clinical datasets were used and those where the preclinical datasets were used. In addition, the deformation results with the clinical datasets were similar to the reproducibility results (Table 4-2).

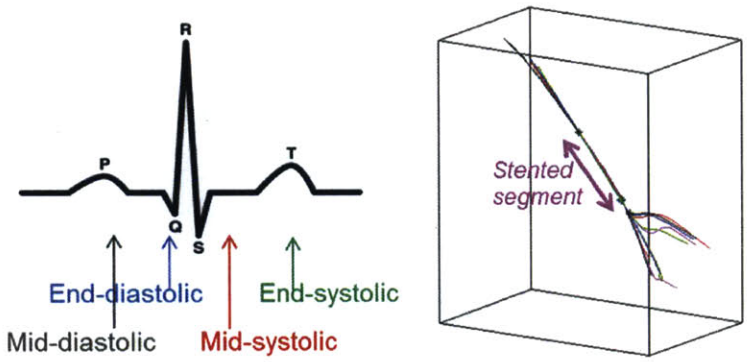

Figure 4-3 Deformation of the vessel centerline over a cardiac cycle (one patient result)
The vessel centerline did not deform significantly within the stented segment because the stent can serve as an anchor for the cardiac motion over a cardiac cycle. Blue, red, green, and black lines represent the vessel centerlines at end-diastolic, mid-systolic, end-systolic, and mid-diastolic phases, respectively, as shown in the ECG pattern.

Table 4-3 Deformation of the vessel centerline over a cardiac cycle (N=3)

All the values were represented as mean ± standard deviation.

	Difference in length between two side branches	Distance between Landmarks 1	Distance between Landmarks 2	Angle between Landmarks 2
Clinical data	(3.2±2.1) mm (9.3±6.1) pixel	(0.64±1.38) mm (1.87±3.75) pixel	(0.38±0.34) mm (1.10±1.00) pixel	$10.5^0 \pm 9.9^0$
Preclinical data	(4.3±1.7) mm (12.7±4.9) pixel	(0.33±0.21) mm (0.97±0.61) pixel	(0.38±0.29) mm (1.11±0.87) pixel	$7.1^0 \pm 6.0^0$

4.4.2.2 Comparison of Reconstructed Stent Length to Its Actual Length

To evaluate the error in the structural reconstruction method, the reconstructed stent lengths were compared to the actual stent length for all three patients. The absolute difference between these two values was 0.33 mm ± 0.21 mm (N=10; 5 patients, 2 time-points/patient), which is 1.6% ± 1.0% of the actual stent length. Although the sample size was quite small, these errors were smaller than those of the preclinical datasets (0.41 mm ± 0.34 mm, 2.4% ± 2.0%; N=36).

4.4.2.3 Comparison of Reconstructed Stent Lengths between Different Time-points

In addition to the comparison of the reconstructed stent length to the actual stent length, the reconstructed stent lengths were compared between two time-points, i.e., the post-implantation and the follow-up. The difference between two time-points was 0.35 mm ± 0.34 mm (N=5), which corresponds to 1.7% ± 1.8% when compared to the actual stent length. These values are within the range of those evaluated with the preclinical dataset (0.56 mm ± 0.41 mm, 3.3% ± 2.3%; N=24).

4.4.3 Time-point Registration Method

4.4.3.1 Registration Results and Registration Error

Figure 4-4 shows the registration results for all five patients. The error in the time-point registration was evaluated in terms of the stent-strut shift from post-implantation and follow-up. The absolute stent-strut shift was 1.3 mm ± 0.6 mm or 6.1% ± 2.2% relative to the actual stent length (N=5). These results were smaller than the error in the preclinical setting (1.6 mm ± 0.5 mm, 9.2% ± 3.0%; N=24).

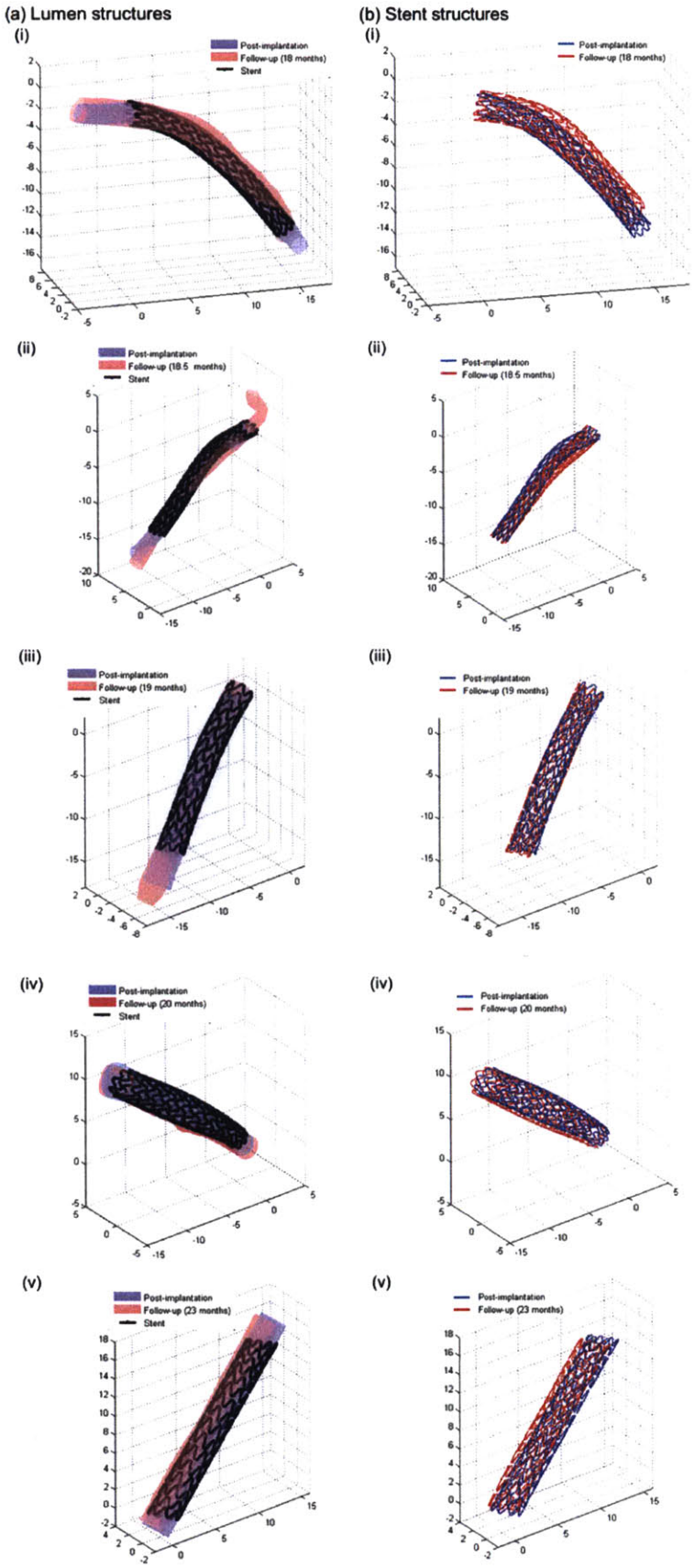

Figure 4-4

Time-point registration results for all five patients: (a) Lumen structure and (b) stent structure

For all five patients, the registered lumen structures in the proximal and/or distal region of the stented segment (a) and the registered stent structures (b) were aligned well, although the residual stent-strut shift existed in all cases. (i) to (v) in both (a) and (b) correspond to the reconstruction for the each patient.

4.4.3.2 Vessel Centerline Shift and Stent Deformation

Although both the vessel centerline and the stent centroid geometry are used as registration paths, a residual error in time-point registration was found in all patient cases. In 3.4.3.2, the potential cause for this error was correlated with the stent deformation; and thus, the vessel centerline shift and the stent deformation were evaluated with these five patients' data. The vessel centerline shift was measured with its direction (toward the myocardium or the fat tissue) that was determined by the angiographic images. Its positive value represents the shift toward the myocardium and its negative value represents the shift toward the fat tissue. The stent deformation was evaluated in terms of the eccentricity of the stent area.

As shown in Figure 4-5, a linear relationship was observed between the vessel centerline shift and the eccentricity change although the sample size was small. The slope of this relationship was less steep than that with the preclinical datasets ($y = 0.0681x+0.0181$ for 5-day follow-up, $y = 0.0659x+0.0117$ for 28-day follow-up). Some possible reasons for this include: (i) the difference in life expectancy between human and swine, (ii) the difference in the stent type, and (iii) the differences in the underlying condition of the coronary artery. First, the world-wide life expectancy at birth for a human is 70 years [3] or 71 years [4], while Yorkshire swine's life span is 6-10 years [5]. Therefore, 5-day or 28-day follow-up in the preclinical setting can be projected as approximately 50-day (1.5-month) or 280-day (9.5-month) follow-up in the clinical setting. On the other hand, the follow-up timings in the clinical datasets are 18-26 months (18 months, 18.5 months, two 19 months, and 23 months for the selected five patients). If the change of the slope is consistent, the slope is expected to be 0.0630 at 20-month follow-up; however, the difference between this expected slope value and the measured value still remains. Secondly, the implanted stent type is different between the preclinical and clinical datasets: the bare metal stent was used in the preclinical experiments, while the sirolimus-eluting stent was used in the clinical datasets. As sirolimus prevents the neointima formation by inhibiting the excessive proliferation of the smooth muscle cells in the arterial wall, the pressure on the stent from the

neointima may be lower than the cases where the bare metal stent was used. However, the higher stent fracture rate was reported when a drug-eluting stent, especially the sirolimus-eluting stent, was used [6, 7], which means that the sirolimus-eluting stent may have a stiffer structure compared to the bare metal stent. Therefore, the stent deforms less from a circle to an oval, which leads to the more negative value in the eccentricity change or the more gentle slope in the relationship between the vessel centerline shift and the eccentricity change. Thirdly, the pre-interventional arterial condition was quite different: the healthy coronary artery in the preclinical setting and the lipid-rich atherosclerotic coronary artery in the clinical setting. As discussed in 3.4.3.2, the eccentricity change is mainly induced by the pressure from the orientation of the myocardium and the fat tissue in the healthy animal model. On the other hand, in the clinical setting, the myocardium may be infarcted because the occlusion of the artery due to the atherosclerosis prevents the oxygen delivery to the myocardium. Therefore, although the plaque is soft enough for a stent to be fully apposed, the influence from the orientation of the myocardium and the fat tissue may diminish, which results in less eccentricity change.

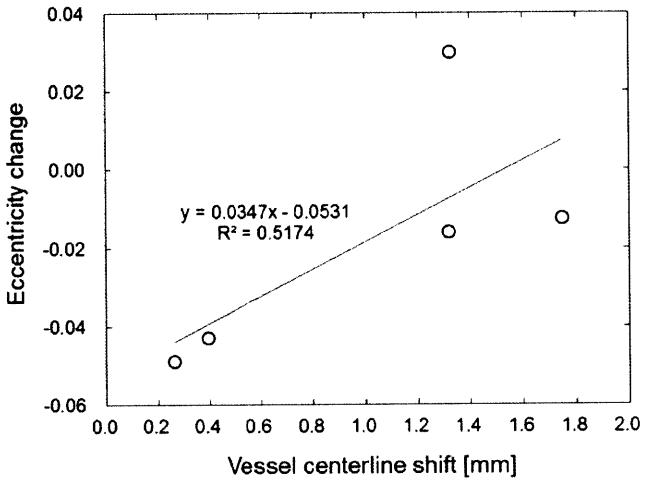

Figure 4-5 Relationship between the vessel centerline shift and the eccentricity change from post-implantation to follow-up

Although the sample size is small, the linear relationship between the vessel centerline shift and the eccentricity change was observed, the same as in the preclinical setting.

4.4.4 Clinical Applicability of Newly Developed Methods

4.4.4.1 Vessel Centerline Reconstruction Method

In the actual clinical setting, the angiographic images are acquired from non-isocentric and/or non-orthogonal viewpoints. The state-of-the-art methods, including those available in commercial software, have not been validated for the usage of both non-isocentric and non-orthogonal paired angiographic images. On the other hand, this newly developed method can handle both non-isocentric and non-orthogonal paired angiographic images. In addition, this new method demonstrated high reproducibility across various imaging angle differences (20^{o}-130^{o}) and between different cardiac cycles, specifically in the stented segment (3.4.1.4, 3.4.1.5, 4.4.1.2). This new method also can estimate accurately the total isocenter movement in each image (3.4.1.1). Moreover, this new method can yield the quite similar vessel centerlines compared to the vessel centerline that was reconstructed from the computed tomography angiography images, which is a clinically available method. Importantly, the error in vessel centerline reconstruction with this method in the clinical setting was similar to that in the preclinical setting, which suggests that this method is sufficiently robust even when the imaging environment cannot be recorded precisely and when the underlying disease may affect the image acquisition. In summary, these validation results indicate that this newly developed vessel centerline reconstruction method is clinically applicable.

4.4.4.2 Structural Reconstruction Method

Although many structural reconstruction methods by angiography-OCT fusion have been proposed and some of them have been used for the analysis of the data from the clinical trials [1, 8-12], the effect of cardiac motion on these methods has not been evaluated. In Chapter 3, the newly developed structural reconstruction method demonstrated its robustness to cardiac motion because: (i) no significant deformation of the vessel centerline was observed over a single cardiac cycle, (ii) the usage of the estimated OCT inter-frame distance based on the heart rate

information enabled the equal distribution of the stent-cells in the longitudinal direction, and (iii) the interpolation of the stent structures with the non-rigid point matching algorithm allowed the anatomically and physiologically correct reconstruction. As discussed in 4.4.2, this method was validated with the clinical datasets, demonstrating that: (i) the vessel centerline was not significantly deformed especially in the stented segment, (ii) the difference between the reconstructed stent length and the actual stent length was small and was similar to that in the preclinical setting, and (iii) the reconstructed stent length did not change significantly between the different time-points, the same as in the preclinical setting. Therefore, these results suggest that this method is clinically applicable and is robust in the presence of cardiac motion and coronary artery disease, i.e., atherosclerosis, where the stent is implanted.

4.4.4.3 Time-point Registration Method

The underlying mechanism of the vascular responses to stent implantation cannot be fully understood unless the vascular responses are tracked in 3D on the stent-strut level. The state-of-the-art methods can compare the different time-point data in 2D space by using the side branch as a landmark [13] or in 3D space on the 3-mm segment level [14]. The newly developed method enables the comparison of the different time-point data in 3D space on a smaller level (1-2 mm) by registering the accurately reconstructed structures from different time-points via a vessel centerline and a stent centroid geometry. The error of this method with the clinical datasets was similar to that with the preclinical datasets. The vessel centerline shift was correlated with the eccentricity change in the clinical setting, the same as in the preclinical setting. Both results suggest that this newly developed time-point registration method is clinically applicable, although the analysis on the stent-strut level (approximately 100 μm) has not been achieved yet.

4.4.4.4 Limitations

First and most importantly, the validations of all three methods in the clinical setting were

performed using data with a small sample size. Therefore, further analysis with data with a large sample size is required to confirm their clinical applicability (5.2.3).

Secondly, especially for the structural reconstruction method, the underlying disease condition, i.e., the plaque characteristics, was carefully selected in this validation. Thus, the clinical applicability of this method and the time-point registration method has not been evaluated in other disease conditions, such as calcified plaques. To make them applicable to any kinds of coronary artery diseases, further evaluation is necessary (5.2.1, 5.2.3).

References

1. Athanasiou, L.S., et al. *3D Reconstruction of Coronary Arteries using Frequency Domain Optical Coherence Tomography Images and Biplane Angiography.* in *34th Annual International Conference of the IEEE Engineering-in-Medicine-and-Biology-Society (EMBS).* 2012. San Diego, CA.
2. Jang, I.-K., *Optical Coherence Tomography or Intravascular Ultrasound?* JACC: Cardiovascular Interventions, 2011. **4**(5): p. 492-494.
3. United Nations, Department of Economics and Social Affairs, Population Division (2015), *World Population Prospects: The 2015 Revision.* 2015. Volume I: Comprehensive Tables (ST/ESA/SER.A/379).
4. World Health Organization, *Life expectancy.* Global Health Observatory data [cited April 17, 2016].
5. *The Life Span of a Yorkshire Pig.* [cited April 17, 2016]; Available from: http://animals.mom.me/life-span-yorkshire-pig-6185.html.
6. Nair, R.N., *Coronary Stent Fracture: A Review of the Literature.* Cardiac Cath Lab Director, 2011. **1**(1): p. 32-38.
7. Park, K.W., et al., *Clinical characteristics of coronary drug-eluting stent fracture: insights from a two-center des registry.* J Korean Med Sci, 2011. **26**(1): p. 53-8.
8. Hebsgaard, L., et al., *Co-registration of optical coherence tomography and X-ray angiography in percutaneous coronary intervention. The Does Optical Coherence Tomography Optimize Revascularization (DOCTOR) fusion study.* Int J Cardiol, 2015. **182**(0): p. 272-278.
9. Tu, S., et al., *In Vivo Flow Simulation at Coronary Bifurcation Reconstructed by Fusion of 3-Dimensional X-ray Angiography and Optical Coherence Tomography.* Circulation: Cardiovascular Interventions, 2013. **6**(2): p. e15-e17.
10. Tu, S.X., et al., *In vivo comparison of arterial lumen dimensions assessed by co-registered three-dimensional (3D) quantitative coronary angiography, intravascular ultrasound and optical coherence tomography.* International Journal of Cardiovascular Imaging, 2012. **28**(6): p. 1315-1327.
11. Tu, S., et al., *Fusion of 3D QCA and IVUS/OCT.* Int J Cardiovasc Imaging, 2011. **27**(2): p. 197-207.
12. Papafaklis, M.I., et al., *Anatomically correct three-dimensional coronary artery reconstruction using frequency domain optical coherence tomographic and angiographic data: head-to-head comparison with intravascular ultrasound for endothelial shear stress assessment in humans.* . EuroIntervention, 2014(1969-6213 (Electronic)).

13. Gutierrez-Chico, J.L., et al., *Vascular Tissue Reaction to Acute Malapposition in Human Coronary Arteries Sequential Assessment With Optical Coherence Tomography.* Circulation-Cardiovascular Interventions, 2012. **5**(1): p. 20-U81.
14. Stone, P.H., et al., *Prediction of progression of coronary artery disease and clinical outcomes using vascular profiling of endothelial shear stress and arterial plaque characteristics: the PREDICTION Study.* Circulation, 2012. **126**(2): p. 172-81.

CHAPTER 5: CONCLUSIONS

5.1 Summary of Thesis

5.1.1 Hypothesis and Research Goal

Coronary artery disease is a major cause of death worldwide, and its prevalence is expected to increase [1-4]. Innovative imaging technologies have dramatically improved the ability to diagnose coronary artery disease [5-8] and the procedural success of stent implantation, which is a widely-used treatment for atherosclerotic coronary artery disease [5, 9-12]. However, stent implantation may fail due to adverse outcomes, such as stent thrombosis or in-stent restenosis. Managing the adverse outcomes, i.e., the prediction, the prevention, and the treatment of the adverse outcomes, is still challenging due to the lack of methods (i) to reconstruct precise 3D structures of the lumen and the stent and (ii) to track the vascular responses over time by registering different time-point data. A lumen structure cannot be reconstructed in 3D from the 2D intravascular images that are acquired perpendicularly to the imaging catheter because the location of the catheter in 3D space is unknown [5]. Neither can the vascular morphological changes be tracked over time in 3D space since the imaging catheter cannot be placed at the exact same position at follow-ups. To compare the images taken at different time-points in 2D, landmarks that are visible at all time-points are used [13], but this comparison is limited by the number of available landmarks and prevents the analysis of the entire imaging dataset.

The hypothesis that governs this thesis is that new methods to reconstruct the 3D structures of lumens and stents accurately and to register the 3D structures of the same vessel across different time-points can be developed by melding different imaging modalities, i.e., coronary angiography and intravascular imaging modality. 3D reconstruction will advance the understanding of the interaction between plaque components in the lesion and the influence of

hemodynamics on the vascular wall in 3D. Time-point registration will provide the novel knowledge about the time course of vascular responses in 3D. Specifically, this thesis focuses on the vessel centerline technique – extracting the vessel centerline from two planar coronary angiographic images and transforming the 2D centerline information of each image into one 3D space. The 3D vessel centerline can provide both the 3D location of the imaging catheter for 3D reconstruction and 3D landmarks for comparison of images taken at different time-points. Although this technique has been used previously [14, 15], the state-of-the-art methods have been validated for images acquired under conditions that are difficult for physicians to satisfy in real-world clinical scenarios. Therefore, the main goal of this thesis is to improve the vessel centerline technique and make it clinically applicable, and to develop a method by fusing angiography and optical coherence tomography (OCT) that enables reconstructing the accurate 3D structures of lumens and stents and registering them across time.

5.1.2 Achievements

5.1.2.1 Vessel Centerline Reconstruction Method

Reconstruction of the vessel centerline from the paired angiographic images is important because the 3D vessel centerline can serve as a path of angiography-OCT fusion for the structural reconstruction and as a registration path. Although many methods have been proposed [14-26], the state-of-the-art methods have two limitations: (i) they are validated for the isocentric (no machine-origin isocenter offset or no movements of object) and orthogonal pair of angiographic images, and (ii) the effect of the cardiac motion has not been considered. Although some of the state-of-the-art methods have already been used in the clinical protocols, images are often non-isocentric and non-orthogonal in clinical situations because of two reasons. First, the C-arm fluoroscopic angiography system itself has an isocenter offset. Second, physicians may take images from various positions and may move the table during the procedure to obtain

better views and/or the patients themselves may move during the procedure. In addition to these problems, the influence of the cardiac motion needs to be overcome to enable the accurate reconstruction of the vessel centerline. Cardiac motion itself induces a morphological change in the coronary arteries, which may influence the reconstruction of the vessel centerline. This effect can be avoided if angiographic images are ECG-gated. However, although the coronary angiography system does have such a function, it is frequently not practical to acquire ECG-gated angiographic images in the clinical setting. Therefore, a new vessel centerline reconstruction method that can overcome these limitations is required.

The vessel centerline reconstruction method was first developed using the static phantom models. The newly developed method uses the stereoscopic theory [27], which relates the 3D geometry to its projected 2D geometry via a projection matrix. The usage of the projection matrix enables handling the non-orthogonal paired angiographic images. Then, a new algorithm that can estimate the total isocenter movement and can calibrate it in each angiographic image was implemented to enable handling the non-isocentric paired images. This algorithm showed the high accuracy for the estimation of the total isocenter movement and the high effectiveness for the vessel centerline reconstruction from the non-isocentric paired images. The static errors of the length and the angle were evaluated: 1.7 mm ± 1.4 mm or 4.4 pixel ± 3.5 pixel (5.0% ± 4.2%) and $2.6^0 \pm 2.0^0$ (4.2% ± 3.2%) for the non-stented phantom model, 1.8 mm ± 1.6 mm or 4.4 pixel ± 4.3 pixel (4.4% ± 4.0%) and $0.9^0 \pm 0.9^0$ (1.8% ± 1.7%) for the stented phantom model (Table 2-3). A strong linear relationship between the actual length and the reconstructed length was observed in the non-stented phantom model (Figure 2-8). The high reproducibility of the vessel centerline across the various imaging angle differences (20^0-130^0) was also achieved with this method (Table 2-3). This method was then validated under the condition where cardiac motion is to be considered and where the underlying disease, i.e., atherosclerosis, exists. The high reproducibility of the vessel centerline across the various imaging angle differences (20^0-130^0) was retained in the preclinical setting (Table 3-4). These imaging angle differences were superior

to those of the currently available methods, which can utilize the paired images with at least 25^0 of the imaging angle difference [18]. In addition, this method demonstrated the high reproducibility between different cardiac cycles (Table 3-5, Table 4-2), which has not been evaluated with any state-of-the-art methods. This method is further significant because the total isocenter movement can be accurately estimated; thus, when the machine-origin isocenter offset is negligibly small, the information of the movement of the table and/or the patient during the procedure can be collected retrospectively whenever needed.

5.1.2.2 Structural Reconstruction Method

This thesis focuses on the fusion of coronary angiography with optical coherence tomography (OCT) as a means of the structural reconstruction. Cardiac motion potentially affects the accuracy of the structural reconstruction when angiography-OCT fusion is used for two reasons. First, cardiac motion may change the morphology of the coronary artery, which may lead to the morphological change of the vessel centerline. Because the OCT images of the stented segment are acquired over approximately a single cardiac cycle due to the fast pullback speed of OCT [28], the change in the vessel centerline morphology may result in the error in the structural reconstruction when the vessel centerline is used as a fusion path. Secondly, the OCT imaging catheter can move laterally and longitudinally during the pullback due to cardiac motion [29]. Previous study with four patients' data demonstrated that the usage of the vessel centerline as a fusion path could directly overcome the lateral movement problem and that it induced a small error in angiography-OCT fusion due to the longitudinal movement of the imaging catheter [29]. However, the structural reconstruction has yet to be optimized in relation to the cardiac motion since the accuracy of the structural reconstruction by angiography-OCT fusion has not been fully evaluated.

First, the deformation of the vessel centerline was assessed in both preclinical and clinical settings (*in vivo* swine and *in vivo* human datasets). The vessel centerlines that were

reconstructed from four different cardiac phases, i.e., end-diastolic, mid-systolic, end-systolic, and mid-diastolic phases, showed no significant differences (Table 3-6, Table 4-3). Therefore, the end-diastolic vessel centerline was selected as a fusion path based on physiological and experimental rationales (3.4.2.1). The potential error in structural reconstruction due to the error in the vessel centerline reconstruction including the deformation of the vessel centerline over a cardiac cycle and the reproducibility errors across the imaging angle differences and between different cardiac cycles was estimated to be approximately 3%.

Secondly, to overcome the longitudinal movement problem of the OCT imaging catheter, the method to correct the OCT inter-frame distance was established and implemented. From the original OCT images, the stent-cell height in the longitudinal direction was measured and was interpolated as a sinusoidal wave using *a priori* knowledge of the stent design and the recorded heart rate. Since the preset, constant OCT inter-frame distance may also be affected by the cardiac motion, the interpolated OCT inter-frame distance was adjusted based on the actual stent length. This method enabled the evaluation of the OCT inter-frame distance in a physiologically realistic and meaningful way. By interpolating the OCT inter-frame distance as a sinusoidal wave, the correction of the OCT inter-frame distance can be applied through extrapolation to the region where the stent is not available, e.g. the region between the stent edge and the nearest side branch. By using the corrected OCT inter-frame distance, the error of the reconstructed stent length relative to its actual stent length was improved approximately 2.3-fold and that between different time-points was improved by approximately 2.1-fold (Table 3-7, Table 3-8). Similar results were achieved with five patients' data in the clinical setting (4.4.2.2, 4.4.2.3).

Thirdly, to create the physiologically realistic and accurate structures of the lumen and the stent, the method for interpolating and smoothing 2D-to-3D transformed points was established. For the lumen structures, the transformed points were smoothened along the longitudinal direction in 3D. For the stent structures, the transformed points were fit to their actual known

design using a non-rigid point matching algorithm.

These results suggest that this newly developed method can reconstruct the 3D structures of the lumen and the stent in a physiologically realistic and precise way by using (i) the end-diastolic vessel centerline, (ii) the estimated OCT inter-frame distance, and (iii) the prior knowledge of the stent design. The total error in the structural reconstruction method can be predicted to be approximately 3% based on both preclinical and clinical results.

5.1.2.3 Time-point Registration Method

To optimize the procedure of stent implantation and to predict chronic outcomes before the procedure, the underlying mechanism of the vascular responses needs to be understood in 3D on the stent-strut level (approximately 100 μm). Time-point registration is important because the full understanding of the vascular responses and their mechanisms can be achieved only when the 3D structures of the same vessel at different time-points are registered precisely in 3D. Since the imaging catheter cannot be located at the exact same location over time, the imaging catheter cannot be a path for registering the structures of the same vessel across time. The state-of-the-art methods can compare 2D images using the side branches as landmarks [30] or 3D structures on the 3-mm segment level [31], both of which prevent a full understanding of the vascular responses due to the limited number of available side branches or the limited resolution. On the other hand, the vessel centerline can be an ideal path to register the different time-point 3D structures because as many landmarks can be created as needed and because the higher resolution may be achieved by registering the structures precisely in 3D space. However, the morphology of the vessel centerline itself may change over time by the vascular responses to stent implantation; therefore, to develop a new time-point registration method, the influence of the vascular responses on the vessel centerline needs to be first evaluated, and then the points on the centerline that are insensitive to the morphological change need to be found to use as landmarks.

Two landmarks were first set on the reconstructed vessel centerline: Landmark 1 is located on the stented segment at 21 mm downstream from the intersection of the stented segment and the nearest side branch, and Landmark 2 is located on the side branch at 2 mm downstream from the intersection. Since the stent length is shorter than 21 mm, these landmarks were set aiming to avoid the vascular responses to stent implantation. However, due to the twisting and the growth of the side branch, the stent-strut shift from post-implantation to follow-up remained large when only the vessel centerline was used (2.6 mm ± 1.4 mm, relative to the stent length: 15.0% ± 8.0%; Table 3-9). Therefore, another landmark or registration path that is more robust to the time-dependent morphological change of the vessels was required; and thus, the stent centroid geometry was selected as a secondary registration path. By using both the vessel centerline and the stent centroid geometry, the stent-strut shift has improved by approximately 1.6-fold (1.6 mm ± 0.5 mm, relative to the stent length: 9.2% ± 3.0%; Table 3-9). This newly developed time-point registration method demonstrated a similar or slightly smaller error in the clinical setting (1.3 mm ± 0.6 mm, relative to the stent length: 6.1% ± 2.2%; five patients' data). Although the stent-strut level analysis has not been achieved yet with this method, this newly developed method enables the 3D analysis with higher resolution than 3 mm. In addition, this method can increase the number of OCT frames that can be compared between different time-points by measuring the distance of the centerline from the side branches and/or the stent edges at each time-point.

5.1.3 Physiological and/or Pathological Findings

5.1.3.1 Stent Deformation and Tissue Orientation around Coronary Artery

The stent itself may deform across time because the pressure may distribute unequally in the angular direction due to the difference in the types of the tissues that surround coronary arteries and the differences in the vascular responses to stent implantation. The stent

deformation and these potential biomechanical influences were evaluated in the preclinical setting.

The stent area and the eccentricity were first evaluated to understand how the stent deforms over time. The stent area decreased slightly at 28-day follow-up, while the eccentricity tended to increase over time (Figure 3-24, Figure 3-25). Although no statistically significant differences were observed between any time-points for both the stent area and the eccentricity, this result suggests that the stent deforms from a circular shape to an oval shape without shrinking or expanding. As the eccentricity increased, both lengths of the semi-major axis and the semi-minor axis decreased; a higher decrease rate was observed in the semi-minor axis length than the semi-major axis length, which suggests that some force gradient that changed the semi-minor axis governed the increase in the eccentricity over time.

To understand the cause of this eccentricity change, the orientation of the myocardium and the fat tissue was first correlated with the major axis of the eccentricity. At all three time-points, strong 1:1 relationships were observed between the boundary axis angle of the myocardium and the fat tissue and the major axis angle of the eccentricity (Figure 3-27). Since this strong linear relationship was observed at 28-day follow-up, at which the significant amount of the neointima was formed in all stented vessels, the tissue orientation of the myocardium and the fat tissue is considered as the primary factor to induce the stent deformation over time. This was supported by the fact that the difference in the slope of the relationship between this eccentricity change and the vessel centerline shift toward the myocardium was minimal between 5-day follow-up and 28-day follow-up (Figure 3-29).

5.1.3.2 Existence of Stent Underexpansion and Vascular Responses

In the preclinical swine model, the underexpansion of the stent was created with the specially-modified balloon catheter. This attempted to mimic the malapposition of the stent, which was reported to occur in 62% of lesions when DES was used [32]. When the stent

underexpansion was created in the healthy swine coronary artery, it was resolved within 5 days due to the vascular recoil by the smooth muscle cells in the arterial wall (Figure 3-31). However, the thicker neointima was formed in the underexpanded cases compared to the fully-apposed cases (Figure 3-32), which is consistent with the well-known mechanism of the neointima response to stent implantation: the blood flow disruption due to stent implantation induces the variation of the wall shear stress distribution in the stented segment, resulting in the neointima formation, and this disruption is exacerbated by the underexpansion of the stent [31, 33-36].

In the underexpanded cases, the neointima thickness was linearly correlated with the eccentricity change from post-implantation to 5-day follow-up and the steeper slope was observed in the area where the underexpansion was originally created and the areas distal to the underexpanded area (Figure 3-33). This result suggests that the eccentricity change may be another factor to determine the degree of the neointima response in the malapposition cases.

5.2 Future Directions

In this thesis, the vessel centerline reconstruction method, the structural reconstruction method, and the time-point registration method were developed using the static phantom models and *in vivo* swine models. These methods were preliminarily validated using a small sample of the clinical datasets. To improve these newly developed methods and to make them clinically applicable, further research is required.

5.2.1 Improvement of Structural Reconstruction Method

The structural reconstruction method was developed and validated using the data that the stents were implanted to the healthy artery (*in vivo* swine model) or the artery with soft plaque (*in vivo* human model) to make sure the stent was fully apposed to the arterial wall. Therefore, the applicability of this newly developed method is unknown when the stents are implanted to the other types of atherosclerotic plaques, e.g., calcified plaques. When the stents are implanted to the hard lesions, the stent may not be able to fully expand, which may affect the measurement of the stent-cell height, leading to the error in the OCT inter-frame distance correction. Further study is necessary to understand the effect of the lesion type on structural reconstruction and to improve this new method to be applicable to variable lesion characteristics.

In addition, this new method requires *a priori* knowledge of the stent design to correct the OCT inter-frame distance and to interpolate the stent structure. Thus, an investigation of the clinically available stent types is important to create a data bank of the stent design and to make this method available for all the stent types.

5.2.2 Improvement of Time-point Registration Method

Although the usage of the stent centroid geometry as a secondary registration path has improved the time-point registration compared to using only the vessel centerline as a registration path, the stent-strut shift still remains 1.6 mm on average, which prevents the

long-term analysis of the vascular responses on the stent-strut level. As discussed in 3.4.3.2, the stent itself deforms due to the unequal pressure distribution in the angular direction. This deformation was the likely cause of the vessel centerline shift, which induced the error in time-point registration. Therefore, to improve time-point registration, the vessel centerline shift needs to be corrected by evaluating the stent deformation and/or the landmarks that are more robust to cardiac motion and to the pressure distribution need to be sought.

Alternatively, the stent structure itself can be used as the landmark although it deforms over time. Once the same points on the stent are found based on the edges of the stent and/or the stent-cells and the prior knowledge of the stent design, they will enable registering the reconstructed 3D structures non-rigidly with the non-rigid point matching algorithm [37] that was used in the last step of the structural reconstruction. However, the downside of this method is that the features of the structural reconstruction method, i.e., the reconstruction of the physiologically realistic and accurate structures, will be no longer available after the registration. This will affect the appreciation of the vascular responses, especially when the hemodynamic aspect is added, since the precise evaluation of the hemodynamic influence, i.e., the blood flow simulation, can be achieved only when the physiologically correct geometry is used.

5.2.3 Further Assessment of Clinical Applicability

Since all three methods were validated with clinical data with a small sample size, further validation using data with a large sample size is necessary to understand the accuracy and the robustness of these methods in the clinical setting.

5.2.4 Further Understanding of Relationship between Eccentricity Change and Vascular Responses

In 3.4.4, the linear relationship between the eccentricity change from post-implantation to 5-day follow-up and the neointima thickness was observed in the underexpanded cases. This result suggests the possibility that the eccentricity change on the acute phase may determine the vascular responses on the chronic phase, especially in the underexpanded cases. Since the underexpansion of the stent was observed in 62% of the DES implantation [32], the further understanding of the relationship between the eccentricity change and the vascular responses may help the management of the stent implantation.

As discussed in 3.4.3.2, in the healthy animal model, the stent deforms mainly due to the continuous pressure from the myocardium according to the rhythm of the heartbeat. In addition, no difference in the stent deformation was observed between the fully-apposed cases and the underexpanded cases in this animal model probably because all the underexpansion was resolved within 5 days due to the vascular recoil and because the continuous pressure can be applied to the stent although the underexpansion was created at post-implantation. On the other hand, when the range of the eccentricity change was compared between the preclinical setting and the clinical setting, the range in the clinical setting was 10 times smaller than that in the preclinical setting. These results lead to the hypothesis that the stent deforms only when the vessel can recoil, i.e., the vessel has an ability to resolve the malapposition, and when the myocardium is intact and can move according to the heartbeat. Therefore, to fully understand the influence of the stent deformation on the vascular responses, the relationship between the eccentricity change and the vascular responses needs to be appreciated in the four conditions described in Table 5-1.

In 3.4.4, the relationship between the eccentricity change on the acute phase (from post-implantation to 5-day follow-up) and the neointima thickness at 28-day follow-up was revealed: more neointima was observed at 28-day follow-up especially in the area where the

underexpansion was created and the areas distal to the originally underexpanded area. Although it is well-known that the blood flow disruption due to stent implantation and/or stent malapposition induces the higher neointima response on the chronic phase [31, 33-36], the factors that determine the degree of the neointima response have not been revealed yet. Since all the underexpansion was resolved on the acute phase, the pattern of the blood flow disruption changed at least twice in the underexpanded cases (when the stent was implanted and when the underexpansion was resolved). This result may suggest a hypothesis that the neointima response may be proportional to (i) the degree of the flow disruption, (ii) the number of times that the flow disruption patterns have changed on the acute phase, and (iii) the pre-interventional arterial wall condition, i.e., the degree of the arterial narrowing and the type of atherosclerotic plaques. This hypothesis also needs to be tested in the four conditions in Table 5-1.

Table 5-1 Four conditions in which further analysis is required to understand the underlying mechanism of the vascular responses to stent implantation

		Vessel wall condition	
		Healthy (Can recoil)	Abnormal (Cannot recoil)
Myocardium condition	Intact (Can move with the heartbeat)	Healthy animal model [Chapter 3]	Modified animal model Make the arterial wall stiffer by placing a stent in the arterial wall prior to the actual stent implantation
	Infarcted (Cannot move with the heartbeat)	Patient data	Patient data

5.2.5 Appreciation of Insight into Vascular Responses

Development of the structural reconstruction method and the time-point registration method enables more sophisticated modeling that can include information about the plaque components and the hemodynamics, to evaluate the morphological change of the coronary artery due to the vascular responses. These newly added dimensions will help in gaining more insight into the vascular responses. Therefore, following the improvement of both the structural reconstruction method and the time-point registration method and the further evaluation of their clinical applicability, the underlying mechanism of the vascular responses can be studied in detail and hopefully be fully appreciated on the stent-strut level.

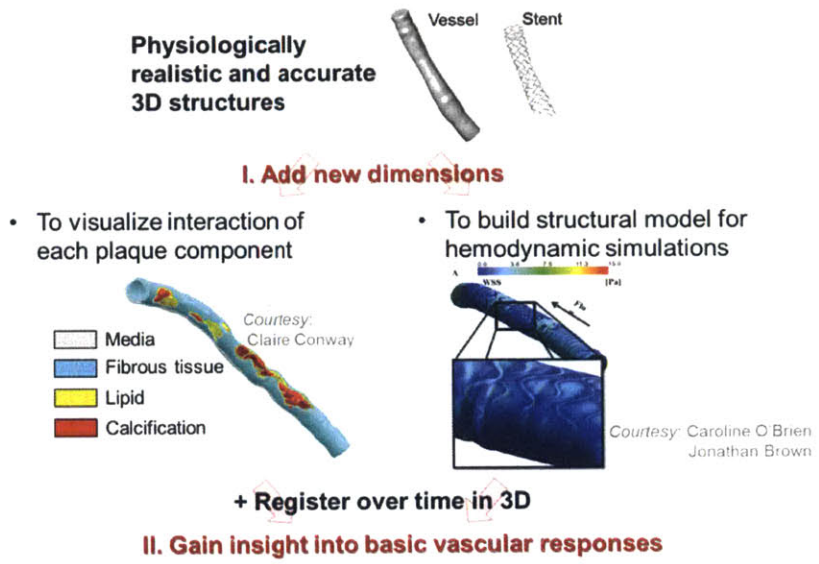

Figure 5-1 Workflow to understand the underlying mechanism of the vascular responses to stent implantation

5.3 Clinical Application

This thesis is a multi-scale and multi-dimensional project that combines the meticulousness of the precise imaging, the power of both bench-top and animal studies with controllable parameters, and the clinical patient data with uncontrollable parameters. All three methods that have been developed through this thesis make use of all the available imaging data including unbiased and clinically diverse patient data. The accumulated data can serve as a data bank, which will help physicians assess the risk of stent failure, optimize the procedure and prescribe patient-specific medication. Moreover, 3D reconstructions with this method will enable physicians to make more accurate diagnoses of the lesions and will give better guidance during the procedure. Therefore, the achievements of this thesis and the further understanding of the underlying mechanisms of the vascular responses with future improvement in the time-point registration will enable the advancement of catheter-based coronary intervention, especially stent implantation.

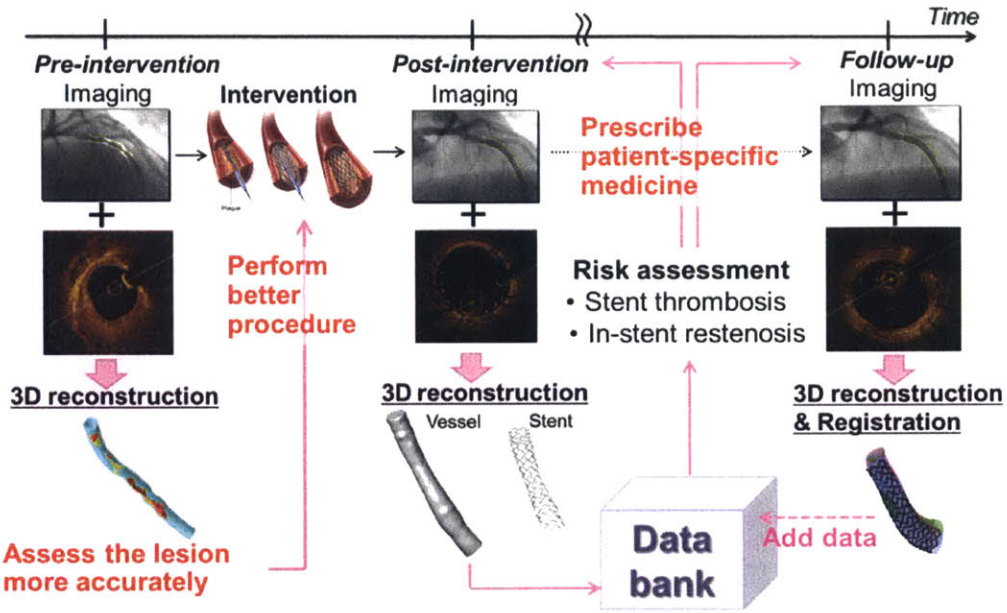

Figure 5-2 Potential clinical usage of the structural reconstruction method and the time-point registration method

References

1. Roger, V.L., et al., *Heart disease and stroke statistics--2012 update: a report from the American Heart Association.* Circulation, 2012. **125**(1524-4539 (Electronic)): p. e2-e220.
2. World Health Organization Global Health Observatory, *Noncommunicable Diseases (NCD) Mortality and Morbidity.* [cited 2014 April 20]; Available from: http://www.who.int/gho/ncd/mortality_morbidity/en/.
3. World Health Organization, *Cardiovascular Diseases (CVDs) Fact sheet N°317.* 2013 March 2013; Available from: http://www.who.int/mediacentre/factsheets/fs317/en/index.html.
4. World Health Origanization, *Burden: mortality, morbidity and risk factors.* Global Status Report on Noncommunicable Diseases 2010. 2011.
5. Dowe, D.A., M. Fioranelli, and P. Pavone, *Imaging Crororary Arteries.* 2nd ed. 2013: Springer.
6. Dvir, D., et al., *Three-dimensional coronary reconstruction from routine single-plane coronary angiograms: in vivo quantitative validation.* Int J Cardiovasc Intervent, 2005. **7**(1462-8848 (Print)): p. 141-145.
7. Saito, T., et al., *Three-dimensional quantitative coronary angiography.* Biomedical Engineering, IEEE Transactions on, 1990. **37**(8): p. 768-777.
8. Brown, B.G., et al., *Quantitative coronary arteriography: estimation of dimensions, hemodynamic resistance, and atheroma mass of coronary artery lesions using the arteriogram and digital computation.* Circulation, 1977. **55**(2): p. 329-37.
9. Shah, V.M., et al., *Background incidence of late malapposition after bare-metal stent implantation.* Circulation, 2002. **106**(14): p. 1753-5.
10. Yock, P.G., et al., *Intravascular ultrasound guidance for catheter-based coronary interventions.* Journal of the American College of Cardiology, 1991. **17**(6s2): p. 39-45.
11. Kubo, T., et al., *Application of Optical Coherence Tomography in Percutaneous Coronary Intervention.* Circulation Journal, 2012. **76**(9): p. 2076-2083.
12. Adriaenssens, T., et al., *Optical coherence tomography (OCT) in PCI for in-stent restenosis (ISR): rationale and design of the SEDUCE (Safety and Efficacy of a Drug elUting balloon in Coronary artery rEstenosis) study.* Eurointervention, 2011. **7**: p. K100-K105.
13. Gutierrez-Chico, J.L., et al., *Vascular tissue reaction to acute malapposition in human coronary arteries: sequential assessment with optical coherence tomography.* Circ Cardiovasc Interv, 2012. **5**(1): p. 20-9, S1-8.
14. Bourantas, C.V., et al., *A new methodology for accurate 3-dimensional coronary artery reconstruction using routine intravascular ultrasound and angiographic data: implications for widespread assessment of endothelial shear stress in humans.* EuroIntervention, 2013. **9**(5):

p. 582-593.

15. Yang, J., et al., *Novel approach for 3-d reconstruction of coronary arteries from two uncalibrated angiographic images.* IEEE Trans Image Process, 2009. **18**(7): p. 1563-72.
16. Tu, S.X., et al., *In vivo comparison of arterial lumen dimensions assessed by co-registered three-dimensional (3D) quantitative coronary angiography, intravascular ultrasound and optical coherence tomography.* International Journal of Cardiovascular Imaging, 2012. **28**(6): p. 1315-1327.
17. Athanasiou, L.S., et al. *3D Reconstruction of Coronary Arteries using Frequency Domain Optical Coherence Tomography Images and Biplane Angiography.* in *34th Annual International Conference of the IEEE Engineering-in-Medicine-and-Biology-Society (EMBS).* 2012. San Diego, CA.
18. Tu, S., et al., *Fusion of 3D QCA and IVUS/OCT.* Int J Cardiovasc Imaging, 2011. **27**(2): p. 197-207.
19. van der Giessen, A.G., et al., *3D fusion of intravascular ultrasound and coronary computed tomography for in-vivo wall shear stress analysis: a feasibility study.* International Journal of Cardiovascular Imaging, 2010. **26**(7): p. 781-796.
20. Slager, C.J., et al., *True 3-Dimensional Reconstruction of Coronary Arteries in Patients by Fusion of Angiography and IVUS (ANGUS) and Its Quantitative Validation.* Circulation, 2000. **102**(5): p. 511-516.
21. Bourantas, C.V., et al., *ANGIOCARE: An automated system for fast three-dimensional coronary reconstruction by integrating angiographic and intracoronary ultrasound data.* Catheterization and Cardiovascular Interventions, 2008. **72**(2): p. 166-175.
22. Bourantas, C.V., et al., *A method for 3D reconstruction of coronary arteries using biplane angiography and intravascular ultrasound images.* Computerized Medical Imaging and Graphics, 2005. **29**(8): p. 597-606.
23. Wahle, A., et al., *Fusion of angiography and intravascular ultrasound in vivo: establishing the absolute 3-D frame orientation.* Biomedical Engineering, IEEE Transactions on, 1999. **46**(10): p. 1176-1180.
24. Wahle, A., et al., *Geometrically correct 3-D reconstruction of intravascular ultrasound images by fusion with biplane angiography-methods and validation.* IEEE Transactions on Medical Imaging, 1999. **18**(8): p. 686-699.
25. Shekhar, R., et al. *Fusion of intravascular ultrasound and biplane angiography for three-dimensional reconstruction of coronary arteries.* in *Computers in Cardiology, 1996.* 1996.
26. Laban, M., et al. *ANGUS: a new approach to three-dimensional reconstruction of coronary vessels by combined use of angiography and intravascular ultrasound.* in *Computers in*

Cardiology 1995. 1995.

27. Faugeras, O., Q.-T. Luong, and T.o. Papadopoulo, *The geometry of multiple images : the laws that govern the formation of multiple images of a scene and some of their applications*. 2001, Cambridge, Mass.: MIT Press. xxiv, 644 p.
28. Jang, I.-K., *Optical Coherence Tomography or Intravascular Ultrasound?* JACC: Cardiovascular Interventions, 2011. **4**(5): p. 492-494.
29. Papafaklis, M.I., et al., *Anatomically correct three-dimensional coronary artery reconstruction using frequency domain optical coherence tomographic and angiographic data: head-to-head comparison with intravascular ultrasound for endothelial shear stress assessment in humans*. . EuroIntervention, 2014(1969-6213 (Electronic)).
30. Gutierrez-Chico, J.L., et al., *Vascular Tissue Reaction to Acute Malapposition in Human Coronary Arteries Sequential Assessment With Optical Coherence Tomography.* Circulation-Cardiovascular Interventions, 2012. **5**(1): p. 20-U81.
31. Stone, P.H., et al., *Prediction of progression of coronary artery disease and clinical outcomes using vascular profiling of endothelial shear stress and arterial plaque characteristics: the PREDICTION Study.* Circulation, 2012. **126**(2): p. 172-81.
32. Im, E., et al., *Incidences, predictors, and clinical outcomes of acute and late stent malapposition detected by optical coherence tomography after drug-eluting stent implantation.* Circulation. Cardiovascular interventions, 2014. **7**(1): p. 88-96.
33. Chen, H.Y., et al., *Impact of stent mis-sizing and mis-positioning on coronary fluid wall shear and intramural stress.* Journal of Applied Physiology, 2013. **115**(2): p. 285-292.
34. Stone, P.H., et al., *Effect of endothelial shear stress on the progression of coronary artery disease, vascular remodeling, and in-stent restenosis in humans: in vivo 6-month follow-up study.* Circulation, 2003. **108**(4): p. 438-44.
35. Rikhtegar, F., et al., *Compound Ex Vivo and In Silico Method for Hemodynamic Analysis of Stented Arteries.* Plos One, 2013. **8**(3).
36. Kolandaivelu, K., et al., *Stent thrombogenicity early in high-risk interventional settings is driven by stent design and deployment and protected by polymer-drug coatings.* Circulation, 2011. **123**(13): p. 1400-9.
37. Myronenko, A. and S. Xubo, *Point Set Registration: Coherent Point Drift.* Pattern Analysis and Machine Intelligence, IEEE Transactions on, 2010. **32**(12): p. 2262-2275.

APPENDIX: PRECLINICAL STENT-CELL LEVEL ANALYSIS

A.1 Purpose

To understand the effect of the underexpansion of the stent on the stent deformation and the chronic vascular responses, the analysis of the stent-cell level was performed.

A.2 Methods

The stent deformation and the chronic vascular responses were evaluated in terms of the eccentricity and the wall-to-stent distance, respectively, at all three time-points (post-implantation, 5-day follow-up, and 28-day follow-up). As discussed in Chapter 3, since the error in time-point registration was 1.6 mm ± 0.5 mm and since the stent-cell length was 1.7 mm, this analysis was performed by grouping every two stent-cells, which were numbered from 1 to 10 in the direction of proximal to distal (Figure A-1). This grouping was achieved by measuring the length of the vessel centerline from the edge of the stent. In each OCT frame, the eccentricity was evaluated by fitting the detected stent-struts in an oval. The wall-to-stent distance was evaluated by averaging the distances between the lumen surface and each detected stent-strut. This distance is positive if the stent-strut is located inside the lumen. Then, all the evaluated eccentricities and wall-to-stent distances from the OCT frames that were within every each two stent-cells were averaged.

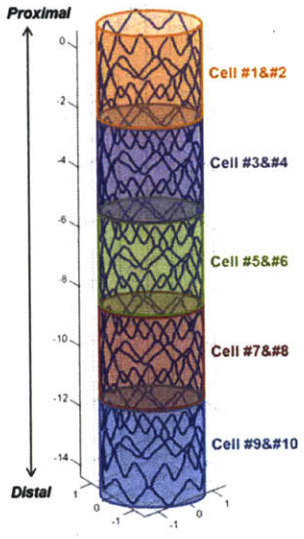

Figure A-1 Grouping of the stent-cells for the stent-cell level analysis

A.3 Results

All the results were summarized in Figure A-2 - A-6.

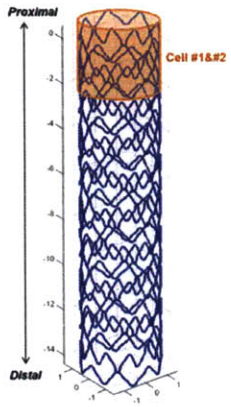

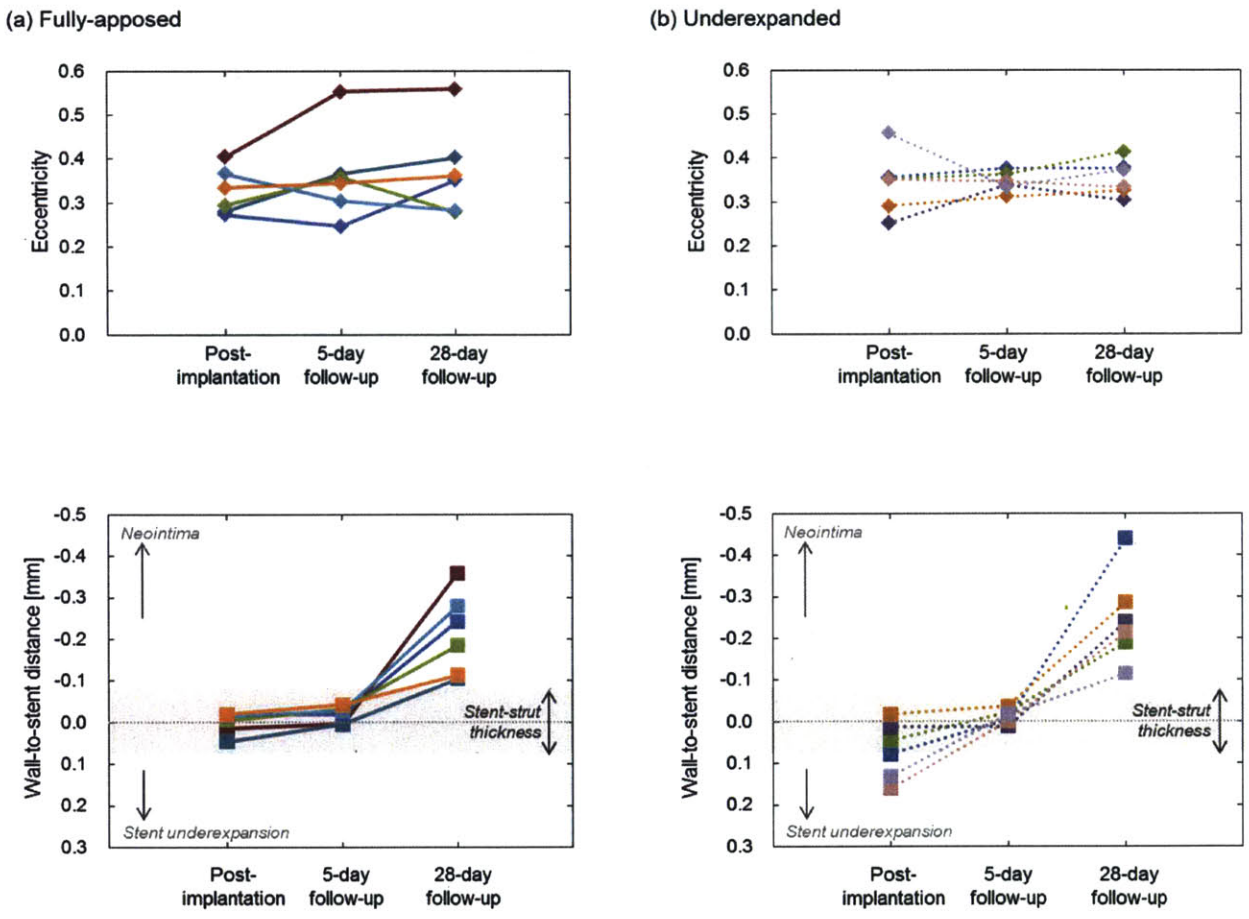

Figure A-2 Changes of eccentricity and wall-to-stent distance in stent-cell #1&#2

Each line represents each stented vessel.

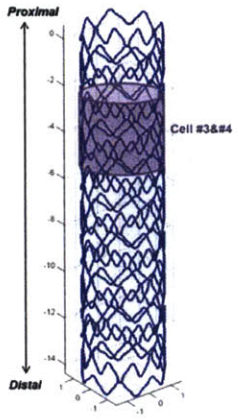

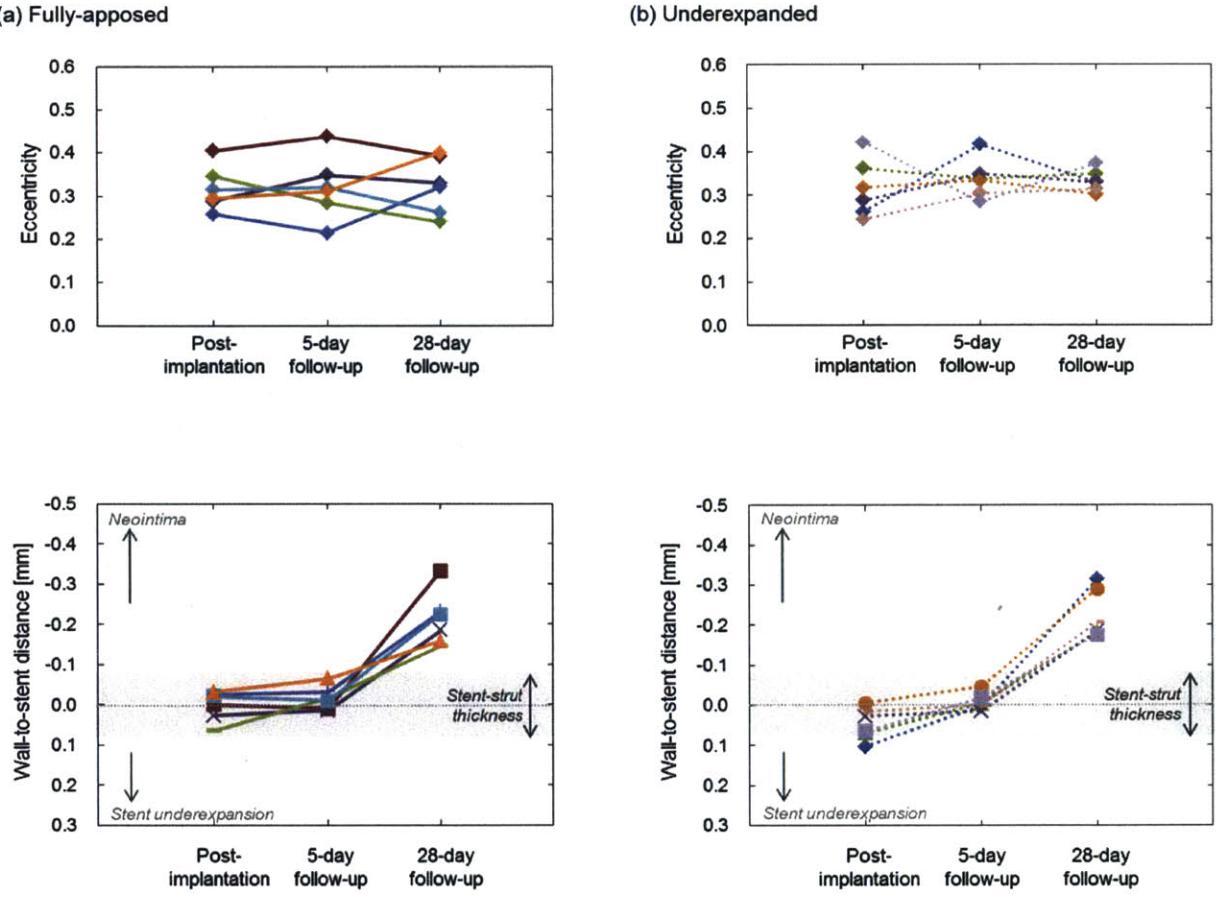

Figure A-3 Changes of eccentricity and wall-to-stent distance in stent-cell #3&#4

Each line represents each stented vessel.

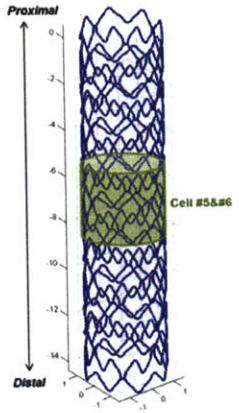

(a) Fully-apposed

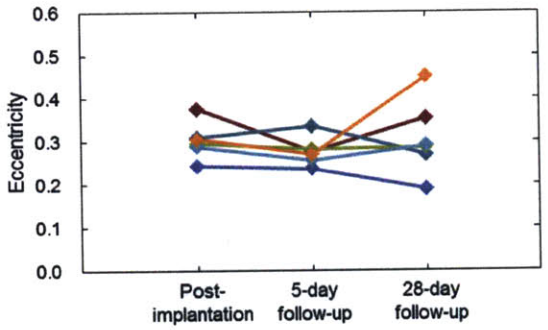

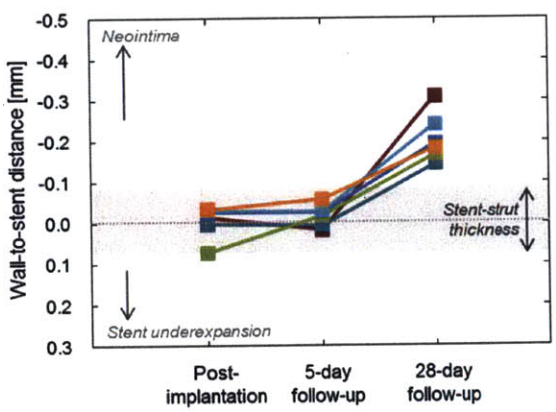

(b) Underexpanded

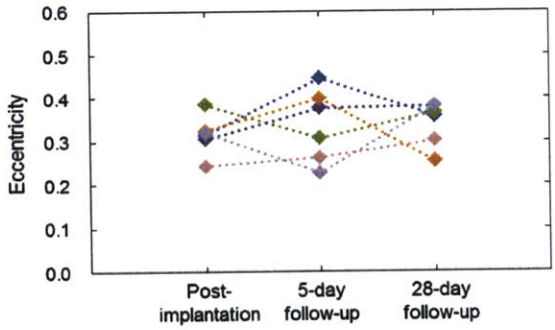

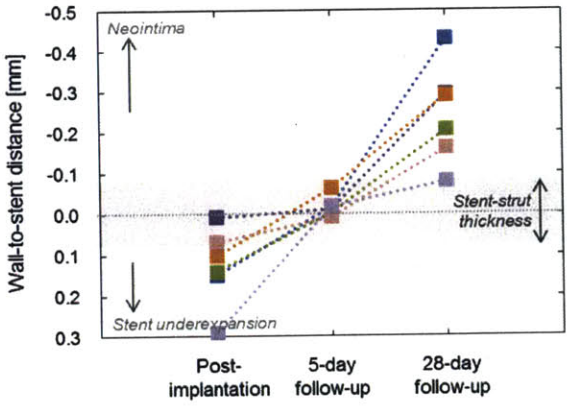

Figure A-4 Changes of eccentricity and wall-to-stent distance in stent-cell #5&#6

Each line represents each stented vessel.

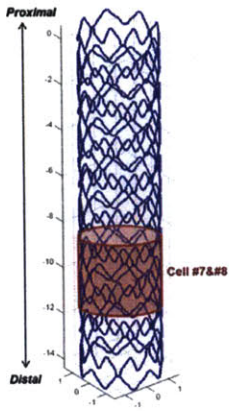

(a) Fully-apposed

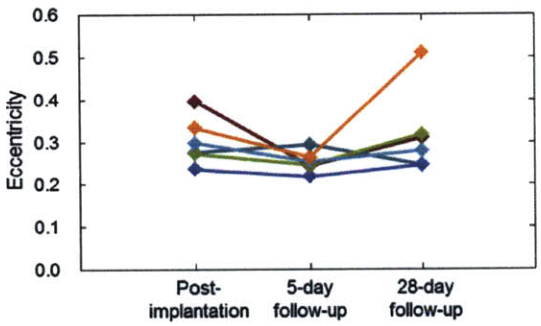

(b) Underexpanded

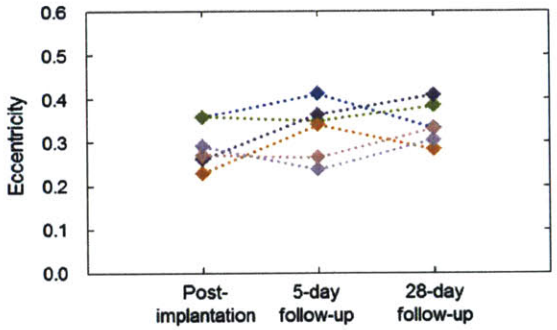

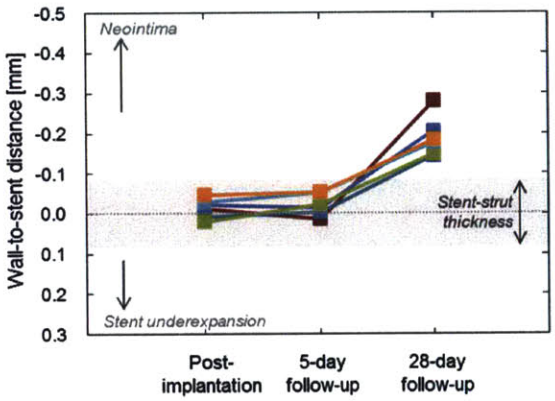

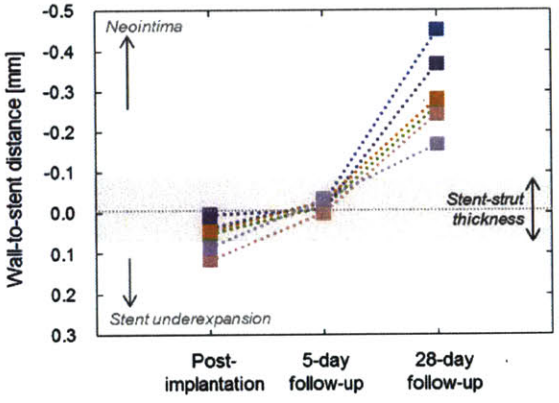

Figure A-5 Changes of eccentricity and wall-to-stent distance in stent-cell #7&#8

Each line represents each stented vessel.

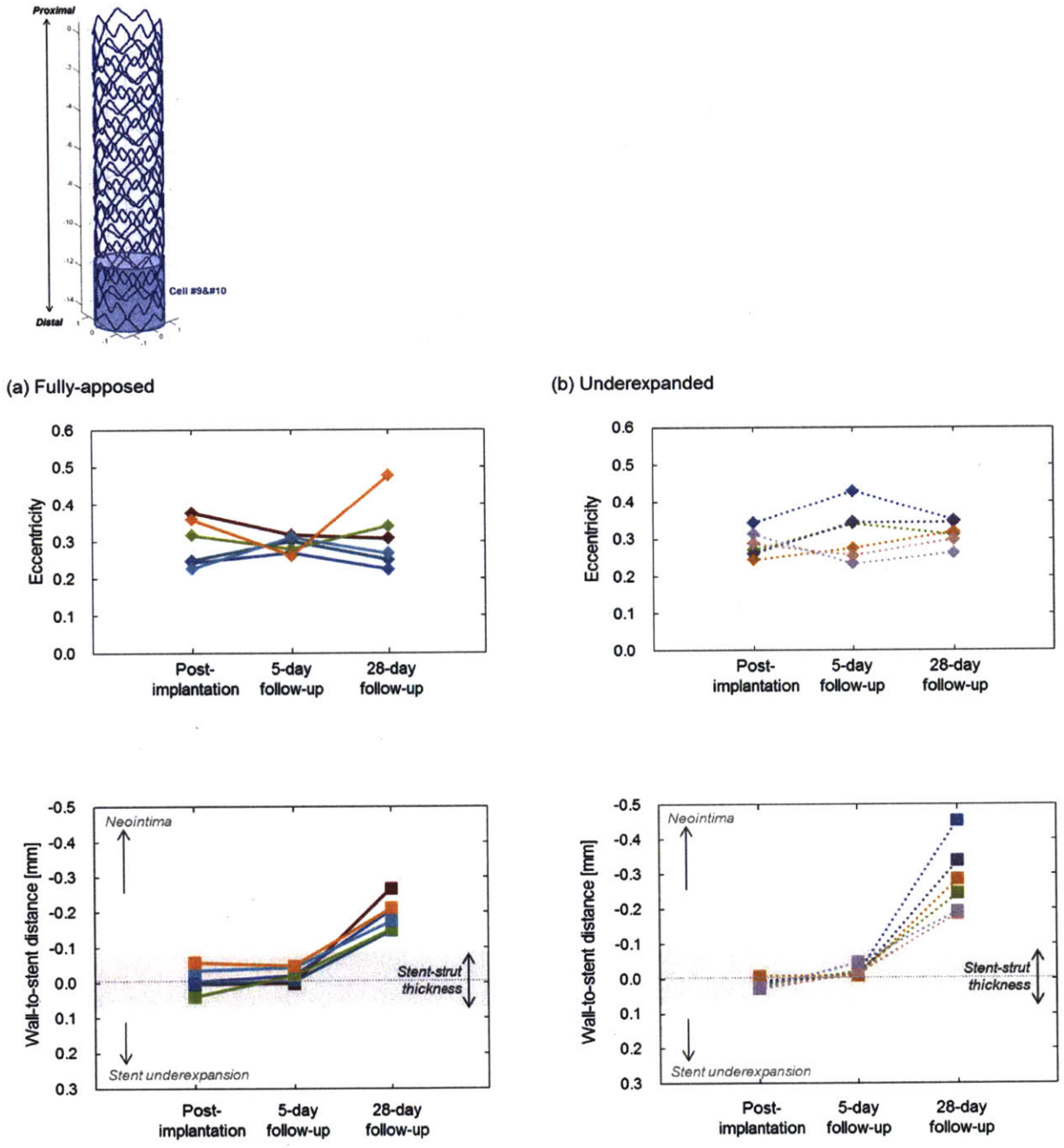

Figure A-6 Changes of eccentricity and wall-to-stent distance in stent-cell #9&#10

Each line represents each stented vessel.